



HAL
open science

Evaporation of moderately volatile elements from silicate melts: experiments and theory

Paolo Sossi, Stephan Klemme, Hugh St.C. O'Neill, Jasper Berndt, Frédéric Moynier

► **To cite this version:**

Paolo Sossi, Stephan Klemme, Hugh St.C. O'Neill, Jasper Berndt, Frédéric Moynier. Evaporation of moderately volatile elements from silicate melts: experiments and theory. *Geochimica et Cosmochimica Acta*, 2019, 260, pp.204-231. 10.1016/j.gca.2019.06.021 . insu-02916918

HAL Id: insu-02916918

<https://insu.hal.science/insu-02916918>

Submitted on 12 Aug 2021

HAL is a multi-disciplinary open access archive for the deposit and dissemination of scientific research documents, whether they are published or not. The documents may come from teaching and research institutions in France or abroad, or from public or private research centers.

L'archive ouverte pluridisciplinaire **HAL**, est destinée au dépôt et à la diffusion de documents scientifiques de niveau recherche, publiés ou non, émanant des établissements d'enseignement et de recherche français ou étrangers, des laboratoires publics ou privés.



Distributed under a Creative Commons Attribution 4.0 International License

Evaporation of moderately volatile elements from silicate melts: experiments and theory

Paolo A. Sossi^{1*}, Stephan Klemme², Hugh St.C. O'Neill³, Jasper Berndt², Frédéric Moynier^{1,4}

¹Institut de Physique du Globe de Paris, 1 rue Jussieu, F-75005, Paris, France

²Institut für Mineralogie, Westfälische Wilhelms-Universität Münster, Correnst. 24, D48149 Münster, Germany

³Research School of Earth Sciences, Australian National University, 2601 Canberra, Australia

⁴Institut Universitaire de France, 75005, Paris, France

* Corresponding author. Present address: Institute of Geochemistry and Petrology, ETH Zürich, Sonneggstrasse 5, CH-8092, Zürich, Switzerland. E-mail: paolo.sossi@erdw.ethz.ch

Abstract

Moderately volatile elements (MVEs) are sensitive tracers of vaporisation in geological and cosmochemical processes owing to their balanced partitioning between vapour and condensed phases. Differences in their volatilities allows the thermodynamic conditions, particularly temperature and oxygen fugacity (fO_2), at which vaporisation occurred to be quantified. However, this exercise is hindered by a lack of experimental data relevant to the evaporation of MVEs from silicate melts. We report a series of experiments in which silicate liquids are evaporated in one-atmosphere (1-atm) gas-mixing furnaces under controlled fO_2 s, from the Fe-“FeO” buffer (iron-wüstite, IW) to air ($10^{-0.68}$ bars), bracketing the range of most magmatic rocks. Time- (t) and temperature (T) series were conducted from 15 to 930 minutes and 1300-1550°C, at or above the liquidus for a synthetic ferrobalt, to which 20 elements, each at 1000 ppm, were added. Refractory elements (*e.g.*, Ca, Sc, V, Zr, REE) are quantitatively retained in the melt under all conditions. The MVEs show highly redox-dependent volatilities, where the extent of element loss as a function of fO_2 depends on the stoichiometry of the evaporation reaction(s), each of which has the general form $M^{x+n}O_{(x+n)/2} = M^xO_{x/2} + n/4O_2$. Where n is positive (as in most cases), the oxidation state of the element in the gas is more reduced than in the liquid, meaning lower oxygen fugacity promotes evaporation. We develop a general framework, by integrating element vaporisation stoichiometries with Hertz-Knudsen-Langmuir (HKL) theory, to quantify evaporative loss as a function of t , T and fO_2 . Element volatilities from silicate melts differ from those during solar nebular condensation, and can thus constrain the conditions of volatile loss in post-nebular processes. Evaporation in a single event strongly discriminates between MVEs, producing a step-like abundance pattern in the residuum, similar to that observed in the Moon or Vesta. Contrastingly, the gradual depletion of MVEs according to their volatility in the Earth is inconsistent with their loss in a single evaporation event, and instead likely reflects accretion from many smaller bodies that had each experienced different degrees of volatilisation.

Keywords: Moderately Volatile Element, Evaporation, Volatile Depletion, Experiment, Silicate Melts

1.0. Introduction

Phase transformation from condensed (liquid, l, or solid, s) to gaseous (g) form, termed evaporation, is a ubiquitous geological process occurring during outgassing of ascending magmas (Symonds and Reed, 1993; Mather et al., 2012), upon heating attending meteorite impacts in the crust (Humayun and Koeberl, 2004; Moynier et al., 2009) and, on a larger scale, in planetary accretion processes (O'Neill, 1991; Alexander, 2001; Visscher and Fegley, 2013). The *volatility* of an element refers to its tendency to partition into the gas phase relative to condensed phases, and at equilibrium, depends on the thermodynamic conditions, especially the temperature and fO_2 at which these processes occur.

Under solar nebula conditions, the volatility of an element is quantified by its '50% condensation temperature', T_c^{50} , the temperature at which half its mass is calculated to condense from a gas of solar composition at equilibrium (Larimer, 1967). As T_c^{50} of the elements vary among one another, their abundances in chondrites may be used to constrain temperatures at which they accreted (*e.g.*, Keays et al. 1971; Laul et al. 1973), a concept known as 'cosmothermometry' (Urey, 1954). Although elemental abundances in chondrites correlate positively with T_c^{50} , these temperatures refer to specific conditions; that of a rarified (tenuous) nebular gas, with assumed pressures, P_{total} of 10^{-3} - 10^{-5} bar (Larimer, 1967; Grossman, 1972; Grossman and Larimer, 1974; Lodders, 2003), in which H_2 is the most abundant species, such that $pH_2 \sim P_{total}$. The correspondingly low H_2O/H_2 (5×10^{-4} ; Rubin et al. 1988) of the solar nebula promotes very reducing conditions, ~ 7 log units below the iron-wüstite (IW) oxygen buffer at 1400 K. Low total pressures result in condensation temperatures that are below the silicate, metal and sulfide solidi, such that condensation occurs into solid phases (Ebel, 2004).

In the absence of any other scale, T_c^{50} has been widely used to quantify element volatility in various other contexts, such as degassing from planetary bodies. Although refractory elements and the main components (Fe, Mg, Si) in the Earth and other planetary bodies (the Moon, Mars, Vesta) have abundances similar to those in chondritic meteorites, the moderately volatile elements (MVEs), with $650 < T_c^{50}$ (K) < 1300 at 10^{-4} bar (Palme et al., 1988), are variably depleted (Urey, 1954; Ringwood, 1966; Wanke and Dreibus, 1988; O'Neill and Palme, 1998; Albarède et al., 2015). The sub-equal distribution of MVEs between the gas and condensed phases holds promise for quantifying the conditions of volatile loss processes, which neither refractory elements (hardly lost) nor highly volatile elements (almost entirely lost) address.

Chondrite-normalised abundances of lithophile MVEs in the mantles of differentiated rocky bodies plotted against T_c^{50} define 'volatility trends'. Depletions of siderophile MVEs relative to these trends point to their additional loss to planetary cores (*e.g.*, Wood et al. 2006; Siebert and Shahar 2015). However, the proportions of siderophile MVEs (*e.g.*, Ga, Pb, In) inferred to reside in Earth's core using this approach are irreconcilable with their experimentally-determined metal-silicate partition coefficients

36 (Wang et al. 2016; Blanchard et al. 2017; Ballhaus et al. 2017; Norris and Wood, 2017), suggesting T_c^{50}
37 may not be an apt descriptor of volatility at the conditions relevant to the formation of Earth.

38 The assumption implicit in the use of T_c^{50} states that volatile loss occurred under the same solar nebular
39 conditions experienced by chondritic meteorites, and therefore neglects variations in nebular chemistry
40 (*cf.* Ebel and Grossman 2000; Schaefer and Fegley 2010), in addition to the likelihood that planetary
41 bodies continued to accrete following dissipation of the nebular gas. Indeed, numerical simulations of
42 planetary formation highlight the potential for chemical fractionation to occur throughout their growth
43 (*e.g.*, Morbidelli et al. 2012; Carter et al. 2015). These *post-nebular* processes include collisional erosion
44 of differentiated material (O'Neill and Palme, 2008; Bonsor et al., 2015) and melting and evaporation of
45 planetesimals or planets *via* ^{26}Al and ^{60}Fe decay (Sahijpal et al., 2007) or impact heating (Pahlevan et al.,
46 2011). Models for the Moon-forming impact invoke temperatures ≥ 4000 K (*e.g.*, Melosh 1990;
47 Nakajima and Stevenson 2014) and pressures between 10^3 and 100 bar (Canup et al., 2015). The $f\text{O}_2$ of
48 the gas evolved by evaporation of silicates is close to the Fayalite-Magnetite-Quartz (FMQ) buffer
49 (De Maria et al., 1971; Visscher and Fegley, 2013; Costa et al., 2017), orders of magnitude higher
50 than in the solar nebula. Moreover, elemental depletions in planetary environments reflect not only
51 volatility, but also the ability for the gas species to be carried away from the locus of vaporisation,
52 which varies with physical factors such as planetary size, molar mass and atmospheric structure
53 (Chamberlain and Hunten, 1989). As such, equilibrium is not mandated during evaporation (Young et
54 al. 2019) and the physical mechanism cannot, *a priori*, be treated as the inverse of equilibrium
55 condensation. Indeed, MVE depletion patterns in many planetary bodies are quite unlike those in
56 chondritic meteorites (*e.g.*, O'Neill and Palme, 2008), attesting to their accretion under conditions and/or
57 *via* mechanisms distinct from those of the solar nebula. Volatility trends established under these post-
58 nebular conditions should thus diverge from expectations based on T_c^{50} . Together, these
59 considerations call for more quantitative descriptions of element volatility relevant to the evaporation
60 of silicate melts.

61 Existing experimental constraints (Chapman and Scheiber, 1969; Notsu et al., 1978; Bart et al., 1980;
62 Tsuchiyama et al., 1981; Kreuzberger et al., 1986; Shimaoka et al., 1994; Wulf et al., 1995; Norris and
63 Wood, 2017; Braukmüller et al., 2018) highlight a dependence of element volatility on $f\text{O}_2$; some
64 elements (*e.g.*, Zn, Cd, Na) become more volatile at low $f\text{O}_2$, whereas others (*e.g.*, Ir, Au, As) become
65 less so. Differences were found between volatilities inferred from evaporation of silicate melts and
66 those calculated for solar nebula condensation. While abundances of elements that are refractory in the
67 solar nebula (*e.g.*, Al, Ti, Sc, REEs) increased in evaporation residues (Chapman and Scheiber, 1969;
68 Notsu et al., 1978), K ($T_c^{50} = 1006$ K) was observed to vaporise more readily than Na ($T_c^{50} = 958$ K)
69 (Kreuzberger et al., 1986) while In ($T_c^{50} = 536$ K) was found to be less volatile than Zn ($T_c^{50} = 726$ K)
70 (Norris and Wood, 2017). Norris and Wood (2017) argued that, because this order of volatility better
71 matched the MVE depletions observed in Earth's mantle, they were lost *via* evaporation from silicate

72 melts rather than during nebular condensation. Nevertheless, a theoretical understanding of the process
73 studied in these experiments has hitherto not been addressed.

74 Here, we present experimental results of trace element loss during Langmuir (free) evaporation of a
75 ferrobaltic melt composition as a function of run time, temperature and fO_2 . We develop a theoretical
76 approach based on Hertz-Knudsen-Langmuir (HKL) theory (*e.g.* Knudsen 1909) that quantifies the
77 effect of t , T and fO_2 on element loss and determines stoichiometries of element vaporisation reactions.
78 This model enables extrapolation and prediction of evaporative element loss from silicate melts and is
79 used to better understand the conditions and mechanisms that lead to volatile depletion among rocky
80 planetary bodies.

81 2.0. Methods

82 2.1. Experimental Methods

83 Reagent-grade, major-element oxide powders (Fe_2O_3 - MgO - Al_2O_3 - SiO_2) were weighed out and ground
84 in an agate mortar. Calcium was added as carbonate ($CaCO_3$). The major element composition (Table
85 1) represents a compromise between achieving a low liquidus temperature whilst still resembling a
86 realistic planetary mantle composition. To this end, an Anorthite-Diopside eutectic composition was
87 used, to which roughly 15 wt. % each of forsterite and Fe_2O_3 were added. Trace elements were added
88 to a separate mixture; the alkalis (Li, Na, K, Rb) were added as carbonates. The remaining elements
89 were added as oxides, so as to mimic their speciation in silicate melts (addition of elements as
90 solutions, *e.g.*, nitrates was avoided as this may cause elements to behave abnormally during heating).
91 Oxides added were: Cu_2O , Ga_2O_3 , GeO_2 , PbO , MnO , MoO_2 , V_2O_5 , ZrO_2 , Sc_2O_3 , ZnO , TiO_2 , La_2O_3 ,
92 Gd_2O_3 , Yb_2O_3 , Ag_2O and CdO , totalling 20 elements, six of which (Zr, Sc, Ti, and the REEs) are
93 nominally refractory. All oxides were added in proportions equivalent to one-another, to give \approx
94 28,000 ppm of the element in the final trace element mix, of which 3.6 wt. % was added to the
95 FCMAS composition to give \approx 1000 ppm of each element in the final mixture (Table 1). The
96 ensemble was then decarbonated at 1000 °C for 24 h in air and re-ground. Experiments were also
97 performed with the FCMAS mix prior to the addition of the trace element mixture to assess the degree
98 of contamination during the experiments.

99 For each experiment, around 25 mg of powder was mixed into a viscous slurry with 100,000
100 molecular weight polyethylene oxide and loaded onto a metal wire loop. In order to minimise Fe, and
101 other metal loss to the loop, Re was used where possible at reducing conditions (below FMQ),
102 whereas Pt loops (and one Ir loop) were used above FMQ. Oxygen fugacity was externally buffered
103 by CO-CO₂ gas mixtures metered from Tylan mass flow controllers (range 0–200 and 0–20 standard
104 cubic centimetres per minute, sccm), whose performance was checked *in-situ* using a yttria-stabilised
105 zirconia SIRO₂ oxygen sensor at 1000 °C (see O'Neill and Eggins, 2002). The sensor was not used in

106 the actual experiments because of the high temperatures. Oxygen fugacities varied between 10^{-10} bar
107 ($\approx IW$) to $10^{-0.68}$ bar (air) at a given temperature, at an estimated accuracy of ± 0.05 log units. Excepting
108 experiments in air and at ANU, the total gas flow rate was kept constant at each oxygen fugacity, \approx
109 200 sccm. Gas flow rates are listed in Table 2, along with run duration and temperature. Experiments
110 performed at Westfälische Wilhelms-Universität, Münster, are denoted by the code ‘M’, those at the
111 Research School of Earth Sciences, ANU, by ‘C’ and at the Institut de Physique du Globe de Paris, by
112 ‘P’.

113 Samples were introduced into the 3-cm-long hotspot of a 42-mm internal-diameter, 70-cm-long
114 GERO vertical alumina tube furnace directly at the set-temperature, between $1300 < T$ ($^{\circ}\text{C}$) < 1550 ,
115 with run times between 15 min and 930 min. Gases were allowed to run and equilibrate in the sealed
116 furnace tube for ≈ 10 min prior to sample introduction. The gas continually flowed through the tube,
117 and was evacuated by a line at the top of the furnace. The volume of the furnace tube relative to that
118 of the sample is sufficiently large that vapour produced upon sample evaporation was efficiently
119 removed from the hotspot and condensed in the cold zones of the tube, thereby approximating an open
120 system. Temperature was controlled with a thermocouple external to the alumina muffle tube by a
121 Eurotherm® controller, limiting fluctuations to within ± 1 $^{\circ}\text{C}$. Temperatures were independently
122 measured, and adjusted as necessary, with a Type B thermocouple bead (Klemme and O’Neill, 2000)
123 located < 5 mm above the sample. Run duration is reported from the time of sample insertion and
124 therefore includes a thermal equilibration time. This time (defined as the time needed to reach 99% of
125 the set temperature) was determined to be between 4 – 7 minutes, conforming to the relationship dT/dt
126 $= k(T_{\text{final}} - T)$, where k is the response time constant. When integrated with respect to time and
127 temperature, this gives $t = (-\ln(T_{\text{final}} - T) + \ln(T_{\text{initial}} - T))/k$. The value of k was experimentally determined to
128 be 0.018 at 1350°C from the observed increase in temperature for a Type B thermocouple bead of 10^{-4}
129 m radius. The response time constant is related to specific heat capacity (C_p), mass (m) and area (A) of
130 the material by the expression $k = hA/mC_p$, where h is the external heat transfer coefficient and
131 depends on the properties of the gas phase. Since silicate melt spheres in our experiments have higher
132 heat capacities (≈ 1500 J/kgK) and surface areas ($\approx 2 \times 10^{-5}$ m²) than the thermocouple bead,
133 equilibration times are expected to be similar. Charges were quenched by dropping them into a
134 beaker of distilled water.

135 *2.2. Analytical Methods*

136 Trace element abundances in the quenched glasses were measured by Laser-Ablation Inductively-
137 Coupled Plasma Mass Spectrometry (LA-ICP-MS) at the Institut für Mineralogie, Westfälische
138 Wilhelms-Universität Münster. Glasses were mounted in epoxy and polished before being placed in a
139 dual-volume Helix cell filled with He gas (≈ 1 L/min; large cell and 0.33 L/min, small cell). Ablation
140 was performed by a Photon Machines Analyte G2 193 nm ArF excimer laser with a repetition rate of

141 10 Hz, a total fluence of 4 J/cm² and a spot size of 130 μm (25 μm for zoning profiles). The ablation
142 sequence consisted of 20 s background and 40 s of counting time, in which the ablated material was
143 carried to the *ThermoFisher* Element II running in low resolution mode. Each mass peak is measured
144 four times (100 samples per peak with a mass window of 4%) for a total of 0.02 s each. The isotopes
145 measured for this purpose were: ⁷Li, ²³Na, ²⁹Si, ³⁹K, ⁴³Ca, ⁴⁵Sc, ⁴⁷Ti, ⁴⁹Ti, ⁵¹V, ⁵³Cr, ⁵⁵Mn, ⁶⁰Ni, ⁶³Cu,
146 ⁶⁶Zn, ⁶⁹Ga, ⁷²Ge, ⁷³Ge, ⁸⁵Rb, ⁹⁰Zr, ⁹³Nb, ⁹⁵Mo, ¹⁰⁷Ag, ¹¹¹Cd, ¹¹⁵In, ¹³³Cs, ¹³⁹La, ¹⁵⁷Gd, ¹⁷²Yb, ¹⁸²W,
147 ¹⁸⁵Re, ¹⁹³Ir, ¹⁹⁵Pt, ²⁰⁸Pb, totalling an analytical pass time of roughly 0.6 s. Oxide production rates, as
148 monitored by the ²³²Th¹⁶O/²³²Th ratio, were < 0.1 %.

149 Samples were ablated between 6 – 12 times, with care taken to analyse both the core and rim of the
150 glass bead, permitting detection of any zoning. Standards bracketed sample ablation every 12 – 24
151 points (*i.e.*, every two samples), and consisted of a set of three NIST-612 and two basaltic standards
152 (either BCR-2G, GSD-1G, GSE-1G or BIR-1G, depending on the session). Standardisation was
153 performed in two stages. Firstly, the NIST-612 standard glass, in which trace elements are present at ≈
154 40 ppm levels, was used to produce calibration curves relating counts per second to concentration for
155 a given isotope. Following this initial normalisation, ²⁹Si was used as an internal standard (41 wt. %
156 SiO₂ in samples) to correct for matrix effects between the samples and NIST-612 by comparison with
157 BCR-2G, GSD-1G, GSE-1G or BIR-1G, whose matrix is a good analogue for the experimental
158 glasses.

159 Relative standard deviation (RSD) across all elements in a given sample was 5.1±0.4% (SD),
160 excluding cases where the element concentration was near the detection limit (frequently Cd and Ag,
161 but also in some experiments where elements have been quantitatively lost). In these instances, the
162 RSD increases to 15 – 20%, while Li also has a high RSD (≈10%), presumably owing to the analyses
163 of Li tetra- and metaborate-fluxed fused discs on the LA-ICP-MS system. For major elements and
164 those with interference-free masses (*e.g.*, Na, Sc, V, Cr, Mn, Rb and the REE), RSD is typically 2-3
165 %. Analytical accuracy was assessed by analyses of basaltic reference materials; concentrations of all
166 elements were found to be within 10% (and often 5%) of the most recent published analyses using
167 femtosecond LA-ICP-MS (Jochum et al. 2014; Li et al. 2015; Electronic Annex A). The sole
168 exception is Ge; its measured abundance is systematically higher in BCR-2G (⁷²Ge, 2.16±0.10 and
169 ⁷³Ge, 2.23±0.16 ppm) and BIR-1G (⁷²Ge, 4.25±0.60 and ⁷³Ge, 2.18±0.44 ppm) compared to published
170 values (1.51±0.10 and 1.2±0.1 ppm, respectively). This discrepancy disappears for synthetic basaltic
171 glasses with higher Ge contents; GSD-1G (39.07±0.99 vs. 40±1 ppm) and GSE-1G (391.6±13.6 vs.
172 402±16 ppm), pointing to the production of ⁵⁶Fe¹⁶O⁺ and lesser amounts of ⁵⁷Fe¹⁶O⁺ and ⁵⁶Fe¹⁶O¹H⁺
173 on ⁷²Ge and ⁷³Ge, respectively. While these interferences degrade the accuracy of Ge measurements at
174 low abundances (≈ 1 ppm), they are negligible at the concentrations relevant to the experiments (10 –
175 1000 ppm).

176 3.0. Theoretical Framework

177 The kinetic theory of gases states that particles in an isothermal ideal gas have a Maxwell-Boltzmann
 178 distribution of kinetic energies (Maxwell, 1860; Boltzmann, 1872). Such molecular chaos
 179 (*stosszahlansatz*) occurs when the mean free path, the average distance travelled by a gaseous
 180 molecule prior to collision, is greater than the diameter of the particles. At 1673 K and 1 bar, the mean
 181 free path is $\approx 5 \times 10^{-6}$ metres, 10^4 times larger than typical molecular diameters (Chapman and Cowling,
 182 1970). In this framework, the number of particles striking a surface over a given time interval is given
 183 by the Hertz-Knudsen-Langmuir (HKL) equation (Hertz, 1882; Knudsen, 1909; Langmuir, 1916;
 184 Hirth and Pound, 1963; Richter et al., 2002):

$$\frac{dn_i}{dt} = -A \frac{\alpha_e p_{i,sat} - \alpha_c p_i}{\sqrt{2\pi RMT}}, \quad (1)$$

185 Here, $\frac{dn_i}{dt}$ is the flux (mol/s), A the surface area (m^2), $p_{i,sat}$ is the equilibrium partial pressure of the
 186 gas species of element i (Pa) and M its molar mass (kg/mol), p_i its partial pressure at the surface, α_e
 187 and α_c the dimensionless Langmuir coefficients for evaporation and condensation respectively, R the
 188 gas constant (J/mol.K) and T absolute temperature.

189 Langmuir evaporation ($p_{i,sat} \gg p_i$) involves liquid-gas equilibrium only at infinitesimally small
 190 intervals, after which each parcel of gas is removed from the system, rendering it thermodynamically
 191 irreversible. Theoretically, the HKL equation implicitly assumes thermal equilibrium between liquid
 192 and gas. The high thermal mass of the surrounding gas with respect to sample in the furnace hotspot
 193 satisfies this condition, under which the HKL equation accurately describes the Langmuir evaporation
 194 flux (Littlewood and Rideal, 1956; Persad and Ward, 2016).

195 The evaporation rate is maximal when $p_i = 0$ (eq. 1). Though not measurable in these experiments, p_i
 196 relates to the accumulation of molecules of i at the evaporating surface and hence depends on the
 197 evaporation rate relative to the transport rate of i away from the surface. At our experimental
 198 conditions, element evaporation rates are relatively slow ($\approx 10^{-4}$ cm²/s) relative to transport rates,
 199 which are due to both diffusion and advection, and are of the order of several cm²/s (Electronic Annex
 200 B). In this limit the gas is instantaneously removed from the locus of evaporation, maintaining $p_i \approx 0$
 201 and, for a sphere, eq. 1 reduces to:

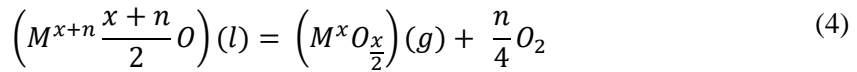
$$dn_i = -4\pi r^2 \frac{\alpha_e p_{i,sat}}{\sqrt{2\pi RMT}} dt. \quad (2)$$

202 Dividing eq. 2 by the total number of moles n_T^0 , since $\left(\frac{n_i}{n_T^0}\right) = X_i$ and $n_T^0 = \frac{4\pi r^3 \rho}{3M}$, gives:

$$dX_i = -\alpha_e p_{i,sat} \frac{3}{r\rho} \sqrt{\frac{M}{2\pi RT}} dt. \quad (3)$$

203 Element loss rate is also affected by the radius (r) and density (ρ) of the sample (eq. 3). A factor of 2
 204 variation in r results in differences in concentration of $\leq 7\%$, and, because the major elements (Si,
 205 Mg, Fe, Al and Ca) are non-volatile in the experiments, ρ is near-constant (Electronic Annex B).
 206 Thus, $r = 0.001$ m was used for all experiments and ρ was calculated for each run using the model of
 207 Bottinga and Weill (1970) and varied between 2761 and 2905 kg/m³.

208 Though the equilibrium partial vapour pressure, $p_{i,sat}$, is not directly measurable in these kinetic
 209 experiments, it may be calculated from equilibrium thermodynamics if the chemical reaction(s)
 210 describing the vaporisation are known. In the general case of the evaporation of a metal oxide species
 211 dissolved in the melt, $(M^{x+n} \frac{x+n}{2} O)(l)$, to a gaseous species that may have a different valence
 212 state, $(M^x O_{\frac{x}{2}})(g)$, the reaction is:



213 Here, M is the metal, x its formal charge (an integer value) and n the number of electrons in the
 214 reaction. Because the evaporating gas is tenuous, we assume ideal gas behaviour, such that $f = p$.
 215 The equilibrium constant of eq. 4, $K_{(4)}$, re-arranged to solve for p , the partial pressure of $M^x O_{\frac{x}{2}}$ in the
 216 gas, is:

$$p(M^x O_{\frac{x}{2}}) = \frac{K_{(4)} X(M^{x+n} O_{\frac{x+n}{2}}) \gamma(M^{x+n} O_{\frac{x+n}{2}})}{f(O_2)^{n/4}}. \quad (5)$$

217 In eq. 5, X and γ refer to the mole fraction and activity coefficient, respectively, of $M^{x+n} O_{\frac{x+n}{2}}$ in the
 218 liquid. For clarity, we make the substitution $i = M^{x+n} O_{\frac{x+n}{2}}$. We take the standard state as that of the
 219 pure liquid oxide at the temperature and pressure of interest. We assume that the concentration of an
 220 evaporating element is in the Henry's law region, such that its activity coefficient, γ_i , is equivalent to
 221 that at infinite dilution, γ_i^∞ . Where $\gamma_i^\infty = 1$, the solution of component i in the liquid is ideal.
 222 Likewise, when the Langmuir evaporation coefficient α_e is unity, Langmuir evaporation is considered
 223 ideal. As the values of α_e and γ_i^∞ are not known *a priori*, it is convenient to define a modified
 224 equilibrium constant, K^* :

$$K^* = \alpha_e \gamma_i^\infty K. \quad (6)$$

225 It is the composite parameter K^* that will be determined from the experiments. For some elements, K
 226 and γ_i^∞ are known from independent equilibrium thermochemical measurements, allowing α_e to be
 227 calculated using eq. 6. Alternatively, if α_e is defined then γ_i^∞ may be computed by the quotient K^*/K .
 228 With this simplification, eqs. 5 and 6 may be substituted into eq. 3, giving:

$$dX_i = -\frac{K_{(4)}^*}{f(O_2)^{n/4}} \frac{3}{r\rho} \sqrt{\frac{M}{2\pi RT}} dt \quad (7)$$

229 Integrating eq. 7 with respect to dX_i and dt yields:

$$\frac{X_i^t}{X_i^0} = \exp\left(-\frac{K_{(4)}^*}{f(O_2)^{n/4}} \frac{3}{r\rho} \sqrt{\frac{M}{2\pi RT}} (t - t_0)\right) \quad (8)$$

230 Equation 8 returns the mole fraction of element i remaining in the melt after a given time, t , (X_i^t)
 231 relative to its initial mole fraction X_i^0 , a ratio that is experimentally-measured. It has three refinable
 232 parameters: the physically significant quantities K^* and n , and t_0 , a lag time that depends on the
 233 experimental arrangement (*e.g.*, heating time). They are found by minimising the misfit of $\frac{X_i^t}{X_i^0}$
 234 calculated by eq. 8 to the measured value, summed over a set of N experiments at a single temperature
 235 and run time but variable fO_2 by non-linear least squares:

$$\chi^2(K^*, n, t_0) = \sum_N \left(\frac{\left(\frac{X_i^t}{X_i^0} \right)_{meas} - \left(\frac{X_i^t}{X_i^0} \right)_{calc}}{s \left(\frac{X_i^t}{X_i^0} \right)_{meas}} \right)^2, \quad (9)$$

236 where s denotes the standard deviation. The values of K^* and n are derived solely from fits to the
 237 experimental data using eq. 9 and do not depend on any *a priori* knowledge of thermodynamic
 238 quantities. By default, t_0 is set to 0 but is refinable within the limits $0 \leq t_0 \leq t$.

239 Plotted against $\log fO_2$, $\frac{X_i^t}{X_i^0}$ varies as a sigmoid, where n determines the slope. If the oxidation state of
 240 an element in the melt is known, then that in the gas may be inferred from the slope of the curve
 241 defined by the experimental data. If $n > 0$, the oxidation state of the element in the gas is lower than
 242 that in the liquid, and vice-versa. The change in element volatility with fO_2 becomes sharper (steeper
 243 slopes) as n diverges from 0. The K^* controls the displacement of the curve along the $\log fO_2$ axis,
 244 where higher values of K^* result in lower $\frac{X_i^t}{X_i^0}$ (*i.e.*, more evaporative loss), all else being equal. At
 245 constant temperature, a systematic increase of K^* with run time signals a non-zero t_0 (evaporation
 246 begins only after some time, t_0).

247 Values of $p_{i,sat}$ reflect the sum of each of the possible vaporisation reactions that may be written
 248 between all relevant components containing i in the melt, and all gas species containing i in the
 249 vapour. If the element of interest has a given number, N_{liq} of valence states in the melt and N_{gas}
 250 species in the gas, there will be $(N_{liq}+N_{gas}-1)$ independent reactions (*e.g.*, one reaction if $N_{liq}=1$ and
 251 $N_{gas}=1$). We identify five possible scenarios in order of increasing complexity:

- 252 1) Congruent associative evaporation with one species in both liquid and gas, the species
 253 having the same oxidation states ($n=0$).

254
$$\frac{x_i^t}{x_i^0} = \exp\left(-K^* \frac{3}{r\rho} \sqrt{\frac{M}{2\pi RT}} (t - t_0)\right) \quad (10)$$

- 255 2) Congruent dissociative evaporation with one metal-bearing species in both liquid and gas,
 256 the species having different oxidation states ($n \neq 0$). Elemental loss is given by eq. 8.
 257 3) Congruent dissociative evaporation with a single oxidation state in the liquid and multiple
 258 in the gas.

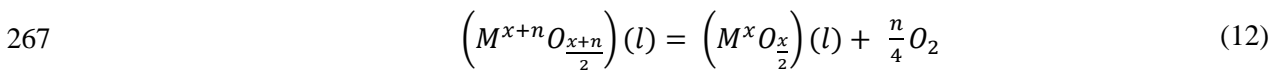
259 This equation is a sum of the partial pressures of the gas species involved in the
 260 vaporisation of a given element:

261
$$\frac{x_i^t}{x_i^0} = \exp\left(-\left(\frac{K_{(4a)}^*}{f(O_2)^{na/4}} + \frac{K_{(4b)}^*}{f(O_2)^{nb/4}}\right) \frac{3}{r\rho} \sqrt{\frac{M}{2\pi RT}} (t - t_0)\right) \quad (11)$$

262 Where a and b refer to the different stoichiometries of eq. 4.

- 263 4) Congruent dissociative evaporation with multiple oxidation states in the liquid and a
 264 single gas species.

265 The homogeneous equilibrium between two melt oxide components with different
 266 oxidation states may be written:



268 The $\log K_{(12)}^*$ is related to the equilibrium constant in the pure M-O system by the
 269 equation:

270
$$\log K_{(12)}^* = \log K_{(12)} - \log\left(\frac{\gamma\left(M^{x+n}O_{\frac{x+n}{2}}\right)}{\gamma\left(M^xO_{\frac{x}{2}}\right)}\right). \quad (13)$$

271 The melt oxide components $\left(M^{x+n}O_{\frac{x+n}{2}}\right)$ and $\left(M^xO_{\frac{x}{2}}\right)$ are denoted i and j respectively.

272 Expressions for the partial pressure of a given gas species can be substituted into eq. 3
 273 (see Appendix A for derivation) and integrated in a manner identical to that for eq. 8 to
 274 give:

275
$$\frac{x_i^t}{x_i^0} = \exp\left(-\frac{\alpha_e \gamma_j K_{(4)} f(O_2)^{-n_{(4)}/4}}{\left(K_{(12)} f(O_2)^{n_{(12)}/4} \frac{\gamma_j}{\gamma_i} + 1\right)} \frac{3}{r\rho} \sqrt{\frac{M}{2\pi RT}} (t - t_0)\right) \quad (14)$$

276 Although $K_{(12)}$ is given by thermodynamic data in the pure metal oxide system, eq. 14 has an
 277 additional degree of freedom, the ratio of the melt oxide activity coefficients, $\frac{\gamma_j}{\gamma_i}$. Therefore eq. 14
 278 requires independent knowledge of $\frac{\gamma_j}{\gamma_i}$ to be able to solve uniquely for K^* .

279 5) Congruent dissociative evaporation with multiple oxidation states in the liquid and in the
 280 gas.

281 This equation is the sum of the partial pressures of two gas species as derived in eq. 14

282
$$\frac{x_i^t}{x_i^0} = \exp\left(-\left(\left(\frac{\alpha_e \gamma_j K_{(4a)} f(O_2)^{-n_{(4a)}/4}}{\left(K_{(12)} f(O_2)^{n_{(12)}/4} \frac{\gamma_j}{\gamma_i} + 1\right)}\right) + \left(\frac{\alpha_e \gamma_j K_{(4b)} f(O_2)^{-n_{(4b)}/4}}{\left(K_{(12)} f(O_2)^{n_{(12)}/4} \frac{\gamma_j}{\gamma_i} + 1\right)}\right)\right) \frac{3}{r\rho} \sqrt{\frac{M}{2\pi RT}} (t - t_0)\right) \quad (15)$$

283 These equations may be applied to any element. New evaporation experiments in the future would
 284 provide additional tests on the theory developed herein.

285 4.0. Results

286 A total of 48 experiments were performed at temperatures of 1300, 1400, 1500 and 1550 °C with run
 287 durations of 15, 60, 120, 720 and 930 minutes and $\log fO_2$ s between air (-0.68) and -10 (Table 2). All
 288 experiments quenched to homogeneous glasses (Fig. 1), with the exception of some of the 1300 °C
 289 experiments at low fO_2 , which contain $\approx 5\%$ microphenocrysts of olivine and spinel (Electronic Annex
 290 C), suggesting the liquidus temperature is close to 1300 °C. Samples run on Pt loops at low fO_2
 291 experienced minor ($\approx 5\%$) Fe loss to the wire (Electronic Annex C).

292 4.1. Contamination and blank runs

293 Four experiments performed at $\log fO_2 = -8$ ($N = 3$) and -0.68 ($N = 1$) at 1400°C and 1500°C on the
 294 FCMAS mixture without trace elements ('blank' runs) were analysed to quantify any contamination
 295 within the furnace. At $\log fO_2 = -8$, the concentrations of all 20 trace elements were $< 1\%$ of 1000
 296 ppm, with an average of 1.8 ppm (Table 2). These values indicate negligible vapour pressures of
 297 volatile elements in the furnace hotspot, ruling out re-condensation and verifying the condition $p_i \approx$
 298 0. In the air experiment (P28/05/18), all elements are present below 3 ppm, excepting Na and K at
 299 92.1 ppm and 77.7 ppm. That Na and K should not have appreciably evaporated after 15 minutes at
 300 1400°C in air suggests they occur as impurities in the major oxides.

301 In the trace element-bearing experiments, abundances of K and particularly Na, increased through
 302 contamination up to 2075 and 20028 ppm from their initial concentrations of 944 ± 128 ppm and
 303 3252 ± 281 ppm in the starting mixture, respectively. Contamination affected only the samples run at

304 WWU Münster, likely reflecting the experimental history of the furnace and/or its alumina muffle
305 tube. As such, only the experiments performed at RSES ANU (C-17,18/12/15) and IPGP, Paris (P-
306 xx/xx/17,18), which have low background Na contents (Table 2; Tuff and O'Neill 2010) are
307 considered for Li, Na and K.

308 *4.2. Experimental reproducibility*

309 We duplicated four experiments at 1400°C (Table 2). Experiments for pair P09-06-18b and P09-06-
310 18a, were run on Pt- and Re loops, respectively. The concentrations of volatile elements (K, Cr, Cu,
311 Zn, Ga, Ge, Rb, Mo, Ag, Cd, Pb; N = 38) are compared in Fig. 2 and adhere closely to the 1:1 line.
312 The median misfit between the four pairs for elements with non-zero (> 5 ppm) concentrations is 6.0
313 % relative. This is two- to three-times larger than the analytical RSD (see section 2.2.), reflecting the
314 experimental error. These random errors include the mass and shape of the experimental charge
315 (section 3.0.; Electronic Annex B) as well as measurement of the temperature, run duration and fO_2
316 (section 2.2.).

317 *4.3. Metal Loops*

318 Because the solubility of an element into metal increases as fO_2 decreases, depletion of some elements
319 in the glasses at low fO_2 may be partially attributable to alloying with noble metal wires. In order to
320 test this hypothesis, the trace element content of wires in 10 experiments (Table 2) were analysed
321 (Electronic Annex C).

322 No elements other than the metal were detected in the Ir loop experiment (C18/12/15) and three Re
323 loop experiments measured (1M-1/3/16, 1M-1/3/16b and C17/12/15c). For Pt loop experiments, Ga
324 and Cu dissolved into Pt metal, along with very minor Ag ($Ag/Pt < 2 \times 10^{-4}$) and Pb ($Pb/Pt < 7 \times 10^{-4}$) in
325 experiments 1M-PS4, 1M-PS5 and 2M-15-07-16f. This latter pair is so volatile that their abundances
326 were already negligible in silicate liquid.

327
328 Although Ga/Pt ratios are typically $< 7 \times 10^{-4}$, in one sample, 2M-17-07-16c ($\log fO_2 = -8$, $T = 1500^\circ C$, t
329 = 60 mins), Ga/Pt reaches $2.4(\pm 0.1) \times 10^{-3}$. The melt is also strongly depleted in Ga (67.4 ppm) with
330 respect to the run at $\log fO_2 = -5.5$ (775.1 ppm). Gallium abundances in Pt loops (P09-06-18b) and Re
331 loops (P09-06-18a) at 1400°C and $\log fO_2 -9.23$ are similar (439.9 ppm and 409.4 ppm), suggesting
332 that partitioning of Ga into Pt wire has no resolvable influence on the quantity measured in the melt.

333
334 The Cu/Pt ratios of the Pt wire reach $4.7 \pm 2.9 \times 10^{-3}$, but are highly heterogeneous, reflecting the low
335 diffusion coefficient of Cu in Pt, $10^{-13} \text{ m}^2/\text{s}$ at 1673 K (Liu et al., 2009). For a 15-minute experiment,
336 Cu would have diffused only 9 μm into the 0.1 mm diameter Pt wire. For a 0.5 cm length with mass
337 of 0.84 mg ($\approx 7\%$ of sample mass), the Cu budget in the wire, assuming 4000 ppm in the affected
338 zone, is 9%. Experiments P09-06-18b (Pt) and P09-06-18a (Re) have similar Cu contents of 40.5 and

339 11.2 ppm, respectively. It is concluded that the partitioning of any given element into the metal wire
340 has no resolvable effect within experimental error ($\pm 6\%$ relative) on its observed depletion in the
341 silicate melt.

342

343 4.4. Elemental Zoning

344 Implicit in the theoretical framework in *section 3.0.* is the homogeneous distribution of evaporating
345 elements in the liquid. To test homogeneity, element concentrations were measured in each sample
346 with at least three 130 μm laser spots in both the core and rim, often with a few points in between (N
347 = 6-12; Fig. 1). In addition, a representative subset of seven samples (two each at 1300°C, 1400°C,
348 1500°C and one at 1550°C; Table 2; Electronic Annex C) were analysed in detail by taking linear
349 profiles from rim to core, consisting of ten to fifteen 25 μm spots spaced at 50 μm intervals (Fig. 3a).

350 Excepting one sample, 2M-15-07-16f, which represents the extremes of lowest temperature (1300
351 °C), $f\text{O}_2$ (10^{-10} bar) and shortest run time (15 mins) of the experiments, all elements in all other
352 samples measured show no analytically-resolvable compositional zoning from core to rim (Fig. 3b
353 and Electronic Annex C). Homogeneous zoning profiles indicate that the characteristic timescale of
354 evaporation, t_{HKL} , found by solving for t in eq. (8), is greater than the diffusive timescale,
355 approximated by $t_D = r^2/2D$, where D is the diffusion coefficient (see Electronic Annex D). The lack
356 of zoning can therefore set lower limits on the value of D . In sample 2M-15-07-16f, the extent of
357 element zoning is inversely proportional to the fraction remaining after volatile loss. This suggests
358 zoning is more pronounced for elements with higher evaporation rates relative to their diffusion rates.
359 This ratio increases (and hence zoning is more likely) for most elements to lower $f\text{O}_2$, because
360 vaporisation rates increase whereas diffusion rates are constant as long as the melt oxide species is
361 unchanged. Accordingly, only sample 2M-15-07-16f was rejected from the dataset. For the remaining
362 experiments, diffusion in the liquid was not the rate-limiting step controlling measured element
363 abundances, thereby leaving evaporation from the surface.

364 4.5. Data fitting

365 Three groups of elements can be classified *i)* ‘non-volatile’ elements (Mn, Sc, Ti, V, Zr and the REEs)
366 for which no statistically discernible change from their initial concentrations is observed, *ii)* volatile
367 elements that become relatively more volatile with decreasing $f\text{O}_2$ ($n > 0$; Na, K, Cu, Zn, Ga, Ge, Rb,
368 Pb, Ag, Cd) and *iii)* volatile elements that become relatively more volatile with increasing $f\text{O}_2$ ($n < 0$;
369 Cr, Mo). Lithium is similarly volatile over the range of $f\text{O}_2$ investigated. At a given $f\text{O}_2$, loss of
370 elements belonging to groups *ii)* and *iii)* also increases with a) temperature and b) run time. Values of
371 t_0 , n and $\log K^*$ fitted to the data for all volatile elements are shown in Table 3.

372 4.5.1. Congruent Dissociative Evaporation with one metal-bearing species in both
373 liquid and gas, the species having different oxidation states

374 *One electron (n = 1) reactions (Na, K, Rb, Cu, Ag)*

375 The order of alkali volatility observed in the experiments increases down the group; $\text{Li} < \text{Na} < \text{K} < \text{Rb}$
376 (Fig. 4a-c), in line with the equilibrium vapour pressures above their pure oxides (Lamoreaux and
377 Hildenbrand, 1984). All alkali metals exist in silicate melts as $\text{M}^+\text{O}_{0.5}$ species (*e.g.*, Charles 1967).
378 Lithium is dealt with separately owing to its distinct vaporisation behaviour.

379 At 1400 °C, sodium and potassium become increasingly volatile at low $f\text{O}_2$ (Fig. 4a, b). This
380 behaviour results from a lower mean valence state of these elements in the gas compared to the liquid.
381 Using eq. 8 to fit the data, both Na and K conform to an $n = 1$ reaction (Fig. 4a, b), implying the
382 reaction $\text{M}^+\text{O}_{0.5}(\text{l}) = \text{M}^0(\text{g}) + \frac{1}{4}\text{O}_2$ (Fig. 4a, b). This stoichiometry is supported by thermodynamic data
383 that show the overwhelming stability of the monatomic gas above $\text{Na}_2\text{O}(\text{s})$ and $\text{K}_2\text{O}(\text{s})$ (Lamoreaux
384 and Hildenbrand, 1984), and above natural silicate melts from Naughton et al. (1971), De Maria et al.
385 (1971) *via* Knudsen Effusion Mass Spectrometry (KEMS) and Tsuchiyama et al. (1981) *via* Langmuir
386 evaporation. The higher $\log K^*$ of the evaporation reaction for K (-3.95 ± 0.06) relative to Na ($-$
387 4.25 ± 0.10) at 1400°C attests to its higher volatility (Fig. 4a, b, Table 3).

388 Rubidium is more volatile than either Na or K (Fig. 4c). Like Na and K, its dependence on $f\text{O}_2$ is
389 consistent with an $n = 1$ reaction, meaning Rb^0 is the stable gas species (Lamoreaux and Hildenbrand
390 1984). In fitting the equilibrium constant of the Rb vaporisation reaction, a positive dependence of
391 $\log K^*$ with the time series (15, 60, 120 minutes) was observed. In order to account for this, an
392 experimental ‘lag time’ is introduced, which describes the time at which Rb starts evaporating after
393 sample insertion. A best fit is found at $t_0 = 14.4$ min (863 s), a constant for all time- and temperature
394 series.

395 Copper is observed to become more volatile at lower $f\text{O}_2$ (Fig. 4d), signalling a lower oxidation state
396 of Cu in the gas relative to the melt. Although copper is expected to be dominantly cuprous (Cu^+) in
397 silicate melts at very high $f\text{O}_2$ (*e.g.*, in air), it may also be present as $\text{Cu}^{2+}\text{O}(\text{l})$ (*e.g.* Schreiber 1987).
398 Only Cu^+ is detected in alkali-free, CMAS and CMAS+Fe liquids at 1300°C up to $\Delta\text{FMQ}-1.5$,
399 (Holzheid and Lodders 2001, and references therein). Nevertheless, to check for the presence of Cu^{2+} ,
400 fits to the experimental data were performed for n in eq. 8. At 1300°C, a formal valence of 1.14 is
401 calculated, at 1400°C it is 1.17, 0.84 at 1500°C, and 0.98 at 1550°C, yielding a weighted average of
402 1.06 ± 0.15 . Therefore, $\text{CuO}_{0.5}$ is the only stable liquid oxide species considered, meaning n is set equal
403 to 1, implying the stability of $\text{Cu}^0(\text{g})$.

404 Silver is in its 1+ oxidation state in silicate melts, occurring as $\text{AgO}_{0.5}(\text{l})$, however, due to its high
405 volatility, its vaporisation stoichiometry is not well constrained by the present set of experiments. The
406 few data points at 1300°C allow the expected one-electron ($n = 1$) reaction to be fit (Table 3).

407 *Two electron (n = 2) reactions (Zn, Ge, Cd)*

408 The volatility of zinc is very sensitive to fO_2 . Although it is less volatile than Cu or K in air, under
409 reducing conditions ($\leq \log fO_2 = -8$), its abundance in the melt is negligible at all temperatures (Fig
410 5a). The experimental data are best fit with an $n = 2$ reaction, reflecting the evaporation of ZnO(l), its
411 only stable melt component, to Zn⁰(g). Thermodynamic data for gases above ZnO(s) also show that
412 Zn exists as Zn⁰(g), be it below the IW buffer or in air, though ZnO(g) becomes important <1000 K in
413 air (Lamoreaux et al., 1987). As for Rb, if $t_0 = 0$ in eq. 8, then a positive dependence of $\log K^*$ with
414 time is observed. For Zn, this time dependence is removed for a time lag of 9 minutes ($t_0 = 540$ s),
415 applied to all run durations and temperatures. $\log K^*$ s increase systematically with temperature (Fig.
416 5a; Table 3).

417 The vaporisation behaviour of Ge closely mirrors that of Zn (Fig. 5b). Although in silicate liquids Ge
418 transitions to 2+ at low fO_2 , where $Ge^{2+}/\sum Ge = 0.5$ at IW and 1 atm for a CMAS composition (Mare
419 et al., 2016), it exists exclusively as Ge⁴⁺ over the fO_2 range covered in our experiments. The data are
420 best fit with an $n = 2$ reaction, implying GeO(g) is stable. This is also corroborated by thermodynamic
421 data for vaporisation of GeO₂(s) (Lamoreaux et al., 1987). Like Zn, a constant ‘time lag’ of $t_0 = 624$ s
422 (10.4 min) accounts for the observed dependence of $\log K^*$ on time. The proportion of Ge lost from
423 the melt is indistinguishable from that of Zn at 1300°C, attested to by their overlapping $\log K^*$ s (Table
424 3), but at higher temperatures Ge becomes relatively more volatile than Zn (Fig. 5).

425 Cadmium, like silver, was too volatile to permit assessment of its evaporation stoichiometry; only two
426 experiments contain measurable quantities of Cd, 2M-15-07-16c and 2M-15-07-15d, $\log fO_2 = -0.67$
427 and -3.44 , for 15 min at 1300°C, respectively. Cadmium, which occurs as Cd²⁺ in silicate melts,
428 evaporates as Cd⁰(g) over all fO_2 above CdO(s) (Lamoreaux et al., 1987) suggesting $n = 2$, the value
429 adopted for the fitting.

430 4.5.2. Congruent dissociative evaporation with a single oxidation state in the liquid 431 and multiple in the gas (Li, Ga, Pb)

432 For an element with a single melt oxidation state, and more than a single species in the gas, the total
433 partial pressure of the element in the gas phase is the sum of two or more partial pressures (eq. 11).
434 This applies to the vaporisation of Li, Ga and Pb over the T- fO_2 conditions investigated.

435 The vaporisation behaviour of Li is distinct from that of other alkali metals; it is equally volatile at
436 high fO_2 as it is at low fO_2 (Fig. 6a). The high-temperature gas species of Li above Li₂O(s) are Li(g),
437 Li₂O(g), and LiO(g) (e.g., Kimura et al. 1980), of which Li₂O(g) is the most stable (Lamoreaux and
438 Hildenbrand, 1984). However, since $p(Li_2O)$ is proportional to $a(LiO_{0.5})^2$, for $a(LiO_{0.5}) \approx 10^{-3}$ as in our
439 experiments, Li₂O is no longer the predominant gas species, leaving Li(g) and LiO(g) (see Electronic
440 Annex E). Lithium depletion is generally observed in long (≥ 120 minute) duration experiments at
441 1400°C, and only these runs are fit. The time series in air gives a $\log K^*$ for the reaction $LiO_{0.5}(l) +$

442 $\frac{1}{4}\text{O}_2 = \text{LiO(g)}$ of -3.39, whereas at $\log f\text{O}_2 = -8$ the $\log K^*$ for $\text{LiO}_{0.5}(\text{l}) = \text{Li(g)} + \frac{1}{4}\text{O}_2$ is -5.36 (Table
443 3, Fig. 6a).

444 No Ga evaporation is observed at 1300°C, but at higher temperatures Ga becomes more volatile at
445 lower $f\text{O}_2$ with close to an $n = 2$ stoichiometry (Fig. 6b). Since Ga occurs as $\text{GaO}_{1.5}$ in silicate melts,
446 there is no suitable Ga-bearing gas species that would result in an $n = 2$ reaction. Above $\text{Ga}_2\text{O}_3(\text{s})$, the
447 stable gas species is $\text{Ga}_2\text{O(g)}$ (Burns, 1966; Lamoreaux et al., 1987), whose partial pressure is
448 proportional to $f\text{O}_2$ (an $n = 4$ reaction). However, as for Li, $p(\text{Ga}_2\text{O})$ is proportional to $a(\text{GaO}_{1.5})^2$,
449 meaning its stability decreases sharply as the activity of $\text{GaO}_{1.5}$ in the melt falls (Electronic Annex E),
450 such that it is stable only below IW-1 at 1700 K for $a(\text{GaO}_{1.5}) = 10^{-3}$ (1000 ppm). Instead, the data is
451 fit by a combination of the $n = 1$ reaction involving GaO(g) and the $n = 3$ reaction with Ga(g) (Table
452 3).

453 Lead is lost rapidly from the melt, and measurable amounts remain only in runs performed at 1300°C
454 and at high $f\text{O}_2$ at 1400°C. In all cases, Pb becomes more volatile with decreasing $f\text{O}_2$ with an
455 observed value of n that is close to 1 (Fig. 6c). In silicate melts, Pb is present as Pb^{2+}O , be it at
456 oxidised ($\approx\text{NNO}$) or reduced ($\approx\text{IW}$) conditions (Watson et al., 1997; Wood and Halliday, 2010).
457 Evaporation of pure PbO(s, l) shows that Pb(g) is dominant below IW, both Pb(g) and PbO(g) are
458 found between IW and air, above which the oxidised species predominates (Lamoreaux et al., 1987;
459 Kobertz et al., 2014; Kobertz, 2019a). As such, both the $n = 0$ and $n = 2$ reactions are fit to the
460 experimental data. The partial pressures of Pb(g) and PbO(g) are found to be similar (Table 3) to
461 reproduce the $n \approx 1$ slope of the data.

462 4.5.3. Congruent dissociative evaporation with multiple oxidation states in the
463 liquid and a single gas species (Mo)

464 Oxygen fugacity may also influence the oxidation state of a metal oxide dissolved in a silicate melt.
465 This is the case for molybdenum, whose two silicate melt components, $\text{Mo}^{4+}\text{O}_2(\text{l})$ and $\text{Mo}^{6+}\text{O}_3(\text{l})$
466 (Holzheid et al., 1994; O'Neill and Eggins, 2002) are related by $(f\text{O}_2)^{1/2}$ (see Appendix A).

467 Unlike the aforementioned elements, Mo becomes increasingly volatile at increasing $f\text{O}_2$ (Fig. 7a),
468 reflecting the higher mean oxidation state of Mo in the gas phase compared to the silicate melt.
469 Because the melt has $\text{Mo}^{4+}/\sum\text{Mo} < 1$, this behaviour implies the presence of $\text{Mo}^{6+}\text{O}_3(\text{g})$. Indeed,
470 calculation of Mo gas species from thermodynamic data (Chase, 1998) shows the clear predominance
471 of $\text{MoO}_3(\text{g})$ at all $f\text{O}_2 > \text{IW}-2.5$ (Electronic Annex E), and hence only this species is considered in
472 fitting the experimental data.

473 Because $\text{Mo}^{4+}/\text{Mo}^{6+}$ of the melt decreases with $(f\text{O}_2)^{1/2}$, the effective value of n must also decrease as
474 $f\text{O}_2$ increases. This behaviour necessitates the use of eq. (14) to fit the data. Unique solutions for
475 $p(\text{MoO}_3)$ require that $\gamma(\text{MoO}_3)$ and $\gamma(\text{MoO}_2)$ are known. Here, a value of $\gamma(\text{MoO}_3) = 0.3$ is chosen

476 from CMAS liquids (O'Neill and Eggins, 2002). The slope of the data (n) with fO_2 depends on
477 $\gamma(MoO_3)/\gamma(MoO_2)$, with a best fit across the experimental range found at a ratio of 20.7. These
478 assumptions render the values for the $\log K^*$ s listed in Table 3 approximate.

479 4.5.4. Congruent dissociative evaporation with multiple oxidation states in the
480 liquid and in the gas (Cr)

481 Chromium, like Mo, becomes more volatile from silicate melts at increasing fO_2 (Fig. 7b) because Cr
482 in the gas has a higher mean valence than in the liquid. In the liquid, both Cr^{2+} and Cr^{3+} occur (*cf.*
483 Berry and O'Neill 2004), while four Cr-bearing gas species are stable at high temperatures; Cr(g),
484 CrO(g), CrO₂(g) and CrO₃(g). However, only CrO₂(g) is important for $IW < fO_2 < FMQ+3$, with
485 CrO₃(g) only becoming dominant in air, though its stability increases to lower temperatures (see
486 Electronic Annex E). Tungsten also has oxidised gas species; WO₂ and WO₃ (see also Fegley and
487 Palme 1985; O'Neill 1991), indicating that this is a general feature of Group VI metals.

488 Two conditions are imposed in the fitting *i*) $\gamma(CrO) = 3$ (Pretorius and Muan, 1992) and *ii*) the
489 $\gamma(CrO_{1.5})/\gamma(CrO)$ ratio at 1400 °C is fixed at 6.13 to give a $\log K^*$ of 2.26 for the equilibrium $CrO(l)$
490 $+ \frac{1}{4}O_2 = CrO_{1.5}(l)$ (at an optical basicity of 0.645 for the ferrobalt; Berry et al. 2006) and is taken to
491 remain constant at all temperatures. Fitting with CrO₃(g) did not improve the misfit and was therefore
492 neglected, hence the data was fit using eq. (14) with CrO₂(g) as the stable species. The 1300°C
493 experiments are anomalously more depleted than at higher temperatures and were not fit. For these
494 reasons, the $\log K^*$ s derived from fitting Cr data shown in Table 3 are semi-empirical.

495

496 4.6. Evaporation coefficients and activity coefficients of metal oxide species in silicate melts

497 In these experiments, gas speciation and thus reaction stoichiometries were not measured, but inferred
498 from fits to concentration- T - fO_2 relations (Figs. 4 – 7), the potential complexity of which limits the
499 extraction of reliable thermodynamic quantities (K^* , n) to elements with simple vaporisation
500 stoichiometries (eq. 8, 10). The sum of the experimental uncertainties that may affect precise
501 determination of K^* and n , including sample properties (size, shape, density) and other kinetic factors
502 that may influence vaporisation rate (diffusion-limited evaporation, gas flow rate), is relatively small
503 ($\pm 6\%$; section 4.2.). As the determination of n relies on how $\left(\frac{x_i^t}{x_i^0}\right)$ changes relative to other
504 experiments in a given fO_2 series, it depends only on these random experimental variables and is
505 derived with good precision and accuracy.

506 An additional experimental uncertainty arises for Rb, Zn and Ge because of the time lag from sample
507 insertion to vaporisation ($t_0 = 9 - 14$ minutes; Table 3), which almost coincides with measured heating
508 times (4 – 7 minutes, section 2.1.). In equilibrium techniques such as KEMS, it is routine to run a

509 standard material with known partial pressures under identical conditions (Margrave, 1967; Drowart
510 et al. 2005) to identify any systematic errors (*e.g.*, choice of r , effect of t_0 , deviations from Langmuir
511 conditions), thereby calibrating K^* values. This was not done for these experiments. Therefore,
512 although K^* values are relatively precise ($\approx \pm 5\%$ to $\pm 30\%$; Table 3), their accuracy is harder to
513 quantify.

514 Here, accuracy is assessed by comparing the experimentally-determined equilibrium constant of the
515 vaporisation reaction of the oxide component from silicate melts (K^*), with the known equilibrium
516 constant for the equivalent vaporisation reaction of the pure oxide (K) calculated from thermodynamic
517 data (*e.g.*, Lamoreaux et al. 1987; Chase 1998; Glushko et al. 1999). The values K^* and K are related
518 by eq. 6, and are not equivalent if γ_i^∞ or α_e deviate from unity. For $\frac{K^*}{K} > 1$ the vapour species is
519 favoured over the liquid component of the silicate melt relative to the same reaction between the pure
520 liquid oxide and gas, and vice-versa.

521 Activity coefficients of metal oxide species in silicate melts vary by orders of magnitude with
522 composition (*e.g.*, Rammensee and Fraser 1982; Wood and Wade 2013), temperature (*e.g.*, Reyes and
523 Gaskell 1983) and metal oxidation state (O'Neill and Eggins, 2002), with theoretical limits between
524 $1/\infty < \gamma_i < \infty$. However, for many trace elements, activity coefficients remain poorly known.
525 Constraints on Langmuir evaporation coefficients are similarly sparse. Because the HKL equation
526 describes only the flux of particles striking a surface, α_e was introduced *a posteriori* as an *ad-hoc*
527 adjustment to account for the energy required in the transformation of element i from the condensed
528 to gaseous state (see Ackermann et al. 1962) and thus has theoretical limits $1/\infty < \alpha_e \leq 1$. Unlike γ_i ,
529 α_e may depend not only on liquid composition, temperature and redox state, but also on the activation
530 energy of evaporation, surface properties, vaporisation rate and nature of the gas phase (*e.g.*, Knacke
531 and Stranski 1956; Persad and Ward 2016) and hence cannot be determined *ab-initio*. Although
532 evaporation coefficients from simple solid metal or binary metal oxides are < 1 , the equivalent liquids
533 have α_e of unity (Burns, 1966; Safarian and Engh, 2013; Shornikov, 2015). For vaporisation of major
534 components from silicate melts Alexander (2002) and Fedkin et al. (2006) employed MELTS to
535 calculate γ_i and found $0.01 < \alpha_e < 0.5$ from fits to experimental data. Given the potential variation of
536 α_e and γ_i^∞ in our system, values of α_e are calculated using independent estimates of γ_i , providing a
537 test of the accuracy of our theoretical framework (section 3.0.).

538 Evaporation coefficients calculated from eq. 6 are shown in Table 4. The activity coefficients of Na
539 and K are well-characterised (O'Neill, 2005; Grant and Wood, 2008; Borisov, 2009; Mathieu et al.,
540 2011) due to their importance in the vaporisation of chondrules (*e.g.*, Tsuchiyama et al. 1981;
541 Shimaoka and Nakamura 1991; Georges et al. 2000) and lunar basalts (De Maria et al., 1971; Gibson
542 and Hubbard, 1972; Gooding and Muenow, 1976; Donaldson, 1979). From the Na vapour pressures
543 measured over natural basalts by DeMaria et al. (1971) and Gooding and Muenow (1976), activity

544 coefficients $\approx 10^{-3}$ were calculated. Mathieu et al. (2008) also report $\gamma_{NaO_{0.5}} = 10^{-3}$ in the CMAS
 545 system and $8.4 \times 10^{-4} - 2.2 \times 10^{-3}$ in the simpler CMS system (Mathieu et al., 2011). This gives $\alpha_{e,NaO_{0.5}}$
 546 between 0.3 – 1.7 for our experiments at 1400 °C. Values of $\gamma_{KO_{0.5}} \approx 5 \times 10^{-5}$ to 7×10^{-4} were calculated
 547 from De Maria et al. (1971), Gooding and Muenow (1976) in natural basalts and Hastie and Bonnell
 548 (1985) for the KFCAS system, resulting in $\alpha_{e,KO_{0.5}}$ from 0.3 to 3.4 at 1400 °C.

549 Reyes and Gaskell (1983) found $\gamma_{ZnO} = 0.25, 0.43,$ and 0.58 at 1400, 1500 and 1550 °C, respectively
 550 in CAS melts by transpiration, yielding $\alpha_{e,ZnO} \approx 2$. Holzheid and Lodders (2001) determined $\gamma_{CuO_{0.5}}$
 551 $= 10 \pm 1$ at 1300°C for Fe-poor basaltic compositions, returning $\alpha_{e,CuO_{0.5}} = 2.4 \pm 0.8$. If the trends of K^*
 552 are extrapolated with temperature to 1650°C, then the $\gamma_{CuO_{0.5}} = 3.5$ determined by Wood and Wade
 553 (2013) at this temperature gives $\alpha_{e,CuO_{0.5}} = 1.2$. The two stable gases species evaporating over PbO(l)
 554 allows $\alpha_{e,PbO}$ to be calculated from both reactions (Table 4). Although the two points for Pb
 555 evaporation do not permit extrapolation to higher temperatures, $\alpha_{e,PbO}$ ranges between 0.3 and 1.7
 556 when calculated from γ_{PbO} of Wood and Wade (2013), 0.22, at 1650°C for an SiO₂-rich melt.

557 Therefore, evaporation coefficients are close to unity (within a factor of 2 - 3) for all elements for
 558 which *i*) the experimentally determined K^* is robust, *ii*) melt compositions and temperatures are
 559 similar to literature data, and *iii*) the activity coefficient is well-determined (particularly Na, Cu and
 560 Zn). Based on these observations α_e is set to 1 and γ_i^∞ is calculated from K^*/K (eq. 6; Table 4, Fig.
 561 8). The uncertainties on the reported activity coefficients represent only the precision on the fit, and
 562 do not include the uncertainties in α_e just discussed.

563 Aside from Li, alkali dissolution in silicate melts is strongly non-ideal ($\gamma_i^\infty \ll 1$), meaning their
 564 volatilities are much reduced from those of pure alkali oxides. Furthermore, alkali metal oxide activity
 565 coefficients decrease in the order $Li \gg Na > K > Rb > (Cs)$ (*cf.* Charles, 1967; Borisov, 2009), a hierarchy
 566 that is inversely proportional to their volatilities.

567 Zinc oxide activity coefficients, like other divalent, first-row transition metals (O'Neill and Eggins,
 568 2002), are close to unity but show a weak positive dependence on temperature. This behaviour is
 569 mimicked by $\gamma_{GeO_2}^\infty$, albeit at lower absolute values. By contrast, $\gamma_{CuO_{0.5}}^\infty$ is >1 , (see also Holzheid et
 570 al., 2001; Wood and Wade, 2013), and decreases to higher temperatures. In these three cases, γ_i^∞
 571 tends towards unity at high temperatures, a phenomenon described by the van't Hoff equation:

$$\frac{d \ln \gamma_i^\infty}{d(1/T)} = - \frac{\Delta H}{R}, \quad (16)$$

572 where ΔH refers to the partial molar enthalpy of solution of *i* in the silicate melt. For CuO_{0.5}, this is
 573 calculated at 121 ± 12 kJ/mol, -143 ± 15 kJ/mol for ZnO (compared with -135 kJ/mol from Reyes and
 574 Gaskell, 1983) and -147 ± 25 kJ/mol for GeO₂ over the temperature range 1573 to 1823 K.

575

576 4.7. Gibbs Free Energy of vaporisation using the ‘2nd law method’

577 The modified equilibrium constants of vaporisation reactions (K^*) may be converted into Gibbs Free
578 Energies (ΔG^*):

$$\Delta G^* = -RT \ln K^*. \quad (17)$$

579 The asterisk denotes that the Gibbs Free Energy of reaction includes *i*) the non-ideality of trace
580 element dissolution in silicate melts and *ii*) any deviation of the evaporation coefficient from unity
581 and/or variation with temperature. Hence, ΔG^* s calculated are relevant only to the investigated melt
582 composition at 1 bar pressure and temperatures between 1573 and 1823 K.

583 Variation of ΔG^* of a volatilisation reaction against the absolute temperature, T , in an Ellingham
584 diagram, results in a straight line (Fig. 9), independent of run time. This confirms that a reproducible,
585 thermally-activated process is controlling elemental loss, namely, the equilibrium partial pressure.

586 At constant total pressure, the Gibbs-Helmoltz equation is:

$$\Delta G^* = \Delta H^* - T\Delta S^* \quad (18)$$

587 Hence, the slope of the line is equivalent to $-\Delta S^*$ (entropy) and its intercept ΔH^* (enthalpy), which
588 are average values determined for the mid-point temperature over the temperature range. This is a 2nd
589 law treatment of the vaporisation data, requiring two or more measurements of the equilibrium
590 constant, and is analogous to the integration of the Clausius–Clapeyron equation generally used for
591 interpretation of vapour pressure data (Drowart and Goldfinger, 1967; Drowart et al., 2005; L’vov,
592 2007). It implicitly assumes that ΔH^* is much greater than the product of ΔC_p^0 (molar heat capacity at
593 constant pressure) and temperature over the interval of interest, such that slopes can be approximated
594 as linear within experimental uncertainty.

595 Values for the entropy and enthalpy of reaction, along with those for the pure system, are listed in
596 Table 5. Typical relative standard deviations for ΔH^* and ΔS^* range from 5 – 15 %, as compared with
597 1 – 2 % for KEMS measurements for vaporisation of multicomponent systems (silicate melt, Markova
598 et al., 1986, Fraser and Rammensee, 1987; olivine, Costa et al. 2017) or pure metal oxides (Kobertz
599 2019a, b). It is observed that ΔH^* and ΔS^* are positively correlated (Fig. 10a), indicative of enthalpy-
600 entropy compensation, where ΔG tends to a common value at infinite temperature (see Exner 1973;
601 Kemeny and Rosenberg 1973). The same is true of thermodynamic data in the pure M-O system,
602 though less marked (compare Fig. 10a and b). The gross effect of γ_i^∞ is to smooth out variability in
603 ΔH^* vs. ΔS^* compared with ΔH^0 and ΔS^0 . Activity coefficients of divalent first-row transition metal
604 cations are ≈ 1 in geologically-relevant silicate melts (Pretorius and Muan, 1992; Ohta and Suito,
605 1995; Holzheid et al., 1997; O’Neill and Eggins, 2002) and furthermore depend on melt composition

606 in a similar manner (O'Neill and Eggins, 2002). With these caveats in mind, their ΔH^o and ΔS^o from
 607 pure system thermodynamic data (Chase, 1998) are also shown in Table 5.

608 4.8. Comparison with previous work

609 Tsuchiyama et al. (1981) studied Na evaporation from chondrule-like melts at varying $\log fO_2$ (-5 to -
 610 10) between 1450 and 1600 °C (Fig. 11a). Their data are well-modelled by eq. (8), conforming to an n
 611 = 1 reaction with $\log K^*$ s that define $\Delta G^* = 444.4(\pm 0.2) - 0.166(\pm 0.003)T$ (kJ/mol) for their
 612 'composition 1'. Na evaporation from 'composition 2', with SiO_2 (43.55 wt. %) and FeO^T (18.52 wt.
 613 %) contents similar to the ferrobalt, has $\log K^*$ 0.5 log units higher ($\log K^* = -3.30$ at 1586 °C),
 614 suggesting a compositional control on $\gamma_{NaO_{0.5}}$ (cf. O'Neill 2005; Borisov 2009; Mathieu et al. 2011).

615
 616 The experiments of Kreutzberger et al. (1986) were performed on a $Di_{75}An_{25}$ melt. The volatility
 617 behaviour of Na, K and Rb is fit as a function of time (Fig. 11b) using an $n = 1$ reaction. A uniform
 618 sample radius of 0.0015 m and density of 2750 kg/m³ was assumed. The order of volatility observed
 619 (Na < K < Rb) is in good agreement with this work, and the fitted $\log K^*$ s for Na (-4.15) and Rb (-
 620 3.04) overlap with our determination (-4.25±0.10 and -3.12±0.10, respectively, Table 3), while that of
 621 K is much higher (-3.26 compared to -3.95±0.06, Table 3).

622
 623 Norris and Wood (2017) performed vaporisation experiments on a trace element-doped MORB melt,
 624 stirred in an Ni crucible. The agreement in the order of volatility for elements common in both studies
 625 is reasonable. At $\log fO_2 = -10$ and 1300 °C, Norris and Wood (2017) show $Cr < Ga < Zn < Pb \approx Cu <$
 626 $Ag < Ge < Cd$ (Fig. 11c), compared with $Cr < Ga < Cu < Zn \approx Ge < Pb < Ag \approx Cd$ in this work.
 627 Given that not all variables (e.g., stirring rate, eccentricity) were kept constant between their
 628 experiments, element depletion factors in Norris and Wood (2017) were normalised to a second
 629 element, j , such that physical factors affecting element loss cancel, leaving:

$$\frac{\ln\left(\frac{X_i^t}{X_i^0}\right)}{\ln\left(\frac{X_j^t}{X_j^0}\right)} = \frac{K_i^*}{K_j^*} (fO_2)^{\frac{\Delta n_{j-i}}{4}} \sqrt{\frac{M_i}{M_j}} \quad (19)$$

630 Here, $j = Zn$, and hence depletion of an element $\left(\frac{X_i^t}{X_i^0}\right)$ by a single vaporisation reaction will be
 631 proportional to a constant multiplied by $(fO_2)^{\frac{\Delta n_{j-i}}{4}}$ (eq. 19). Relative to the Zn vaporisation reaction
 632 ($n=2$), $\Delta n_{Zn-Cu} = 1$ and best fits are found with $\frac{K_{Cu}^*}{K_{Zn}^*} = 10^3$; this compares with 10^1 from our work
 633 (Table 3). For Pb, due to the reducing conditions only $Pb(g)$ is considered, hence $\Delta n_{Zn-Pb} = 0$ and $\frac{K_{Pb}^*}{K_{Zn}^*}$
 634 ≈ 1.2 , in reasonable agreement with $\frac{K_{Pb}^*}{K_{Zn}^*} = 4$ determined herein (Table 3). Similarly, only $Ga(g)$
 635 should be stable below < FMQ (Electronic Annex E), thus $\Delta n_{Zn-Ga} = -1$. Satisfactory agreement is

636 found when $\frac{K_{Ga}^*}{K_{Zn}^*} = 10^{-3}$. For $\Delta n_{Zn-Ge} = 0$ as determined in this work, no constant value fits the gradual
 637 decline in $\frac{X_{Ge}^t}{X_{Ge}^0}$ with $\log fO_2$ observed, suggesting that Δn_{Zn-Ge} increases with decreasing fO_2 .
 638 Phenomenologically, this is consistent with increasing proportions of Ge^{2+} in the melt <IW,
 639 potentially explaining its more volatile behaviour in Norris and Wood (2017) than reported here.

640

641 5.0. Discussion

642

643 Our approach is to provide experimental constraints on element vaporisation from silicate melts under
 644 a set of known and controlled experimental conditions rather than to replicate any specific natural
 645 process. As such, use of the results to quantify vaporisation in natural samples is associated with
 646 numerous caveats. We assume the synthetic ferrobasalt is a good approximation of natural melts,
 647 however, activity coefficients can vary with composition (O'Neill and Eggins, 2002; Borisov, 2009;
 648 section 4.6.) meaning our results are only indicative for other basaltic melts. Moreover, the absence of
 649 major volatiles (H, C, N, S and the halogens) in our experiments prevents their complexation of
 650 metal-bearing gas species, which could otherwise modify element volatility (Schaefer et al., 2012;
 651 Fegley et al., 2016; Renggli et al., 2017). Nevertheless, even in volatile-laden volcanic gases, higher
 652 temperatures and lower pressures favour simple species (monatomic gases, oxides) with respect to
 653 associated molecules (*e.g.*, Churakov et al., 2000). At low pressures (≤ 1 bar), the major volatiles are
 654 either sparingly soluble in silicate melts (*e.g.*, Carroll and Webster 1995) and/or highly volatile,
 655 leaving O_2 as the major volatile species. Such conditions may be relevant to degassed planetesimals,
 656 with escape velocities too low to retain an atmosphere of light elements (*cf.* Hin et al. 2017), as well
 657 as volatile-poor chondrules (Fedkin and Grossman, 2013; Oulton et al., 2016), tektites (Chapman and
 658 Scheiber, 1969; Koeberl, 1986) and other 1 atm furnace experiments (Ertel et al., 1997). Experimental
 659 and thermodynamic studies show that, in a vacuum, silicate vaporisation sets the fO_2 of the vapour
 660 phase close to the FMQ buffer (De Maria et al., 1971; Visscher and Fegley, 2013; Costa et al., 2017),
 661 precisely the conditions covered by our experiments. We hereafter discuss our results in the context of
 662 evaporation of planetary bodies.

663

664 5.1. Equilibrium evaporation and evaporation temperatures

665 Experimentally-derived thermodynamic data (Table 5), permit calculation of evaporation
 666 temperatures. The partial pressure of an element i in the gas phase is related to its mole fraction
 667 (X_i^{vap}) and total pressure, P_T :

$$p_i = X_i^{vap} P_T. \quad (20)$$

668 Because the fraction of i in the gas (f_i^{vap}) and in the liquid, f_i^{liq} must sum to 1, and $f_i^{liq} = X_i^{liq}/X_0^{liq}$
 669 where X_0^{liq} is the original mole fraction of element i , it follows that:

$$p_i = (X_0^{liq} - X_i^{liq})P_T. \quad (21)$$

670 Substituting eq. (21) into eq. (5), combining it with eq. (17) and solving for the temperature (T_e) at
 671 which a fraction, f , of an element, i , has evaporated, gives, for congruent dissociative evaporation
 672 reactions (eq. 4):

$$T_{e,i}^f = \frac{-\Delta H_i^*}{\left(R \left(\frac{n}{4} \ln f O_2 + \ln P_T + \ln \frac{f_i^{vap}}{(1 - f_i^{vap})} \right) - \Delta S_i^* \right)}. \quad (22)$$

673 For more complicated evaporation stoichiometries $T_{e,i}^f$ is computed analytically. Although 50%
 674 condensation temperatures are calculated by convention, any fraction evaporated could be chosen.
 675 Here, because the temperatures of the experiments range between 1573 K and 1823 K, it is favourable
 676 to keep the eventual calculated T_e^f within this range to minimise extrapolation and therefore
 677 uncertainties. As such, 1% evaporation temperatures, T_e^1 , are calculated, at $\log f O_2$ s; -10 ($T_e^{1,-10}$), -5
 678 ($T_e^{1,-5}$) and in air, $T_e^{1,air}$ (Table 6).

679 Relative to nebular T_c^{50} (Lodders, 2003, Fig. 12a; Wood et al. 2019, Fig. 12b), the higher total
 680 pressures (1 bar) and oxygen fugacities at which $T_e^{1,-10}$ are calculated offsets them to higher
 681 temperatures (eq. 22; Fig. 12). These effects notwithstanding, the correlation between $T_e^{1,-10}$ and T_c^{50}
 682 for lithophile elements, (Cr), Mg, Li, Mn, (Ga), Na, K, Rb and Zn, is excellent ($r^2 = 0.93$ for Lodders,
 683 2003; $r^2 = 0.90$ for Wood et al. 2019). Siderophile and chalcophile elements tend to have relatively
 684 lower $T_e^{1,-10}$ than their lithophile counterparts at a given T_c^{50} (Fig. 12). This likely reflects their early
 685 condensation, under nebular conditions, into an Fe-alloy or sulfide phase. An exception is Pb, for
 686 which Lodders (2003) calculated T_c^{50} as 727 K by assuming ideal condensation into Fe metal
 687 whereas Wood et al. (2019), considering its low solubility in Fe as Pb^0 and in FeS as PbS, calculated
 688 495 K. As such, Pb sits below and above, respectively, the lithophile element trends in Fig. 12. This
 689 highlights not only the need for solubility data for trace elements in major nebula condensate phases
 690 to better constrain T_c^{50} , but also that element volatility is sensitive to the phases present (silicate melt
 691 in our experiments; solid FeS, silicates and metal in the solar nebula).

692 A volatility scale of elements evaporating from a ferrobasaltic liquid at 1 bar (Table 6) as a function
 693 of $f O_2$ is shown in Fig. 13. Lead has T_e^1 within liquidus temperatures of basaltic rocks (≈ 1573 K),
 694 even at oxidising conditions, suggesting Pb (and more volatile elements such as Tl and Cd) might be
 695 slightly volatile in subaerial eruptions (see also Norman et al. 2004; Johnson and Canil 2011;
 696 Vlastélic et al. 2013; Edmonds et al. 2018). Zinc and Ge show similar volatility over all $f O_2$ due to

697 their equivalent $n = 2$ vaporisation reactions, where deviations in Zn/Ge should signal metal
698 segregation, as Ge is more siderophile than Zn (*e.g.*, Siebert et al. 2011; Wood et al. 2014). Alkali
699 metal volatilities increase monotonically down Group I, with Na, K and Rb showing identical
700 vaporisation stoichiometries. Lithium is the least volatile of the alkalis, except under oxidising
701 conditions, and becomes more refractory than either Ni (<FMQ-2) or Co (<IW+1). Manganese also
702 becomes more volatile than Li at \approx IW-6, a prediction verified by the observation of slightly
703 decreasing Mn/Li with increasing volatile depletion in carbonaceous chondrites (Siebert et al., 2018)
704 and lower T_c calculated by Wood et al. (2019). Thus, Mn (and Fe and Mg) vaporises sparingly in
705 oxidising, post-nebular settings. The depletion of these elements by volatility is therefore a hallmark
706 of nebular depletion where fO_2 is sufficiently low to render them volatile (O'Neill and Palme, 2008).
707 Although Cr is relatively refractory at low fO_2 , it becomes more volatile with fO_2 , such that $T_{e,Cr}^1 =$
708 1785 K in air is lower than all elements studied except Pb. The same progression is observed for Mo
709 (and W), and hence ratios of the abundances of these Group VI elements to volatile metals with
710 opposite behaviour ($n > 0$) are able to constrain fO_2 during evaporation (see also Fegley and Palme
711 1985).

712 5.2. Origin of moderately volatile elements in the terrestrial planets

713 Element depletion factors relevant to planet-building processes after dispersal of the solar nebula are
714 conveniently expressed by normalising to the main lithophile element in rocky planets, Mg. These
715 depletion factors, defined as $\frac{X_i^t}{X_i^0} / \frac{X_{Mg}^t}{X_{Mg}^0}$, were calculated as a function of temperature (1373 K to 1973
716 K) and fO_2 (FMQ-4 to FMQ+4) at 1 bar, and plotted in Fig. 14.

717 Differences in molar mass play only a secondary role in controlling $\frac{X_i^t}{X_i^0}$ (eq. 19) because equilibrium
718 partial pressures of stable gas species of moderately volatile elements vary by orders of magnitude
719 among one another. This is manifest in the pronounced discrimination of MVE abundances in
720 evaporation residues at a given fO_2 and T . That is, the most volatile MVEs (*e.g.*, Pb and Ge), will be
721 quantitatively vaporised before evaporation of more refractory elements, including Fe and Mg, has
722 begun (Fig. 14). Evaporation therefore results in a near-binary distribution of elements in the residue;
723 those that are preserved and those that are vaporised, with the transition between them defining a
724 sharp 'cut-off' temperature. While this cut-off temperature will vary with total pressure and fO_2 (eq.
725 22), the general step-function form of the MVE pattern in the residuum is insensitive to these
726 variables, or indeed to the accuracy of the K^* values. The binary element distribution results from
727 *relative* differences in partial pressures among MVEs, making it a diagnostic feature of single-stage
728 evaporation.

729 Urey (1952, 1954) first proposed that volatile element abundances could be used as
730 ‘cosmothermometers’ to track accretion temperatures of planetary materials, an approach rendered
731 quantitative by the calculation of condensation temperatures (Larimer, 1967). The fact that MVEs are
732 easily decoupled during evaporation was recognised, and employed as an argument by Anders (1964)
733 and further developed by Keays et al. (1971), Laul et al. (1973), Larimer (1973) and Grossman and
734 Larimer (1974) to exclude vaporisation as a major contributor to the gradual depletion of MVE with
735 volatility observed in chondrites as there is “*no one temperature at which they will all be condensed*
736 *to the same fractional degree*”. As in chondrites, the abundances of lithophile MVEs in the BSE
737 decline smoothly as a function of volatility (Fig. 14).

738 Volatile depletion in the Earth must reflect both *i*) the fraction of the element in the atmosphere (Fig.
739 14) and, unlike chondrites, *ii*) its proclivity to escape. Atmospheric escape from Earth is, however,
740 ineffective in fractionating MVEs abundances. Thermally-based Jeans escape requires prohibitively
741 high temperatures (>10000 K) due to the Earth’s high escape velocity (11.2 km/s) and would produce
742 a correlation with $M^{-0.5}$, which is not observed (Sossi and Fegley, 2018). Both hydrodynamic escape
743 (Hunten et al., 1987; Genda and Abe, 2003; Young et al. 2019) and outflow of ionised particles
744 (Yamauchi and Wahlund, 2007) are nearly mass-independent processes, meaning MVE losses should
745 reflect their equilibrium partial pressures (*cf.* Fig. 14).

746 Many MVE ratios in the Earth are chondritic (*e.g.*, O’Neill and Palme, 2008; Mann et al., 2009;
747 Siebert et al., 2018) suggesting minimal post-nebular perturbation by evaporative processes. Unlike
748 elemental ratios, isotope ratios are readily mass-fractionated during Langmuir evaporation (Humayun
749 and Clayton, 1995; Yu et al., 2003; Wombacher et al., 2004; Richter et al., 2007). Hence, the
750 agreement in MVE stable isotope compositions between Earth and carbonaceous chondrites (*e.g.*
751 Wombacher et al. 2008; Pringle et al., 2017; Sossi et al., 2018) also suggests terrestrial volatile
752 depletion occurred in a similar manner to that in chondrites. Contrastingly, the higher abundance of In
753 ($T_c^{50} \approx 530$ K) relative to Cd ($T_c^{50} \approx 500 - 650$ K) and Zn ($T_c^{50} \approx 700$ K) in the BSE despite its higher
754 siderophilicity and volatility permits deviation from canonical nebular conditions during volatile loss
755 (Wang et al., 2016; Norris and Wood, 2017), though other explanations, including collisional erosion,
756 are feasible (Witt-Eickschen et al. 2009). Indeed, the condensation/vaporisation behaviour of these
757 highly volatile elements ($T_c^{50} < 750$ K), whose abundances flatten out with T_c^{50} in carbonaceous
758 chondrites (Wolf et al., 1980; Humayun and Cassen, 2000; Braukmüller et al., 2018), is poorly
759 understood. Whether these elements also define a constant-abundance plateau in the BSE requires
760 additional work to distinguish between the relative effects of core formation and volatility (*cf.* Wang
761 et al., 2016; Ballhaus et al., 2017). For the MVEs, their gradual depletion with volatility in Earth’s
762 mantle, coupled with their chondritic elemental and isotope ratios, appear at-odds with partial
763 evaporation and loss at a single temperature and fO_2 such as may be expected during a giant impact
764 (Fig. 14).

765 A potential mechanism that could satisfy both isotopic and elemental constraints is the accretion of
766 the Earth from a distribution of partially vaporised bodies. In each body, the elements below a given
767 cut-off temperature are lost entirely while those above it are not lost at all (normalised abundances are
768 '1' above and '0' below), where the cut-off point varies stochastically from body to body. Integration
769 of material from many such bodies, each with its own binary pattern, would sum to a smooth pattern
770 in which MVE depletion correlates with volatility, but whose MVE isotopic composition is dominated
771 by the contributions from material that has seen negligible volatilisation.

772 By contrast, smaller bodies such as Vesta, the Ureilite and Angrite parent bodies and the Moon record
773 significant depletions, $<10^{-3} \times \text{CI}$, in highly volatile elements (Cd, Ag, Pb, Ge, Zn) coupled with
774 modest losses ($\approx 10^{-1}$ to $10^{-2} \times \text{CI}$) of the moderately volatile elements, such as Na, K and Ga (Janssens
775 et al., 1987; O'Neill, 1991; Ruzicka et al., 2001) and a lack of depletion in elements more refractory
776 than Li (see also Magna et al. 2006). Volatile element abundances in the Moon exemplify a highly
777 fractionated, binary pattern consistent with single-stage evaporation, where Mg-normalised
778 abundances of Ge, Zn, and the alkalis are very low (Wolf and Anders, 1980), whereas Li and Mn are
779 undepleted relative to Earth's mantle (Fig. 14). Furthermore, these bodies do exhibit fractionated
780 stable isotope signatures in elements such as Zn (*e.g.* Paniello et al. 2012), K (Wang and Jacobsen,
781 2016), Ga (Kato and Moynier, 2017) and Cl (Boyce et al., 2018); but not Li (Magna et al. 2006),
782 consistent with its retention during volatility-related processes. These lines of evidence are more
783 compatible with a partial evaporation origin, the conditions and mechanisms of which will require
784 quantitative assessment of temperatures, gas compositions, accretion scenarios and vapour loss
785 processes.

786 **Conclusion**

787 In order to determine the behaviour of moderately volatile elements during evaporation of silicate
788 melts, experiments were conducted in 1-atm vertical tube gas-mixing furnaces in which samples of
789 synthetic ferrobalt in the FCMAS system, doped with 1000 ppm each of Li, Na, K, Cu, Rb, Ga, Ge,
790 Pb, Mn, Mo, Zn, V, Zr, Sc, Ti, La, Gd, Yb, Ag and Cd, were suspended on noble metal wire loops and
791 heated to 1300 °C, 1400 °C, 1500 °C and 1550 °C for between 15 and 930 minutes at $\log f_{\text{O}_2}$ s between
792 air (-0.68) and -10. Element loss from the melt, as determined from LA-ICP-MS measurements of the
793 quenched glasses, varied strongly with f_{O_2} . Alloying with the metal wire and incomplete diffusion of
794 the element to the surface were unimportant, leaving vaporisation as the sole cause of the observed
795 depletion relative to the starting composition.

796 The degree of elemental loss depends on the stoichiometries of the vaporisation reaction(s), which
797 have the general form $\text{M}^{x+n}\text{O}_{(x+n)/2}(\text{l}) = \text{M}^x\text{O}_{x/2}(\text{g}) + n/4\text{O}_2$. These reactions are solved for the
798 equilibrium partial pressure of the gas species and incorporated into the Hertz-Knudsen-Langmuir
799 equation, enabling element evaporation from a sphere to be quantitatively modelled. Stoichiometries

800 of the reaction(s), n , and equilibrium constant(s), K^* are calculated from fits to the experimental data.
801 Most MVEs evaporate with $n > 0$, where stoichiometries of 1 (Cu, Na, K, Rb, Ag) and 2 (Zn, Ge, Cd)
802 are common. The Group VI metals, Cr and Mo, show the inverse behaviour ($n < 0$) by virtue of their
803 stable oxide-bearing gas species with oxidation states higher than those in the silicate liquid. The K^*
804 value is the product of the activity coefficient, γ_i , the evaporation coefficient, α_e and the equilibrium
805 constant of reaction (K), the first two of which are not known *a priori*. Evaporation coefficients
806 calculated using literature values for activity coefficients return values near unity, verifying the
807 accuracy of the approach and suggesting evaporation is near-ideal. Given α_e of 1, γ_i of melt oxide
808 components vary by $\sim 10^5$, shifting their volatilities compared with evaporation from pure oxides. For
809 all volatile elements, $\log K^*$ increases with temperature, which, when converted to ΔG^* , allows a
810 straight line to be fit to the data, where the slope is equal to $-\Delta S^*$ and the intercept ΔH^* .

811 These fundamental data are useful for understanding vapour loss during chondrule melting, degassing
812 of anhydrous magmas, tektite formation and other 1 atm furnace experiments. Although lithophile
813 elements show good agreement with nebular condensation temperatures at low fO_2 , chalcophile and
814 siderophile elements are generally more volatile during evaporation of silicate melts relative to solar
815 nebular environments. Evaporation of a silicate melt at a single temperature and fO_2 results in a near-
816 binary element distribution in the residuum, strongly discriminating the volatile elements from the
817 non-volatile. This type of fractionation among MVEs is observed in small telluric bodies (Moon,
818 Vesta) but not on Earth, where element depletion is a gradual function of volatility. This observation
819 argues against volatile loss from Earth during a giant impact, suggesting that it accreted from already
820 volatile-depleted components.

821 Acknowledgements

822 P.A.S. and F.M. were supported by the European Research Council under the H2020 scheme with the grant
823 #637503 (PRISTINE). We are grateful to the Associate Editor Munir Humayun for his measured, thorough and
824 insightful evaluation, advice for re-organisation of the manuscript and broad understanding of the
825 cosmochemical literature and to Executive Editors Marc Norman and Jeff Catalano. We thank Bernie Wood for
826 his input into the use of the HKL equation, experimental considerations, the importance of the evaporation
827 coefficient, and for recommending us to be more circumspect about our thermodynamic treatment, Gokce
828 Ustunisik on the experimental methodology and its relevance to natural processes and an anonymous reviewer
829 for various aspects of the work and for encouraging application of the model to other studies. P.A.S. is thankful
830 to Raúl Fonseca who shared experimental know-how and advice on evaporation experiments, to Bruce Fegley
831 and Katharina Lodders for their keen interest in the experiments, equilibrium evaporation and in-depth
832 calculation of partial pressures using their own codes, and to Frank Richter for highlighting the importance of
833 diffusive effects in the gas during experimental runs. Julien Siebert, Arno Rohrbach, Tahar Hammouda, Bernard
834 Bourdon and Nate Jacobson are thanked for many illuminating discussions.

835 **References**

- 836 Ackermann R. J., Thorn R. J. and Winslow G. H. (1962) *Some fundamental aspects of vaporization*,
837 AEC Research and Development Report, Argonne National Laboratory, Illinois.
- 838 Albarède F., Albalat E. and Lee C.-T. A. (2015) An intrinsic volatility scale relevant to the Earth and
839 Moon and the status of water in the Moon. *Meteorit. Planet. Sci.* **50**, 568–577.
- 840 Alexander C. M. O. D. (2001) Exploration of quantitative kinetic models for the evaporation of
841 silicate melts in vacuum and in hydrogen. *Meteorit. Planet. Sci.* **36**, 255–283.
- 842 Alexander C. M. O. D. (2002) Application of MELTS to kinetic evaporation models of FeO-bearing
843 silicate melts. *Meteorit. Planet. Sci.* **37**, 245–256.
- 844 Anders E. (1964) Origin, age, and composition of meteorites. *Space Sci. Rev.* **3**, 583–714.
- 845 Ballhaus C., Fonseca R. O. C., Münker C., Rohrbach A., Nagel T., Speelmanns I. M., Helmy H. M.,
846 Zirner A., Vogel A. K. and Heuser A. (2017) The great sulfur depletion of Earth's mantle is not
847 a signature of mantle–core equilibration. *Contrib. to Mineral. Petrol.* **172**.
- 848 Bart G., Ikramuddin M. and Lipschutz M. E. (1980) Thermal metamorphism of primitive meteorites-
849 IX. On the mechanism of trace element loss from Allende heated up to 1400° C. *Geochim.*
850 *Cosmochim. Acta* **44**, 719–730.
- 851 Berry A. J. and O'Neill H. S. C. (2004) A XANES determination of the oxidation state of chromium
852 in silicate glasses. *Am. Mineral.* **89**, 790–798.
- 853 Blanchard I., Badro J., Siebert J. (2015) Composition of the core from gallium metal–silicate
854 partitioning experiments. *Earth Planet. Sci. Lett.* **427**, 191–201.
- 855 Boltzmann L. (1872) Weitere Studien über das Wärmegleichgewicht unter Gasmolekülen. *Sitz.-Ber.*
856 *Akad. Vienna* **2**, 275–370.
- 857 Bonsor A., Leinhardt Z. M., Carter P. J., Elliott T., Walter M. J. and Stewart S. T. (2015) A collisional
858 origin to Earth's non-chondritic composition. *Icarus*, **247**, 291–300.
- 859 Borisov A. A. (2009) Influence of SiO₂ and Al₂O₃ on the activity coefficients of alkalis in melts: An
860 experimental study. *Petrology* **17**, 579–590.
- 861 Bottinga Y. and Weill, D. F. (1970) Densities of liquid silicate systems calculated from partial molar
862 volumes of oxide components. *Am. J. Sci.*, **269**, 169–182.
- 863 Boyce J. W., Kanee S. A., McCubbin F. M., Barnes J. J., Bricker H. and Treiman A. H. (2018) Early
864 loss, fractionation, and redistribution of chlorine in the Moon as revealed by the low-Ti lunar
865 mare basalt suite. *Earth Planet. Sci. Lett.* **500**, 205–214.
- 866 Braukmüller N., Wombacher F., Hezel D. C., Escoube R. and Münker C. (2018) The chemical
867 composition of carbonaceous chondrites: Implications for volatile element depletion,
868 complementarity and alteration. *Geochim. Cosmochim. Acta* **239**, 17–48.
- 869 Burns R. P. (1966) Systematics of the evaporation coefficient Al₂O₃, Ga₂O₃, In₂O₃. *J. Chem. Phys.* **44**,
870 3307–3319.
- 871 Canup R. M., Visscher C., Salmon J. and Fegley Jr B. (2015) Lunar Volatile Depletion Due To
872 Incomplete Accretion Within An Impact-Generated Disk. *Nat. Geosci.* **8**, 1–6.
- 873 Carroll M. R. and Webster J. D. (1995) Solubilities of sulfur, noble gases, nitrogen, chlorine, and
874 fluorine in magmas. In *Reviews in Mineralogy vol. 30: Volatiles in Magmas* (eds. M. R. Carroll
875 and J. R. Holloway). Mineralogical Society of America. pp. 231–279.
- 876 Carter P. J., Leinhardt Z. M., Elliott T., Walter M. J. and Stewart S. T. (2015) Compositional
877 evolution during rocky protoplanet accretion. *Astrophys. J.*, **813**, 72.
- 878 Chamberlain J. W. and Hunten D. M. (1989) *Theory of Planetary Atmospheres*, 2nd Ed. Academic
879 Press, San Diego.
- 880 Chapman D. R. and Scheiber L. C. (1969) Chemical Investigation of Australasian Tektites. *J.*
881 *Geophys. Res.* **74**, 6737–6776.
- 882 Chapman S. and Cowling T. G. (1970) *The Mathematical Theory of Non-Uniform Gases*. 3rd ed.,
883 Cambridge University Press, Cambridge.
- 884 Charles R. J. (1967) Activities in Li₂O-, Na₂O-, and K₂O-SiO₂ Solutions. *J. Am. Ceram. Soc.* **50**, 631–
885 641.
- 886 Chase M. W. (1998) NIST-JANAF Thermochemical Tables, 4th Ed. *J. Phys. Chem. Ref. Data*
887 *Monograph 9, Parts I & II*.
- 888 Churakov S. V., Tkachenko S. I., Korzhinskii M. A., Botcharnikov R. E. and Schmulovich K. I.
889 (2000) Evolution of composition of high temperature fumarolic gasses from Kudryavy volcano,

890 Iturup, Kuril Islands: the thermodynamic modeling. *Geochemistry Int.* **38**, 436–451.

891 Costa G. C. C., Jacobson N. S. and Fegley B. (2017) Vaporization and thermodynamics of forsterite-
892 rich olivine and some implications for silicate atmospheres of hot rocky exoplanets. *Icarus* **289**,
893 42–55.

894 De Maria G., Balducci G., Guido M. and Piacente V. (1971) Mass spectrometric investigation of the
895 vaporization process of Apollo 12 lunar samples. *Proc. Second Lunar Sci. Conf.* **2**, 1367–1380.

896 Donaldson C. H. (1979) Composition changes in a basalt melt contained in a wire loop of Pt₈₀Rh₂₀:
897 effects of temperature, time, and oxygen fugacity. *Mineral. Mag.* **43**, 115–119.

898 Drowart J., Chatillon C., Hastie J. and Bonnell D. (2005) High-temperature mass spectrometry:
899 Instrumental techniques, ionization cross-sections, pressure measurements, and thermodynamic
900 data (IUPAC Technical Report). *Pure Appl. Chem.* **77**, 683–737.

901 Drowart J. and Goldfinger P. (1967) Investigation of Inorganic Systems at High Temperature by Mass
902 Spectrometry. *Angew. Chemie Int. Ed.* **6**, 581–648.

903 Ebel D. S. (2004) Condensation of Rocky Material in Astrophysical Environments. In *Meteorites and
904 the Early Solar System II* (eds. D. S. Lauretta and H. Y. McSween). University of Arizona Press,
905 Tucson. pp. 253–277.

906 Ebel D. S. and Grossman L. (2000) Condensation in dust-enriched systems. *Geochemica Cosmochem.
907 Acta* **64**, 339–366.

908 Edmonds M., Mather T. A. and Liu E. J. (2018) A distinct metal fingerprint in arc volcanic emissions.
909 *Nature Geo.* **11**, 790–794.

910 Ertel W., Dingwell D. B. and O’Neill H. S. C. (1997) Compositional dependence of the activity of
911 nickel in silicate melts. *Geochim. Cosmochim. Acta* **61**, 4707–4721.

912 Exner O. (1973) The Enthalpy-Entropy Relationship. In *Progress in Physical Organic Chemistry,
913 Volume 10* (eds. A. Streitwieser and R. W. Taft). John Wiley & Sons, Inc., Hoboken, NJ, USA.
914 pp. 411–482.

915 Fedkin A. V. and Grossman L. (2013) Vapor saturation of sodium: Key to unlocking the origin of
916 chondrules. *Geochim. Cosmochim. Acta* **112**, 226–250.

917 Fedkin A. V., Grossman L. and Ghiorso M. S. (2006) Vapor pressures and evaporation coefficients
918 for melts of ferromagnesian chondrule-like compositions. *Geochim. Cosmochim. Acta* **70**, 206–
919 223.

920 Fegley B., Jacobson N. S., Williams K. B., Plane J. M. C., Schaefer L. and Lodders K. (2016)
921 Solubility of Rock in Steam Atmospheres of Planets. *Astrophys. J.* **824**, 103.

922 Fegley B. and Palme H. (1985) Evidence for oxidizing conditions in the solar nebula from Mo and W
923 depletions in refractory inclusions in carbonaceous chondrites. *Earth Planet. Sci. Lett.* **72**, 311–
924 326.

925 Fraser D. G. and Rammensee W. (1987) Determination of the mixing properties of granitic and other
926 alumino silicate melts by Knudsen Cell Mass Spectrometry. In *Magmatic Processes:
927 Physicochemical Principles* (ed. B. O. Mysen), The Geochemical Society Special Publication **1**,
928 Washington D.C. pp. 401–410.

929 Genda H. and Abe Y. (2003) Modification of a proto-lunar disk by hydrodynamic escape of silicate
930 vapor. *Earth Planets Sp.* **53**, 53–57.

931 Georges P., Libourel G. and Deloule E. (2000) Experimental constraints on alkali condensation in
932 chondrule formation. *Meteorit. Planet. Sci.* **35**, 1183–1188.

933 Gibson E. K. and Hubbard N. J. (1972) Thermal volatilization studies on lunar samples. *Proc. Third
934 Lunar Sci. Conf.* **2**, 2003–2014.

935 Glushko V. P., Medvedev V. A., Gurvich L. V. and Yungman V. S. (1999) *Thermal Constants of
936 Substances*. 1st ed., John Wiley & Sons, New York.

937 Gooding J. L. and Muenow D. W. (1976) Activated release of alkalis during the vesiculation of
938 molten basalts under high vacuum: implications for lunar volcanism. *Geochim. Cosmochim.
939 Acta* **40**, 675–686.

940 Grant K. and Wood B. J. (2008) Alkali activities in silicate melts. *Geochim. Cosmochim. Acta*, A323.

941 Grossman L. (1972) Condensation in the primitive solar nebula. *Geochim. Cosmochim. Acta* **36**, 597–
942 619.

943 Grossman L. and Larimer J. W. (1974) Early chemical history of the solar system. *Rev. Geophys.* **12**,
944 71–101.

- 945 Hastie J. W., Plante E. R., Bonnell and D. W. (1982) Alkali Vapor Transport in Coal Conversion and
 946 Combustion Systems. In: *Metal Bonding and Interactions in High Temperature Systems* (eds. J.
 947 L. Gole and W. C. Stwalley W. C.), ACS Symposium Series **179**, Washington D.C., pp. 543–
 948 600.
- 949 Hertz H. (1882) Ueber den Druck des gesättigten Quecksilberdampfes. *Ann. der Phys. und Chemie*
 950 **17**, 177–197.
- 951 Hin R. C., Coath C. D., Carter P. J., Nimmo F., Lai Y.-J., Pogge von Strandmann P. A. E., Willbold
 952 M., Leinhardt Z. M., Walter M. J. and Elliott T. (2017) Magnesium isotope evidence that
 953 accretional vapour loss shapes planetary compositions. *Nature* **549**, 511–515.
- 954 Hirth J. P. and Pound G. M. (1963) *Condensation and evaporation—nucleation and growth kinetics*,
 955 Pergamon Press, Oxford.
- 956 Holzheid A., Borisov A. and Palme H. (1994) The effect of oxygen fugacity and temperature on
 957 solubilities of nickel, cobalt, and molybdenum in silicate melts. *Geochim. Cosmochim. Acta* **58**,
 958 1975–1981.
- 959 Holzheid A. and Lodders K. (2001) Solubility of copper in silicate melts as function of oxygen and
 960 sulfur fugacities, temperature, and silicate composition. *Geochim. Cosmochim. Acta* **65**, 1933–
 961 1951.
- 962 Holzheid A., Palme H. and Chakraborty S. (1997) The activities of NiO, CoO and FeO in silicate
 963 melts. *Chem. Geol.* **139**, 21–38.
- 964 Humayun M. and Cassen P. (2000) Processes Determining the Volatile Abundances of the Meteorites
 965 and Terrestrial Planets. In *The Origin of the Earth and Moon* (eds. R. M. Canup and K. Righter).
 966 University of Arizona Press, Tucson. pp. 3–23.
- 967 Humayun M. and Clayton R. N. (1995) Potassium isotope cosmochemistry: Genetic implications of
 968 volatile element depletion. *Geochim. Cosmochim. Acta* **59**, 2131–2148.
- 969 Humayun M. and Koeberl C. (2004) Potassium isotopic composition of Australasian tektites.
 970 *Meteorit. Planet. Sci.* **39**, 1509–1516.
- 971 Hunten D. M., Pepin R. O. and Walker J. C. G. (1987) Mass fractionation in hydrodynamic escape.
 972 *Icarus* **69**, 532–549.
- 973 Janssens M.-J., Hertogen J., Wolf R., Ebihara M. and Anders E. (1987) Ureilites: Trace element clues
 974 to their origin. *Geochim. Cosmochim. Acta* **51**, 2275–2283.
- 975 Jochum K.P., Stoll B., Weis U., Jacob D. E., Mertz-Kraus R. and Andreae M. O. (2014). Non-Matrix-
 976 Matched Calibration for the Multi-Element Analysis of Geological and Environmental Samples
 977 Using 200 nm Femtosecond LA-ICP-MS: A Comparison with Nanosecond Lasers. *Geochem.*
 978 *Geoanal. Res.* **38**(3), 265–292.
- 979 Johnson A. and Canil D. (2011) The degassing behavior of Au, Tl, As, Pb, Re, Cd and Bi from
 980 silicate liquids: Experiments and applications. *Geochim. Cosmochim. Acta* **75**, 1773–1784.
- 981 Kato C. and Moynier F. (2017) Gallium isotopic evidence for extensive volatile loss from the Moon
 982 during its formation. *Sci. Adv.* **3**, e1700571.
- 983 Keays R. R., Ganapathy R. and Anders E. (1971) Chemical fractionations in meteorites-IV
 984 Abundances of fourteen trace elements in L-chondrites; implications for cosmochemistry.
 985 *Geochim. Cosmochim. Acta* **35**, 337–363.
- 986 Kemeny G. and Rosenberg B. (1973) Compensation law in thermodynamics and thermal death.
 987 *Nature* **243**, 400–401.
- 988 Kimura H., Asano M. and Kubo K. (1980) Thermochemical study of the vaporization of Li₂O(c) by
 989 mass spectrometric Knudsen effusion method. *J. Nucl. Mater.* **92**, 221–228.
- 990 Klemme S. and O'Neill H. S. C. (2000) The effect of Cr on the solubility of Al in orthopyroxene:
 991 experiments and thermodynamic modelling. *Contrib. to Mineral. Petrol.* **140**, 84–98.
- 992 Knacke O. and Stranski I. N. (1956) The mechanism of evaporation. *Prog. Met. Phys.* **6**, 181–235.
- 993 Knudsen M. (1909) Die Gesetze der Molekularströmung und der inneren Reibungsströmung der Gase
 994 durch Röhren. *Ann. Phys.* **333**, 75–130.
- 995 Kobertz D., Müller M. and Molak A. (2014) Vaporization and caloric studies on lead titanate.
 996 *Calphad Comput. Coupling Phase Diagrams Thermochem.* **46**, 62–79.
- 997 Kobertz D. (2019a) Vaporization and caloric studies on yellow lead oxide. *Calphad* **65**, 155–164.
- 998 Kobertz D. (2019b) Vaporization studies on sodium oxide. *Calphad* **64**, 327–333.
- 999 Koeberl C. (1986) Geochemistry of tektites and impact glasses. *Annu. Rev. Earth Planet. Sci.* **14**,

- 1000 323–350.
- 1001 Kreutzberger M. E., Drake M. J. and Jones J. H. (1986) Origin of the Earth's Moon: Constraints from
1002 alkali volatile trace elements. *Geochim. Cosmochim. Acta* **50**, 91–98.
- 1003 L'vov B. (2007) *Thermal Decomposition of Solids and Melts*. 1st ed. Springer Netherlands.
- 1004 Lamoreaux R. H. and Hildenbrand D. L. (1984) High Temperature Vaporization of Oxides. I. Alkali
1005 Metal Binary Oxides. *J. Phys. Chem. Ref. Data* **13**, 151–173.
- 1006 Lamoreaux R. H., Hildenbrand D. L. and Brewer L. (1987) High-Temperature Vaporization Behavior
1007 of Oxides II. Oxides of Be, Mg, Ca, Sr, Ba, B, Al, Ga, In, Tl, Si, Ge, Sn, Pb, Zn, Cd, and Hg. *J.*
1008 *Phys. Chem. Ref. Data* **16**, 419–443.
- 1009 Langmuir I. (1916) The evaporation, condensation and reflection of molecules and the mechanism of
1010 adsorption. *Phys. Rev.* **8**, 149–176.
- 1011 Larimer J. W. (1967) Chemical fractionations in meteorites-I. Condensation of the elements.
1012 *Geochim. Cosmochim. Acta* **31**, 1215–1238.
- 1013 Larimer J. W. (1973) Chemical fractionations in meteorites-VII. Cosmothemometry and
1014 cosmobarometry. *Geochim. Cosmochim. Acta* **37**, 1603–1623.
- 1015 Laul J. C., Ganapathy R., Anders E. and Morgan J. W. (1973) Chemical fractionations in meteorites-
1016 VI. Accretion temperatures of H-, LL- and E-chondrites, from abundance of volatile trace
1017 elements. *Geochim. Cosmochim. Acta* **37**, 329–357.
- 1018 Li Z., Hu Z., Liu Y., Gao S., Li M., Zong K., Chen H. and Hu S. (2015) Accurate determination of
1019 elements in silicate glass by nanosecond and femtosecond laser ablation ICP-MS at high spatial
1020 resolution. *Chem. Geol.* **400**, 11–23.
- 1021 Littlewood R. and Rideal E. (1956) On the Evaporation Coefficient. *Trans. Faraday Soc.* **52**, 1598–
1022 1608.
- 1023 Liu Y., Zhang L. and Yu D. (2009) Diffusion mobilities in fcc Cu-Au and fcc Cu-Pt alloys. *J. Phase*
1024 *Equilibria Diffus.* **30**, 136–145.
- 1025 Lodders K. (2003) Solar System Abundances and Condensation Temperatures of the Elements.
1026 *Astrophys. J.* **591**, 1220–1247.
- 1027 Magna T., Wiechert U. and Halliday A. N. (2006) New constraints on the lithium isotope
1028 compositions of the Moon and terrestrial planets. *Earth Planet. Sci. Lett.* **243**, 336–353.
- 1029 Mann U., Frost D. J. and Rubie D. C. (2009) Evidence for high-pressure core-mantle differentiation
1030 from the metal–silicate partitioning of lithophile and weakly-siderophile elements. *Geochim.*
1031 *Cosmochim. Acta* **73**, 7360–7386.
- 1032 Mare E., O'Neill H. S. C. and Berry A. (2016) Changes in the Coordination and Valence State of Ge
1033 in Silicate Melts at Conditions Relevant to Core Formation. In *Mineralogical Magazine*
1034 Yokohama, Japan. p. 1971.
- 1035 Margrave J. L. (1967) *The Characterization of High Temperature Vapors*, John Wiley & Sons, New
1036 York.
- 1037 Markova O. M., Yakovlev O. I., Semenov G. A. and Belov A. N. (1986) Evaporation of Natural Melts
1038 in a Knudsen Chamber. *Geokhimiya* **11**, 1559–1568.
- 1039 Mather T. A., Witt M. L. I., Pyle D. M., Quayle B. M., Aiuppa A., Bagnato E., Martin R. S., Sims K.
1040 W. W., Edmonds M., Sutton A. J. and Ilyinskaya E. (2012) Halogens and trace metal emissions
1041 from the ongoing 2008 summit eruption of Kīlauea volcano, Hawai'i. *Geochim. Cosmochim.*
1042 *Acta* **83**, 292–323.
- 1043 Mathieu R., Khedim H., Libourel G., Podor R., Tissandier L., Deloule E., Faure F., Rapin C. and
1044 Vilasi M. (2008) Control of alkali-metal oxide activity in molten silicates. *J. Non. Cryst. Solids*
1045 **354**, 5079–5083.
- 1046 Mathieu R., Libourel G., Deloule E., Tissandier L., Rapin C. and Podor R. (2011) Na₂O solubility in
1047 CaO-MgO-SiO₂ melts. *Geochim. Cosmochim. Acta* **75**, 608–628.
- 1048 Maxwell J. C. (1860) Illustrations of the dynamical theory of gases.—Part I. On the motions and
1049 collisions of perfectly elastic spheres. *London, Edinburgh, Dublin Philos. Mag. J. Sci.* **19**, 19–
1050 32.
- 1051 Melosh H. J. (1990) Giant Impacts and the Thermal State of the Early Earth. In *Origin of the Earth*
1052 (eds. H. E. Newsom and J. H. Jones). Oxford University Press, New York. pp. 69–83.
- 1053 Morbidelli A., Lunine J. I., O'Brien D. P., Raymond S. N. and Walsh K. J. (2012) Building Terrestrial
1054 Planets. *Annu. Rev. Earth Planet. Sci.* **40**, 251–275.

- 1055 Moynier F., Beck P., Jourdan F., Yin Q. Z., Reimold U. and Koeberl C. (2009) Isotopic fractionation
 1056 of zinc in tektites. *Earth Planet. Sci. Lett.* **277**, 482–489.
- 1057 Nakajima M. and Stevenson D. J. (2014) Investigation of the initial state of the Moon-forming disk:
 1058 Bridging SPH simulations and hydrostatic models. *Icarus* **233**, 259–267.
- 1059 Naughton J. J., Derby J. V. and Lewis V. A. (1971) Vaporization from heated lunar samples and the
 1060 investigation of lunar erosion by volatilized alkalis. *Proc. Second Lunar Sci. Conf.* **1**, 449–457.
- 1061 Ni P., Zhang Y., Chen S. and Gagnon J. (2019) A melt inclusion study on volatile abundances in the
 1062 lunar mantle. *Geochim. Cosmochim. Acta* **249**, 17–41.
- 1063 Norman M. D., Garcia M. O. and Bennett V. C. (2004) Rhenium and chalcophile elements in basaltic
 1064 glasses from Ko’olau and Moloka’i volcanoes: Magmatic outgassing and composition of the
 1065 Hawaiian plume. *Geochim. Cosmochim. Acta* **68**, 3761–3777.
- 1066 Norris C. A. and Wood B. J. (2017) Earth’s volatile contents established by melting and vaporization.
 1067 *Nature* **549**, 507–510.
- 1068 Notsu K., Onuma N. and Nishida N. (1978) High temperature heating of the Allende meteorite.
 1069 *Geochim. Cosmochim. Acta* **42**, 903–907.
- 1070 O’Neill H. S. C. (2005) A method for controlling alkali-metal oxide activities in one-atmosphere
 1071 experiments and its application to measuring the relative activity coefficients of NaO_{0.5} in
 1072 silicate melts. *Am. Mineral.* **90**, 497–501.
- 1073 O’Neill H. S. C. (1991) The origin of the Moon and the early history of the Earth - A chemical model.
 1074 Part 1: The Moon. *Geochim. Cosmochim. Acta* **55**, 1135–1157.
- 1075 O’Neill H. S. C. and Eggins S. M. (2002) The effect of melt composition on trace element
 1076 partitioning: an experimental investigation of the activity coefficients of FeO, NiO, CoO, MoO₂
 1077 and MoO₃ in silicate melts. *Chem. Geol.* **186**, 151–181.
- 1078 O’Neill H. S. C. and Palme H. (2008) Collisional erosion and the non-chondritic composition of the
 1079 terrestrial planets. *Philos. Trans. A. Math. Phys. Eng. Sci.* **366**, 4205–38.
- 1080 O’Neill H. S. C. and Palme H. (1998) Composition of the Silicate Earth: Implications for Accretion
 1081 and Core Formation. In *The Earth’s Mantle: Composition, Structure and Evolution* (ed. I.
 1082 Jackson). Cambridge University Press, Cambridge. pp. 3 – 126.
- 1083 O’Neill H. S. C. and Pownceby M. I. (1993) Thermodynamic data from redox reactions at high
 1084 temperatures. I. An experimental and theoretical assessment of the electrochemical method
 1085 using stabilized zirconia electrolytes, with revised values for the Fe–“FeO”, Co–CoO, Ni–NiO
 1086 and Cu–Cu₂O. *Contrib. to Mineral. Petrol.* **114**, 296–314.
- 1087 Ohta H. and Suito H. (1995) Activities of MnO in CaO-SiO₂-Al₂O₃-MnO (<10 Pct)-Fe¹O (<3 Pct)
 1088 Slags Saturated with Liquid Iron. *Metall. Mater. Trans. B* **26**, 295–303.
- 1089 Oulton J., Humayun M., Fedkin A. and Grossman L. (2016) Chemical evidence for differentiation ,
 1090 evaporation and recondensation from silicate clasts in Gujba. *Geochim. Cosmochim. Acta* **177**,
 1091 254–274.
- 1092 Pahlevan K., Stevenson D. J. and Eiler J. M. (2011) Chemical fractionation in the silicate vapor
 1093 atmosphere of the Earth. *Earth Planet. Sci. Lett.* **301**, 433–443.
- 1094 Palme H., Larimer J. W. and Lipschutz M. E. (1988) Moderately Volatile Elements. In *Meteorites and*
 1095 *the Early Solar System* (eds. J. F. Kerridge and M. S. Matthews). University of Arizona Press,
 1096 Tucson. pp. 436–461.
- 1097 Paniello R. C., Day J. M. D. and Moynier F. (2012) Zinc isotopic evidence for the origin of the Moon.
 1098 *Nature* **490**, 376–379.
- 1099 Persad A. H. and Ward C. A. (2016) Expressions for the Evaporation and Condensation Coefficients
 1100 in the Hertz-Knudsen Relation. *Chem. Rev.* **116**, 7727–7767.
- 1101 Pretorius E. B. and Muan (1992) Activity–Composition Relations of Chromium Oxide in Silicate
 1102 Melts at 1500 °C. *J. Am. Ceram. Soc.* **75**, 1364–1377.
- 1103 Pringle E. A., Moynier F., Beck P., Paniello R. and Hezel D. C. (2017) The origin of volatile element
 1104 depletion in early solar system material: Clues from Zn isotopes in chondrules. *Earth Planet.*
 1105 *Sci. Lett.* **468**, 62–71.
- 1106 Rammensee W. and Fraser D. G. (1982) Determination of activities in silicate melts by Knudsen cell
 1107 mass spectrometry-I. The system NaAlSi₃O₈-KAlSi₃O₈. *Geochim. Cosmochim. Acta* **46**, 2269–
 1108 2278.
- 1109 Renggli C. J., King P. L., Henley R. W. and Norman M. D. (2017) Volcanic gas composition, metal

- 1110 dispersion and deposition during explosive volcanic eruptions on the Moon. *Geochim.*
1111 *Cosmochim. Acta* **206**, 296–311.
- 1112 Reyes R. A. and Gaskell D. R. (1983) The thermodynamic activity of ZnO in silicate melts. *Metall.*
1113 *Trans. B* **14**, 725–731.
- 1114 Richter F. M., Davis A. M., Ebel D. S. and Hashimoto A. (2002) Elemental and isotopic fractionation
1115 of type B calcium-, aluminum-rich inclusions: Experiments, theoretical considerations, and
1116 constraints on their thermal evolution. *Geochim. Cosmochim. Acta* **66**, 521–540.
- 1117 Richter F. M., Janney P. E., Mendybaev R. A., Davis A. M. and Wadhwa M. (2007) Elemental and
1118 isotopic fractionation of Type B CAI-like liquids by evaporation. *Geochim. Cosmochim. Acta*
1119 **71**, 5544–5564.
- 1120 Ringwood A. E. (1966) Chemical evolution of the terrestrial planets. *Geochim. Cosmochim. Acta* **30**,
1121 41–104.
- 1122 Robie R. A. and Hemingway B. S. (1995) *Thermodynamic Properties of Minerals and Related*
1123 *Substances at 298.15 K and 1 Bar (10⁵ Pascals) Pressure and at Higher Temperatures*. USGS
1124 Bulletin 2131.
- 1125 Rubin A. E., Fegley B. and Brett R. (1988) Oxidation State in Chondrites. In *Meteorites and the Early*
1126 *Solar System* (eds. J. F. Kerridge and M. S. Matthews). University of Arizona Press, Tucson. pp.
1127 488–511.
- 1128 Ruzicka A., Snyder G. A. and Taylor L. A. (2001) Comparative geochemistry of basalts from the
1129 Moon, Earth, HED asteroid, and Mars: Implications for the origin of the Moon. *Geochim.*
1130 *Cosmochim. Acta* **65**, 979–997.
- 1131 Safarian J. and Engh T. A. (2013) Vacuum Evaporation of Pure Metals. *Metall. Mater. Trans. A* **44**,
1132 747–753.
- 1133 Sahijpal S., Soni P. and Gupta G. (2007) Numerical simulations of the differentiation of accreting
1134 planetesimals with ²⁶Al and ⁶⁰Fe as the heat sources. *Meteorit. Planet. Sci.* **42**, 1529–1548.
- 1135 Schaefer L. and Fegley B. (2010) Volatile element chemistry during metamorphism of ordinary
1136 chondritic material and some of its implications for the composition of asteroids. *Icarus* **205**,
1137 483–496.
- 1138 Schaefer L., Lodders K. and Fegley B. (2012) Vaporization of the earth: Application to exoplanet
1139 atmospheres. *Astrophys. J.* **755**, 41.
- 1140 Schreiber H. D. (1987) An Electrochemical Series of Redox Couples in Silicate Melts: A Review and
1141 Applications to Geochemistry. *J. Geophys. Res.* **92**, 9225–9232.
- 1142 Shimaoka T., Miyano N., Baba T., Yamamoto K. and Nakamura N. (1994) Volatilization of Alkali
1143 Metals from the Heated Murchison (CM2) Meteorite. *Proc. NIPR Symp. Antarct. Meteorites* **7**,
1144 164–177.
- 1145 Shimaoka T. and Nakamura (1991) The effect of total pressure on vaporization of alkalis from
1146 partially molten chondritic material. In *Origin and Evolution of Interplanetary Dust* (eds. A. C.
1147 Levasseur-Regourd and H. Hasegawa). Kluwer Academic Publishers, Japan. pp. 79–82.
- 1148 Shornikov S. I. (2015) Vaporization coefficients of oxides contained in the melts of Ca-Al-inclusions
1149 in chondrites. *Geochemistry Int.* **53**, 1080–1089.
- 1150 Siebert J., Corgne A. and Ryerson F. J. (2011) Systematics of metal–silicate partitioning for many
1151 siderophile elements applied to Earth’s core formation. *Geochim. Cosmochim. Acta* **75**, 1451–
1152 1489.
- 1153 Siebert J. and Shahar A. (2015) An Experimental Geochemistry Perspective on Earth’s Core
1154 Formation. In *The Early Earth: Accretion and Differentiation* (eds. J. Badro and M. J. Walter).
1155 American Geophysical Union, Washington, D. C. pp. 103–121.
- 1156 Siebert J., Sossi P. A., Blanchard I., Mahan B., Badro J. and Moynier F. (2018) Chondritic Mn/Na
1157 ratio and limited post-nebular volatile loss of the Earth. *Earth Planet. Sci. Lett.* **485**, 130–139.
- 1158 Sossi P. A. and Fegley B. (2018) Thermodynamics of Element Volatility and its Application to
1159 Planetary Processes. In *Reviews in Mineralogy and Geochemistry 84: High temperature gas-*
1160 *solid reactions in Earth and planetary processes* (eds. P. L. King, T. M. Seward, and B. Fegley).
1161 Mineralogical Society of America, Chantilly. pp. 393–459.
- 1162 Sossi P. A., Nebel O., O’Neill H. S. C. and Moynier F. (2018) Zinc isotope composition of the Earth
1163 and its behaviour during planetary accretion. *Chem. Geol.* **477**, 73–84.
- 1164 Symonds R. B. and Reed M. H. (1993) Calculation of Multicomponent chemical equilibria in gas-

- 1165 solid-liquid systems: Calculation methods, thermochemical data, and applications to studies of
 1166 high-temperature volcanic gases with examples from Mount St. Helens. *Am. J. Sci.* **293**, 758–
 1167 864.
- 1168 Tokor N. Y., Darken L. S. and Muan A. (1991) Equilibrium Phase Relations and Thermodynamics of
 1169 the Cr-O System in the Temperature Range of 1500 °C to 1825 °C. *Metall. Trans. B* **22B**, 225–
 1170 232.
- 1171 Tsuchiyama A., Nagahara H. and Kushiro I. (1981) Volatilization of sodium from silicate melt
 1172 spheres and its application to the formation of chondrules. *Geochim. Cosmochim. Acta* **45**,
 1173 1357–1367.
- 1174 Tuff J. and O'Neill H. S. C. (2010) The effect of sulfur on the partitioning of Ni and other first-row
 1175 transition elements between olivine and silicate melt. *Geochim. Cosmochim. Acta* **74**, 6180–
 1176 6205.
- 1177 Urey H. C. (1952) Chemical fractionation in the meteorites and the abundance of the elements.
 1178 *Geochim. Cosmochim. Acta* **2**, 269–282.
- 1179 Urey H. C. (1954) On the dissipation of gas and volatilized elements from protoplanets. *Astrophys. J.*
 1180 *Suppl. Ser.* **1**, 147–173.
- 1181 Visscher C. and Fegley B. (2013) Chemistry of Impact-Generated Silicate Melt-Vapor Debris Disks.
 1182 *Astrophys. J.* **767**, L12.
- 1183 Vlastélic I., Menard G., Gannoun A., Piro J. L., Staudacher T. and Famin V. (2013) Magma degassing
 1184 during the April 2007 collapse of Piton de la Fournaise: The record of semi-volatile trace
 1185 elements (Li, B, Cu, In, Sn, Cd, Re, Tl, Bi). *J. Volcanol. Geotherm. Res.* **254**, 97–107.
- 1186 Wang K. and Jacobsen S. B. (2016) Potassium Isotopic Evidence for the Origin of the Moon. *Nature*
 1187 **538**, 487–490.
- 1188 Wang Z., Laurenz V., Petitgirard S. and Becker H. (2016) Earth's moderately volatile element
 1189 composition may not be chondritic: Evidence from In, Cd and Zn. *Earth Planet. Sci. Lett.* **435**,
 1190 136–146.
- 1191 Wänke H. and Dreibus G. (1988) Chemical Composition and Accretion History of Terrestrial Planets.
 1192 *Philos. Trans. R. Soc. A Math. Phys. Eng. Sci.* **325**, 545–557.
- 1193 Watson E. B., Cherniak D. J., Hanchar J. M., Harrison T. M. and Wark D. A. (1997) The
 1194 incorporation of Pb into zircon. *Chem. Geol.* **141**, 19–31.
- 1195 Witt-Eickschen G., Palme H., O'Neill H. S. C. and Allen C. M. (2009) The geochemistry of the
 1196 volatile trace elements As, Cd, Ga, In and Sn in the Earth's mantle: New evidence from in situ
 1197 analyses of mantle xenoliths. *Geochim. Cosmochim. Acta* **73**, 1755–1778.
- 1198 Wolf R., Richter G. R., Woodrow A. B. and Anders E. (1980) Chemical fractionations in
 1199 meteorites—XI. C2 chondrites. *Geochim. Cosmochim. Acta* **44**, 711–717.
- 1200 Wolf R. and Anders E. (1980) Moon and Earth: compositional differences inferred from siderophiles,
 1201 volatiles, and alkalis in basalts. *Geochim. Cosmochim. Acta* **44**, 2111–2124.
- 1202 Wombacher F., Rehkämper M. and Mezger K. (2004) Determination of the mass-dependence of
 1203 cadmium isotope fractionation during evaporation. *Geochim. Cosmochim. Acta* **68**, 2349–2357.
- 1204 Wombacher F., Rehkämper M., Mezger K., Bischoff A. and Münker C. (2008) Cadmium stable
 1205 isotope cosmochemistry. *Geochim. Cosmochim. Acta* **72**, 646–667.
- 1206 Wood B. J. and Halliday A. N. (2010) The lead isotopic age of the Earth can be explained by core
 1207 formation alone. *Nature* **465**, 767–70.
- 1208 Wood B. J., Kiseeva E. S. and Mirolo F. J. (2014) Accretion and core formation: the effects of sulfur
 1209 on metal-silicate partition coefficients. *Geochim. Cosmochim. Acta* **145**, 248–267.
- 1210 Wood B. J., Smythe D. J. and Harrison T. (2019) The condensation temperatures of the elements: a
 1211 reappraisal. *Am. Min.* **104**(6), 844–856.
- 1212 Wood B. J. and Wade J. (2013) Activities and volatilities of trace components in silicate melts: a
 1213 novel use of metal-silicate partitioning data. *Contrib. to Mineral. Petrol.* **166**, 911–921.
- 1214 Wood B. J., Walter M. J. and Wade J. (2006) Accretion of the Earth and segregation of its core.
 1215 *Nature* **441**, 825–33.
- 1216 Wulf A. V., Palme H. and Jochum K. P. (1995) Fractionation of volatile elements in the early solar
 1217 system: evidence from heating experiments on primitive meteorites. *Planet. Space Sci.* **43**, 451–
 1218 468.
- 1219 Yamauchi M. and Wahlund J.-E. (2007) Role of the ionosphere for the atmospheric evolution of

1220 planets. *Astrobiology* **7**, 783–800.
 1221 Young E. D., Shahar A., Nimmo F., Schlichting H. E., Schauble E. A., Tang H. and Labidi J. (2019).
 1222 Near-equilibrium isotope fractionation during planetesimal evaporation. *Icarus*, **323**, 1–15.
 1223 Yu Y., Hewins R. H., Alexander C. M. O. 'D. and Wang J. (2003) Experimental study of evaporation
 1224 and isotopic mass fractionation of potassium in silicate melts. *Geochim. Cosmochim. Acta* **67**,
 1225 773–786.

1226
 1227

1228 Figure captions

1229 *Fig. 1.* Back-scattered electron images of four experimental glasses at the same magnification (1000 μm scale bar shown), a)
 1230 3M-29/02/16, 1400 $^{\circ}\text{C}$, $\log f\text{O}_2 = -0.68$, 60 minutes; b) 1M-1/3/16, 1400 $^{\circ}\text{C}$, $\log f\text{O}_2 = -10.01$, 60 minutes; c) 2M-16/07/16h,
 1231 1550 $^{\circ}\text{C}$, $\log f\text{O}_2 = -6.01$, 15 minutes; d) P-11/06/18b, 1550 $^{\circ}\text{C}$, $\log f\text{O}_2 = -5.48$, 15 minutes.

1232 *Fig. 2.* Concentrations of volatile elements (K, Cr, Cu, Zn, Ga, Ge, Rb, Mo, Ag, Cd, Pb; N = 38) in an experimental glass
 1233 (pair 1) plotted relative to their concentrations in another experimental glass run under the same conditions (pair 2) for four
 1234 experimental pairs. The different shades correspond to the following experimental pairs (pair 1, pair 2): black (P-09/06/18b,
 1235 P-09/06/18a), 1400 $^{\circ}\text{C}$, $\log f\text{O}_2 = -9.23$, 15 minutes; dark grey (P-08/02/17b, 3M-29/2/16), 1400 $^{\circ}\text{C}$, $\log f\text{O}_2 = -0.68$, 60
 1236 minutes; light grey (P-09/06/18c, 1M-PS1), 1400 $^{\circ}\text{C}$, $\log f\text{O}_2 = -5.50$, 60 minutes; white (1M-2/3/16, C18/12/15), 1400 $^{\circ}\text{C}$,
 1237 $\log f\text{O}_2 = -3.07$, 60 minutes.

1238 *Fig. 3.* Measurement of elemental zoning profiles in sample 3M-29/02/16 (1400 $^{\circ}\text{C}$, 60 mins, air). Panel a) shows a reflected
 1239 light image of the glass and laser spot profiles. Panel b) displays the fraction of a volatile element i remaining in the glass
 1240 (Ga, green; Zn, red; Cu, blue; Ge, purple; Rb, blue; Mo, orange) as a function of distance from rim to rim, corresponding to
 1241 the uppermost profile in panel a), with 25 μm spots at 100 μm spacing.

1242 *Fig. 4.* Vaporisation of a) Na, b) K, c) Rb, and d) Cu – elements with one oxidation state in the liquid and one species in the
 1243 gas, corresponding to vaporisation reactions with $n = 1$ stoichiometry (eq. 4). The fraction of the element remaining in the
 1244 glass after a run duration of 60 minutes (Na and K) or 15 minutes (Rb and Cu), relative to its initial concentration in the glass
 1245 $\left(\frac{x_i^f}{x_i^0}\right)$ are plotted as a function of $\log f\text{O}_2$. Lines at the top denote the location of the FMQ buffer as a function of temperature.
 1246 Curves are non-linear least-squares fits (see eq. 9) to the experimental data using eq. (8), shown along with the $\log K^*$ values
 1247 to which they correspond. Colours of lines, curves and symbols denote the temperature of the experiment; blue = 1300 $^{\circ}\text{C}$,
 1248 green = 1400 $^{\circ}\text{C}$, yellow = 1500 $^{\circ}\text{C}$, red = 1550 $^{\circ}\text{C}$.

1249 *Fig. 5.* Vaporisation of a) Zn and b) Ge – elements with one oxidation state in the liquid and one gas species, corresponding
 1250 to vaporisation reactions with $n = 2$ stoichiometry (eq. 4). The fraction of the element remaining in the glass after a run
 1251 duration of 15 minutes, relative to its initial concentration in the glass $\left(\frac{x_i^f}{x_i^0}\right)$ is plotted as a function of $\log f\text{O}_2$. Lines at the top
 1252 denote the location of the FMQ buffer. Colours and nomenclature are as per Fig. 4.

1253 *Fig. 6.* Vaporisation of a) Li, b) Ga and c) Pb – elements with one oxidation state in the liquid and multiple species in the
 1254 gas. The fraction of the element remaining in the glass after an experimental run, relative to its initial concentration in the
 1255 glass $\left(\frac{x_i^f}{x_i^0}\right)$ is plotted as a function of a) time for Li. Shown are experiments performed at a single temperature, 1400 $^{\circ}\text{C}$, at
 1256 two $\log f\text{O}_2$ s, -0.68 (white circles) and -8.00 (black circles). Both series are fit by non-linear least squares using eq. 8
 1257 corresponding to the reactions $\text{LiO}_{0.5}(\text{l}) + \frac{1}{4}\text{O}_2 = \text{LiO}(\text{g})$ for a $\log K^*$ of -3.39 (white circles) and $\text{LiO}_{0.5}(\text{l}) = \text{Li}(\text{g}) + \frac{1}{4}\text{O}_2$
 1258 with $\log K^*$ of -5.36 (black circles). Parts b) and c) plot $\left(\frac{x_i^f}{x_i^0}\right)$ against $\log f\text{O}_2$ for Ga and Pb, respectively. Lines at the top
 1259 denote the location of the FMQ buffer. Symbols and nomenclature as per Fig. 4. All experiments shown were run for 15

1260 minutes. The two $\log K^*$ s for Ga correspond to the reactions $\text{GaO}_{1.5}(\text{l}) = \text{GaO}(\text{g}) + \frac{1}{4}\text{O}_2$ (normal script) and $\text{GaO}_{1.5}(\text{l}) = \text{Ga}(\text{g})$
1261 $+ \frac{3}{4}\text{O}_2$ (italic); and for Pb, $\text{PbO}(\text{l}) = \text{PbO}(\text{g})$ (normal script) and $\text{PbO}(\text{l}) = \text{Pb}(\text{g}) + \frac{1}{2}\text{O}_2$ (italic).

1262 *Fig. 7.* Vaporisation of the Group VI elements – a) Mo and b) Cr – that have multiple species in the liquid and at least one
1263 species in the gas, whose net vaporisation reactions have $n < 0$ stoichiometry (see eq. 4). The fraction of the element
1264 remaining in the glass after a run duration of 15 minutes, relative to its initial concentration in the glass $\left(\frac{X_i^t}{X_i^0}\right)$ is plotted as a
1265 function of $\log f\text{O}_2$. Lines at the top denote the location of the FMQ buffer. Colours and nomenclature are as per Fig. 4. For
1266 Mo, the $\log K^*$ values shown correspond to the reaction: $\text{MoO}_3(\text{l}) = \text{MoO}_3(\text{g})$, and for Cr the $\log K^*$ values shown correspond
1267 to the reaction: $\text{CrO}(\text{l}) + \frac{1}{2}\text{O}_2 = \text{CrO}_2(\text{g})$.

1268 *Fig. 8.* Activity coefficients (γ) of melt oxide species (i) at infinite dilution (∞) in a ferrobaltic FCMAS liquid calculated
1269 by eq. 6, as a function of temperature. Melt oxide species are: $\text{CuO}_{0.5}$ = teal, $\text{LiO}_{0.5}$ = yellow, $\text{AgO}_{0.5}$ = grey, ZnO = blue,
1270 PbO = light orange, CdO = red, GeO_2 = purple, $\text{NaO}_{0.5}$ = sky blue, $\text{KO}_{0.5}$ = dark orange, $\text{RbO}_{0.5}$ = black. The two light
1271 orange ‘PbO’ series denote $\gamma_{\text{PbO}}^\infty$ calculated by two reactions, $\text{PbO}(\text{l}) = \text{PbO}(\text{g})$ (lower series) and $\text{PbO}(\text{l}) = \text{Pb}(\text{g}) + \frac{1}{2}\text{O}_2$
1272 (upper series). The two data points shown for $\text{LiO}_{0.5}$ denote $\gamma_{\text{LiO}_{0.5}}^\infty$ calculated at $\log f\text{O}_2$ -8.00 by the reaction $\text{LiO}_{0.5}(\text{l}) = \text{Li}(\text{g})$
1273 $+ \frac{1}{4}\text{O}_2$ and at $\log f\text{O}_2 = -0.68$ by the reaction $\text{LiO}_{0.5}(\text{l}) + \frac{1}{4}\text{O}_2 = \text{LiO}(\text{g})$.

1274 *Fig. 9.* The Gibbs Free Energy, ΔG^* , in kJ/mol against temperature (K) for element vaporisation reactions from a
1275 ferrobaltic liquid in the FCMAS system at 1 bar of a) Rb, $\text{RbO}_{0.5}(\text{l}) = \text{Rb}(\text{g}) + \frac{1}{4}\text{O}_2$ b) Cu, $\text{CuO}_{0.5}(\text{l}) = \text{Cu}(\text{g}) + \frac{1}{4}\text{O}_2$ c) Zn,
1276 $\text{ZnO}(\text{l}) = \text{Zn}(\text{g}) + \frac{1}{2}\text{O}_2$ d) Ge, $\text{GeO}_2(\text{l}) = \text{GeO}(\text{g}) + \frac{1}{2}\text{O}_2$. Greyscale denotes $f\text{O}_2$ series run at constant temperature with
1277 different times, White = 15 minutes, Black = 60 minutes, Grey = 120 minute. Best fits to all data points *via* the 2nd-law
1278 method yield the ΔG^* as a function of temperature (shown in panel).

1279 *Fig. 10.* Enthalpy (ΔH)-Entropy (ΔS) correlations for vaporisation reactions that are a) experimentally-derived (see section
1280 4.7. and Table 5) and b) in the pure system (see Table 5). Labels refer to the stable gas species. Colours as per Fig. 8 with the
1281 addition of Ga and GaO (fuchsia), CrO_2 (green) for the reaction $\text{CrO}(\text{l}) + \frac{1}{2}\text{O}_2 = \text{CrO}_2(\text{g})$ and MoO_3 (magenta) for the
1282 reaction $\text{MoO}_2(\text{l}) + \frac{1}{2}\text{O}_2 = \text{MoO}_3(\text{g})$.

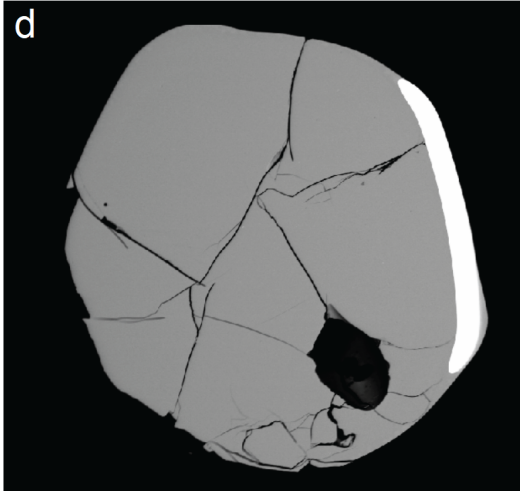
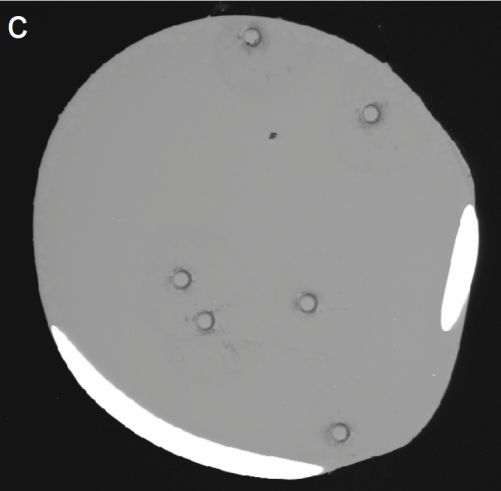
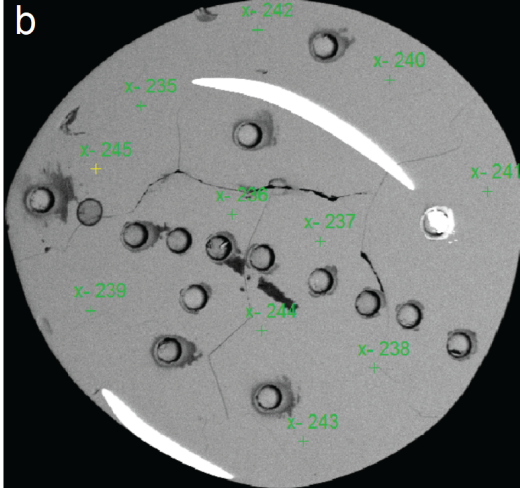
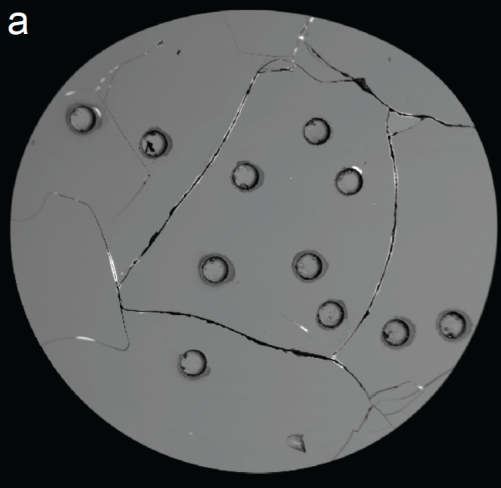
1283 *Fig. 11.* Experimental data from the literature. a) Fraction of Na remaining in chondrule-like glass as a function of time at
1284 different temperatures (Tsuchiyama et al., 1981). Circles refer to ‘composition 1’; blue = 1450 °C, green = 1500 °C, yellow
1285 = 1550 °C, red = 1600 °C; the square symbols refer to ‘composition 2’ at 1586 °C. Curves are fits with eq. 8 assuming an $n =$
1286 1 evaporation stoichiometry, and numbers correspond to $\log K^*$ values. b) Data of Kreuzberger et al. (1986) showing the
1287 fraction of Na (blue), K (orange) and Rb (black) remaining in a $\text{Di}_{75}\text{An}_{25}$ glass composition at 1400 °C in air as a function of
1288 time. Curves are fits with eq. 8 assuming an $n = 1$ evaporation stoichiometry, and numbers correspond to $\log K^*$ values. c)
1289 Data of Norris and Wood (2017) showing the fraction of Cu (teal), Zn (blue), Ga (crimson), Ge (purple) and Pb (orange)
1290 remaining in MORB glass after 60 minutes at 1300 °C, as a function of $\log f\text{O}_2$. The fits to the data are made relative to Zn,
1291 with eq. (19).

1292 *Fig. 12.* Nebular half condensation temperatures (T_c^{50}) of a) Lodders (2003) and b) Wood et al. (2019) compared to 1%
1293 evaporation temperatures for metal oxides from a ferrobaltic silicate melt at 1 bar and $\log f\text{O}_2 = -10$, calculated from the
1294 experiments, except for Mn, Mg, Fe, Co, Ni and Cr, which are taken from thermodynamic data in the pure system (Table 5).
1295 Chalcophile = orange, Siderophile = grey, Lithophile = green. Line of best fit (black) to lithophile elements only.

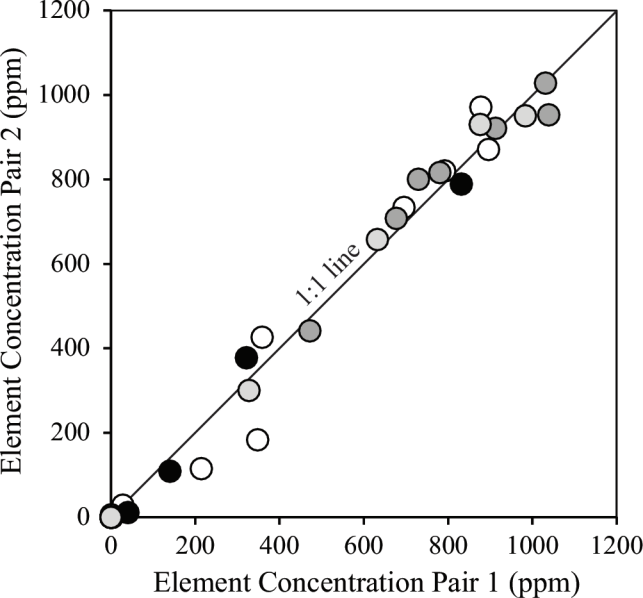
1296 *Fig. 13.* 1% evaporation temperatures for metal oxides from a ferrobaltic in the FCMAS system at 1 bar as a function of \log
1297 $f\text{O}_2$, calculated from thermodynamic data from the experiments, except for Mn, Mg, Fe, Co, Ni and Cr (below IW-1), which
1298 are taken from the pure system (Table 5). Dotted coloured lines (Li, Na, K, Mo, Cr) indicate that evaporation temperatures
1299 are calculated assuming their activity coefficients are constant with temperature (For Li, Na, K calculated at 1673 K, for Mo

1300 and Cr fixed by literature values at 1673 K) and hence uncertain outside of this temperature. In general, caution should be
1301 exercised in use of evaporation temperatures calculated outside of the experimental range (grey field). Dashed grey lines
1302 show the fO_2 defined by mineral oxygen buffers (IW = Iron-Wüstite, FMQ = Fayalite-Magnetite-Quartz, MH = Magnetite-
1303 Hematite).

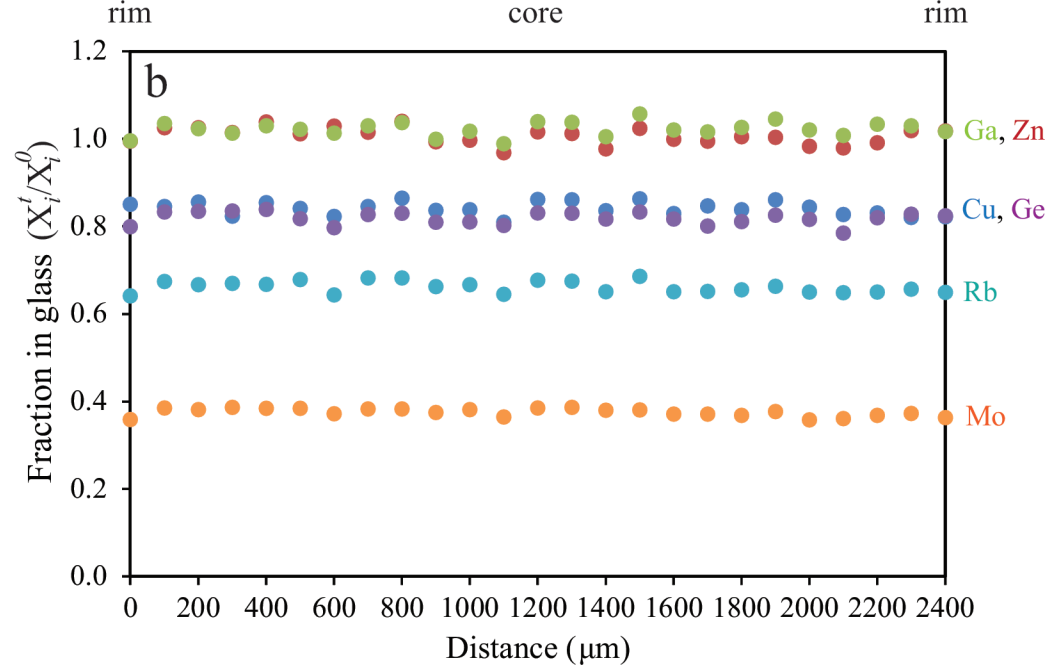
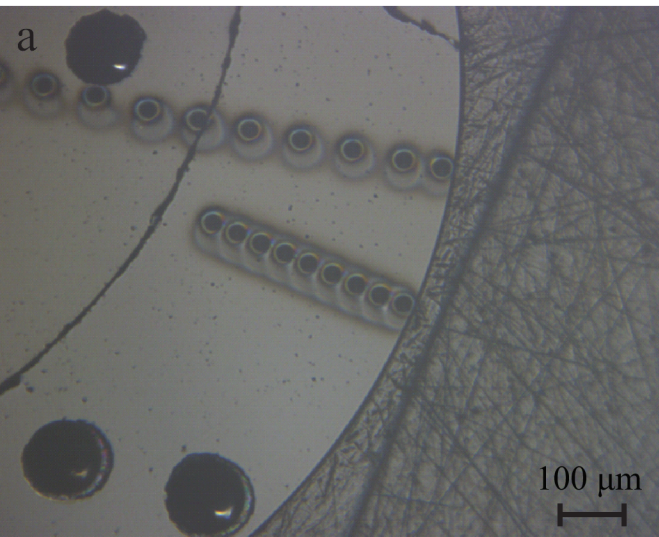
1304 *Fig. 14.* Elemental depletion factors normalised to Mg in a residual ferrobalt melt after Langmuir evaporation at 1 bar
1305 calculated with eq. 19. Elements are plotted in order of their volatilities from the ferrobalt composition. a) At constant
1306 relative fO_2 (FMQ buffer) and variable temperature (listed next to lines in K) and b) At constant temperature and variable
1307 relative fO_2 (Δ FMQ listed next to lines). Also plotted are the estimated elemental abundances of lithophile and weakly
1308 siderophile elements in the Earth's primitive mantle (Palme and O'Neill, 2014; green circles) and the Moon's primitive
1309 mantle (O'Neill, 1991, Ni et al. 2019; grey circles).



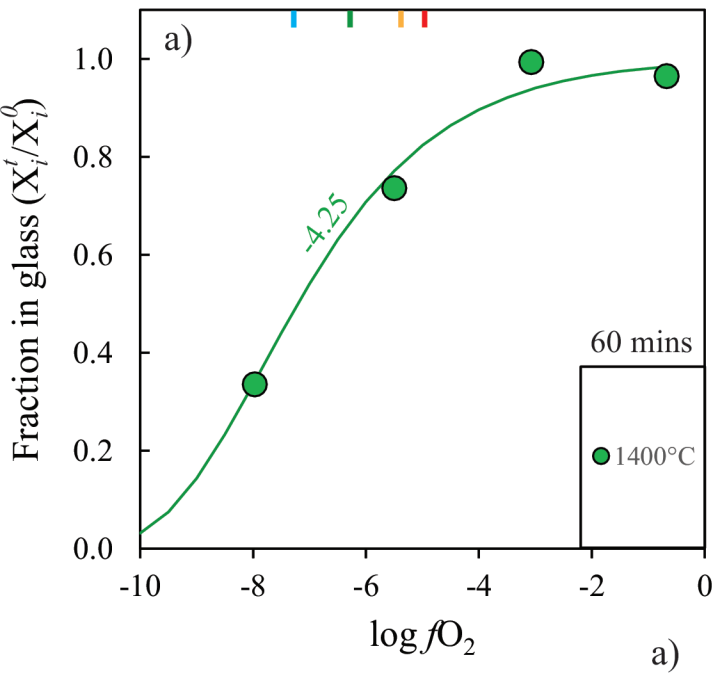
1000 μm



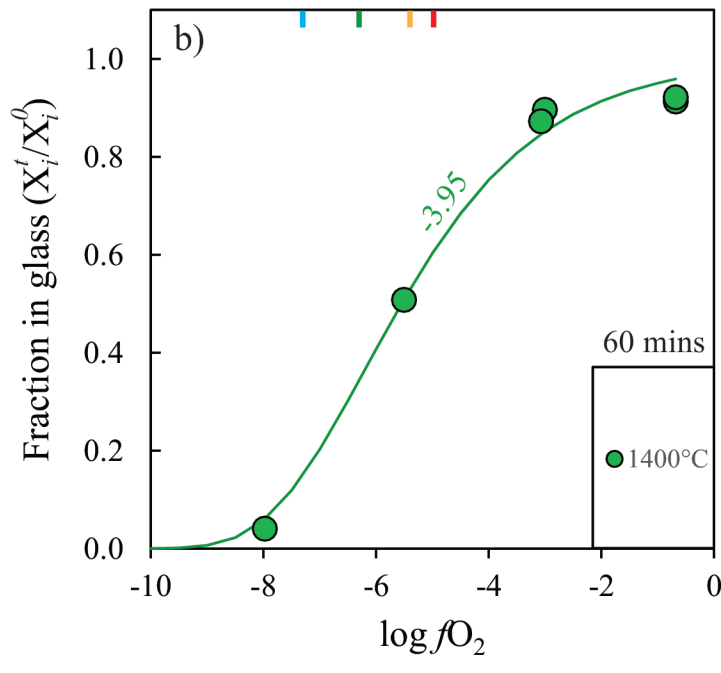
Sample 3M-29/02/16 (1400 °C, 60 mins, air)



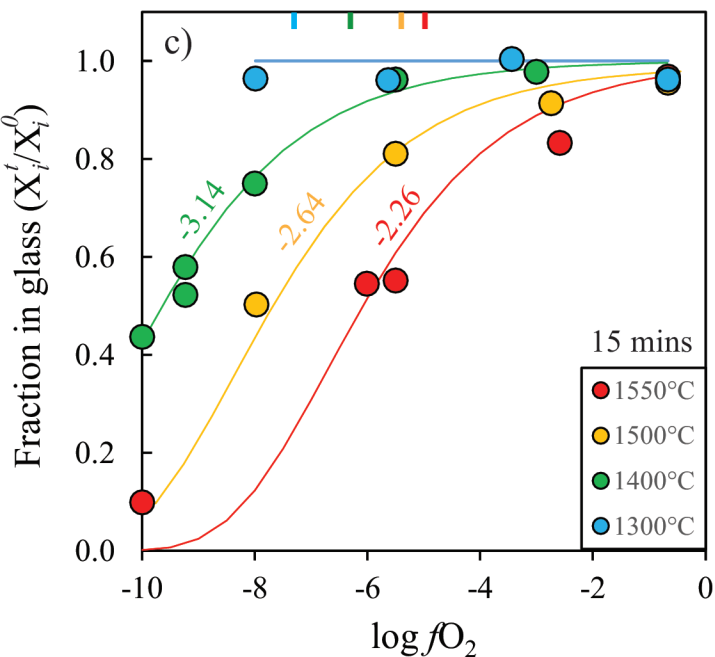
Na



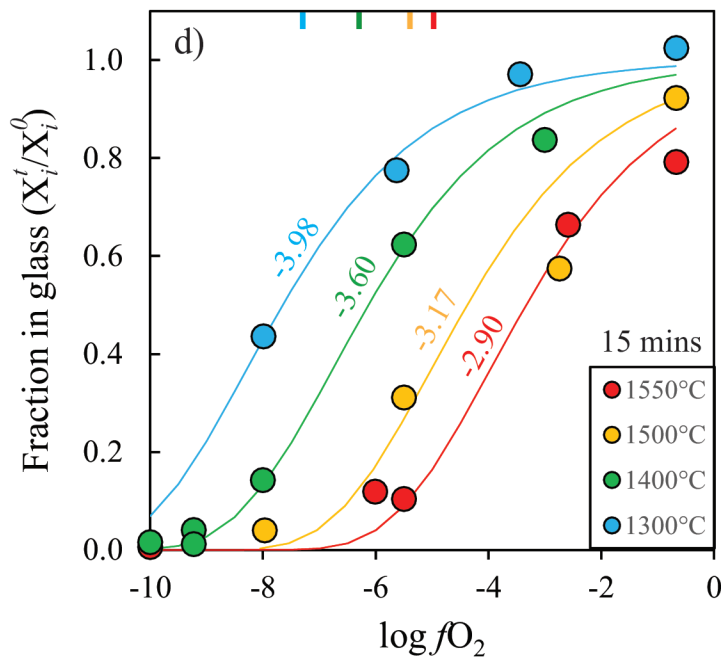
K

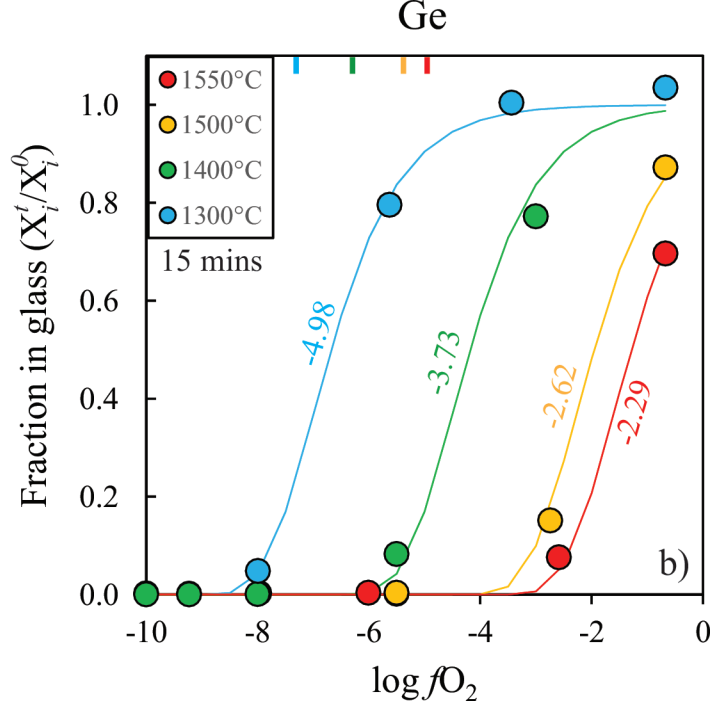
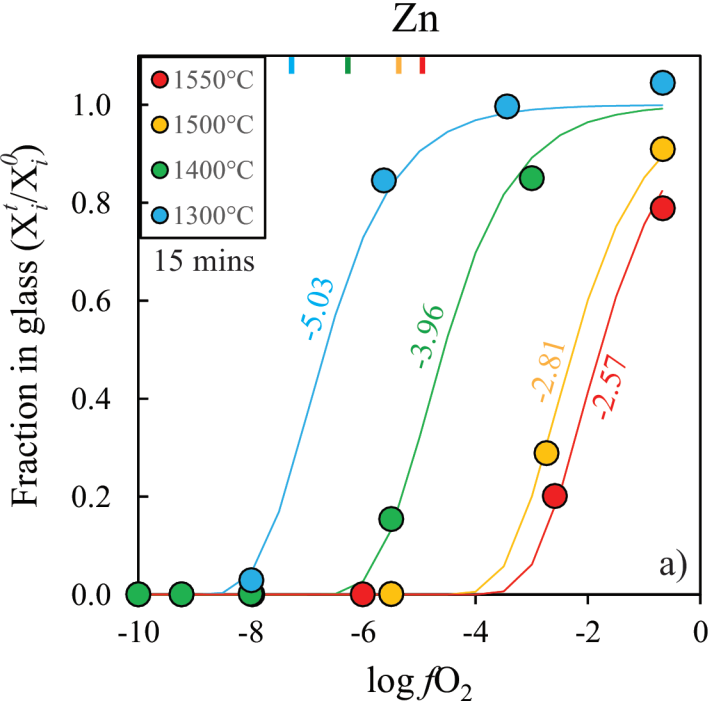


Rb

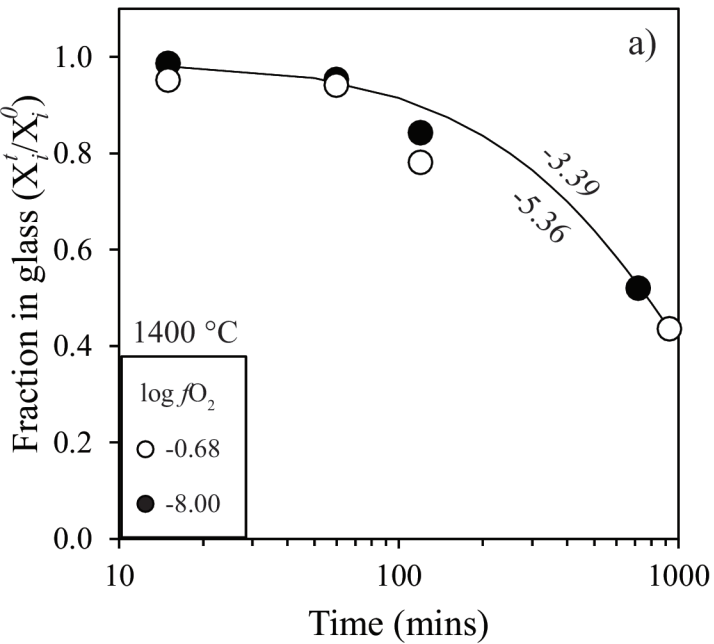


Cu

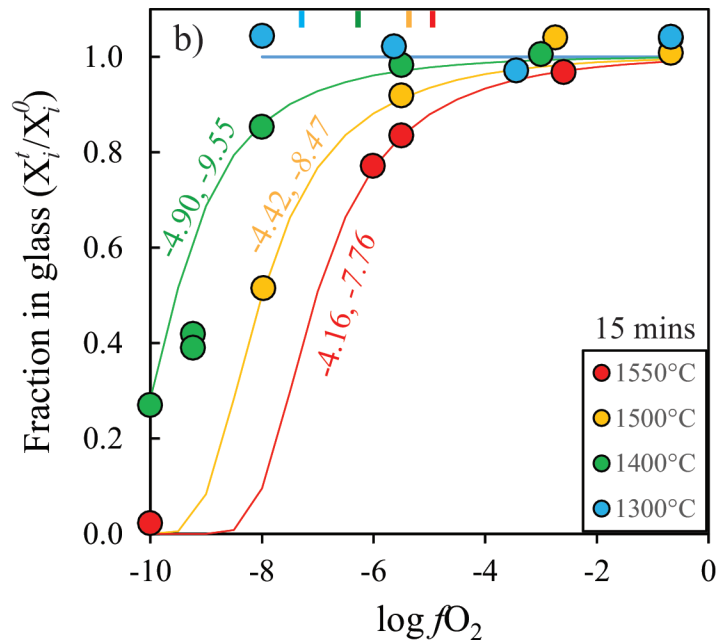




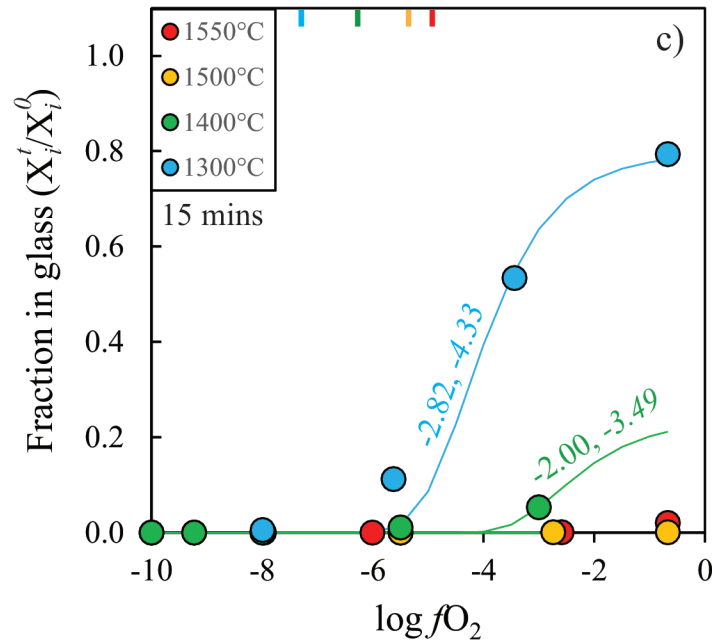
Li



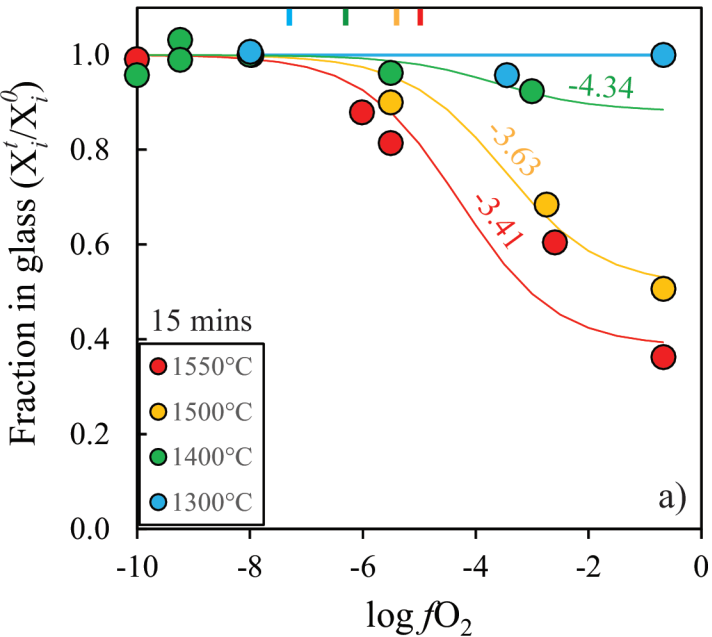
Ga



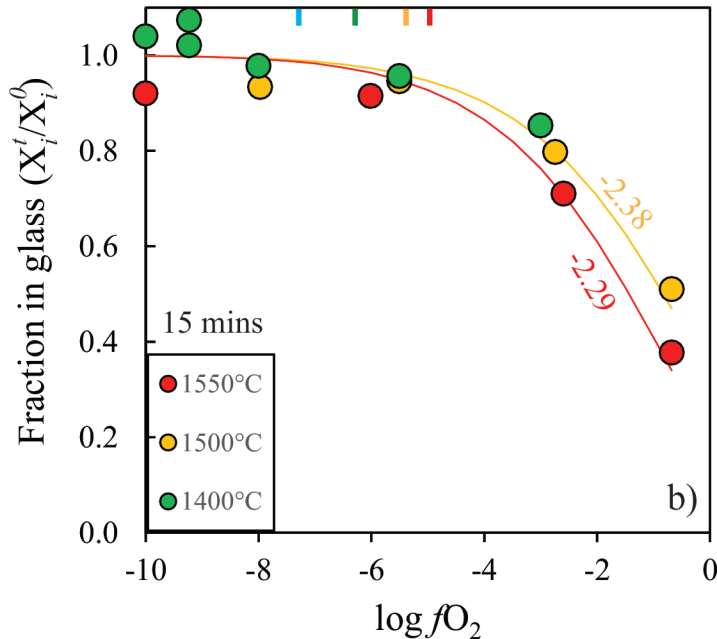
Pb

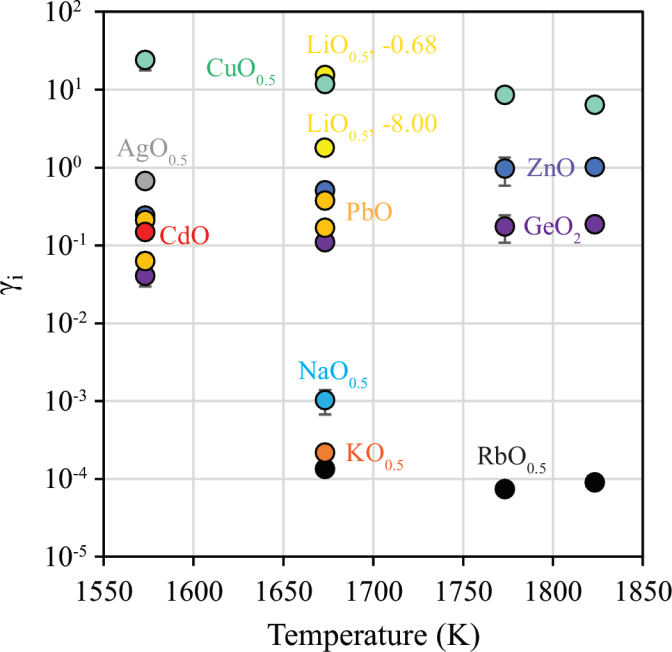


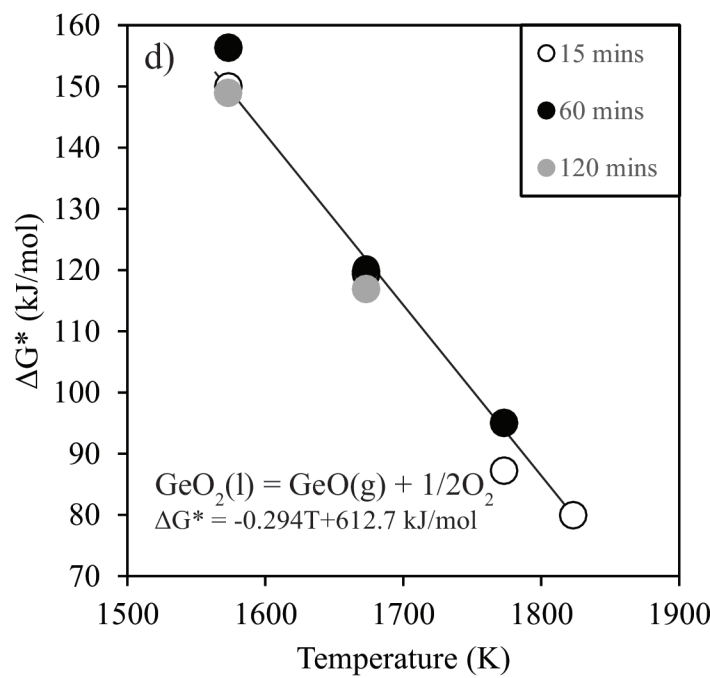
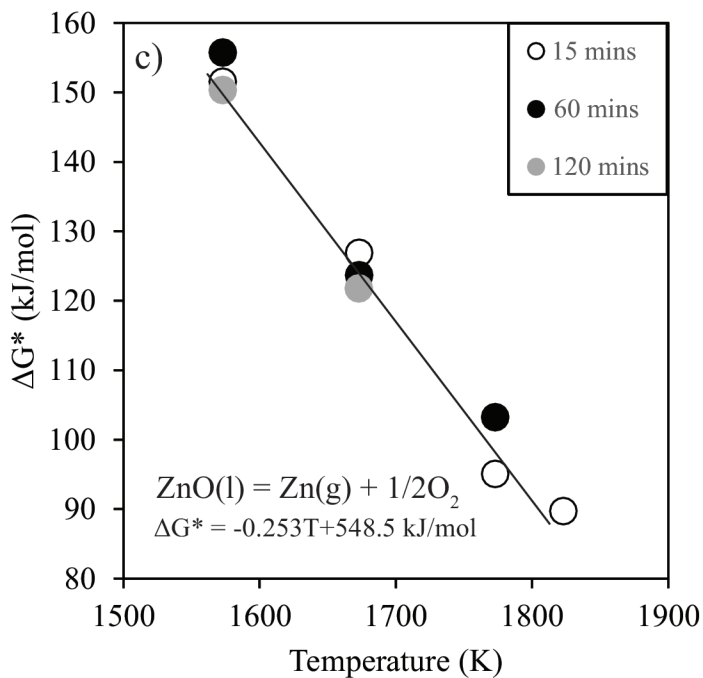
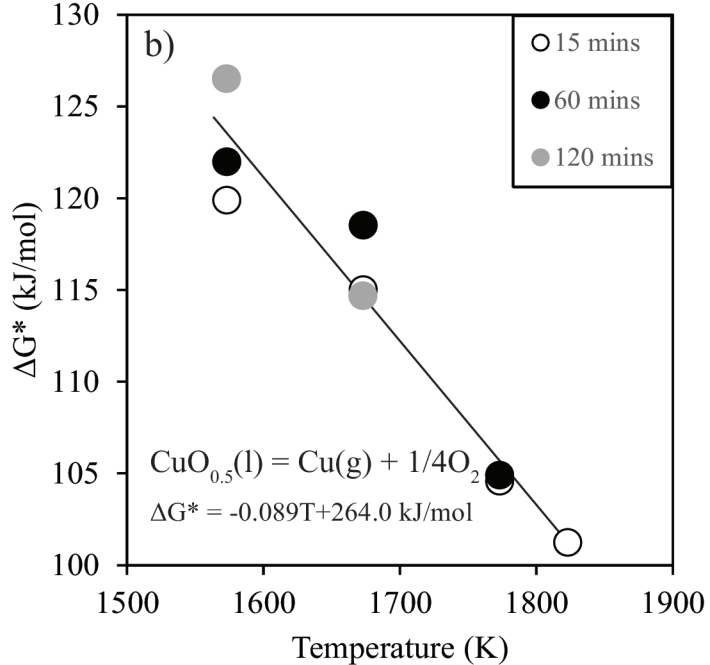
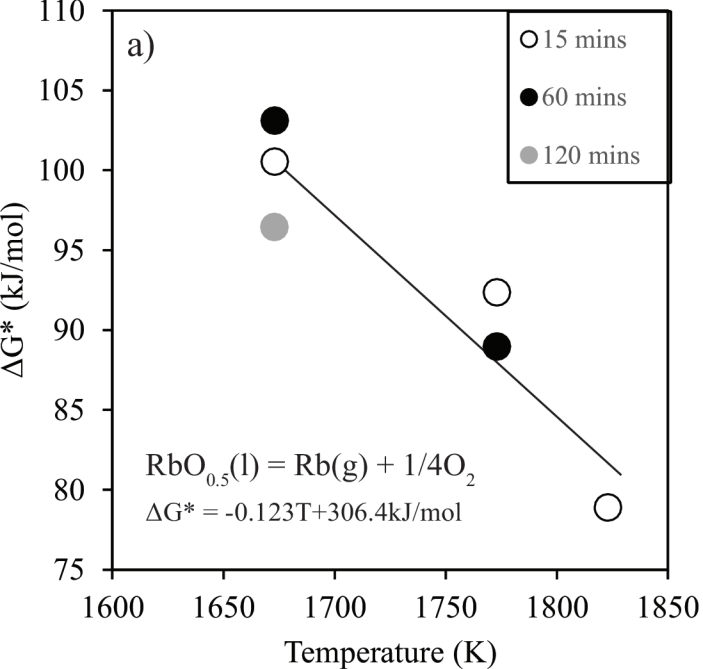
Mo



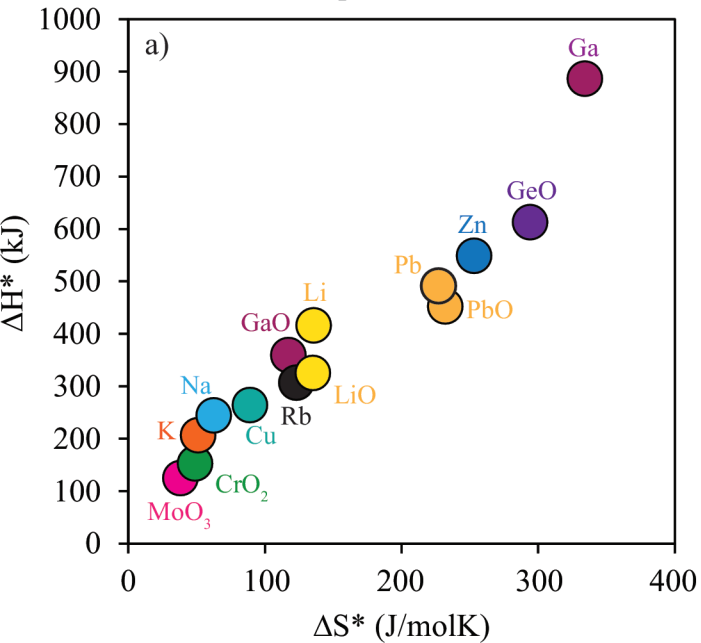
Cr



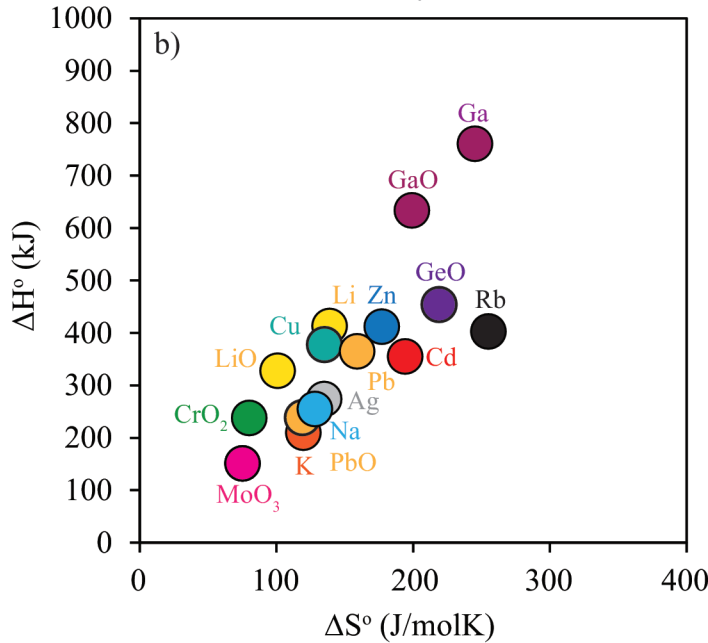


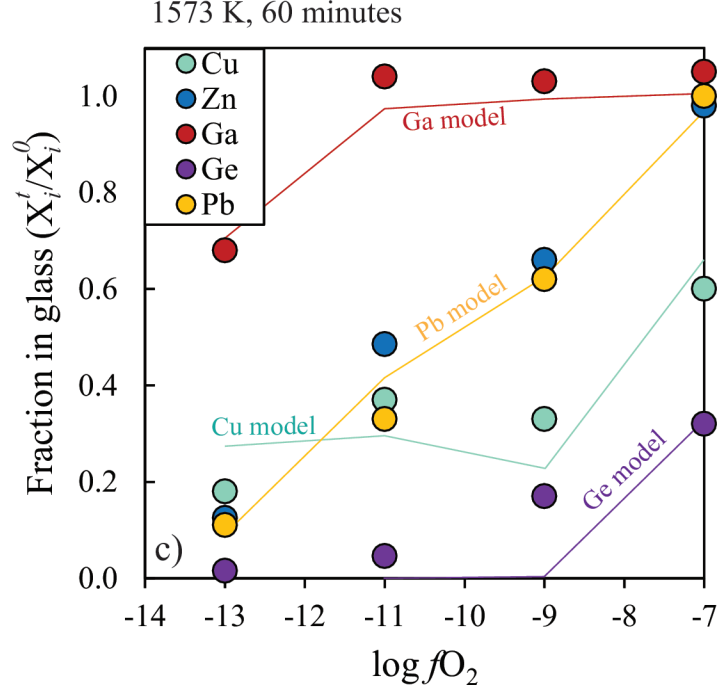
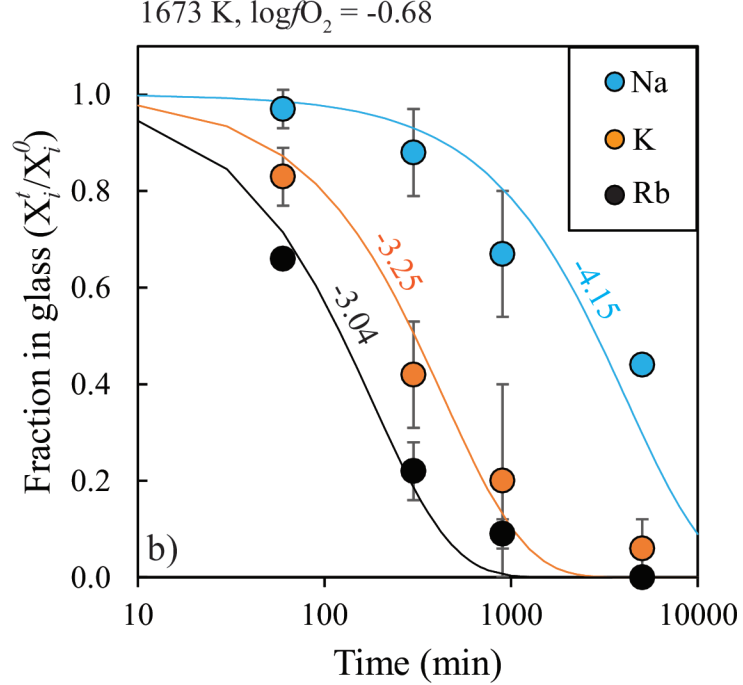
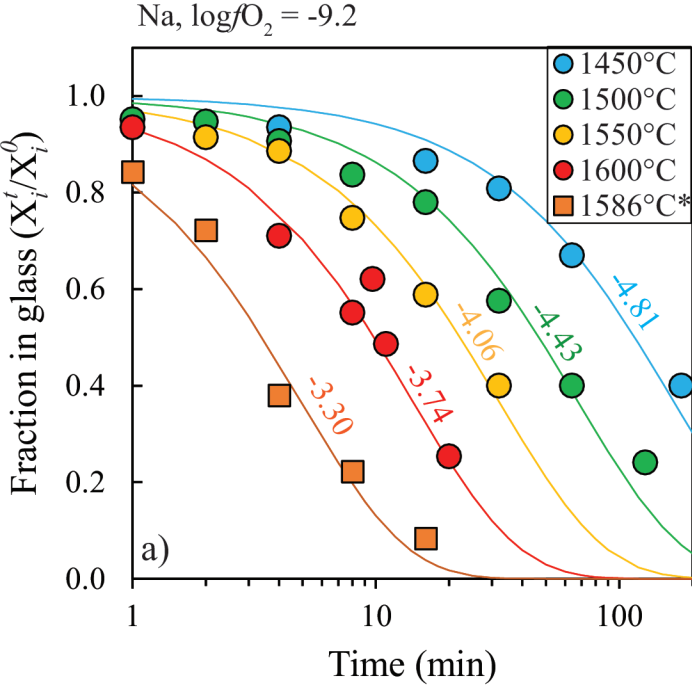


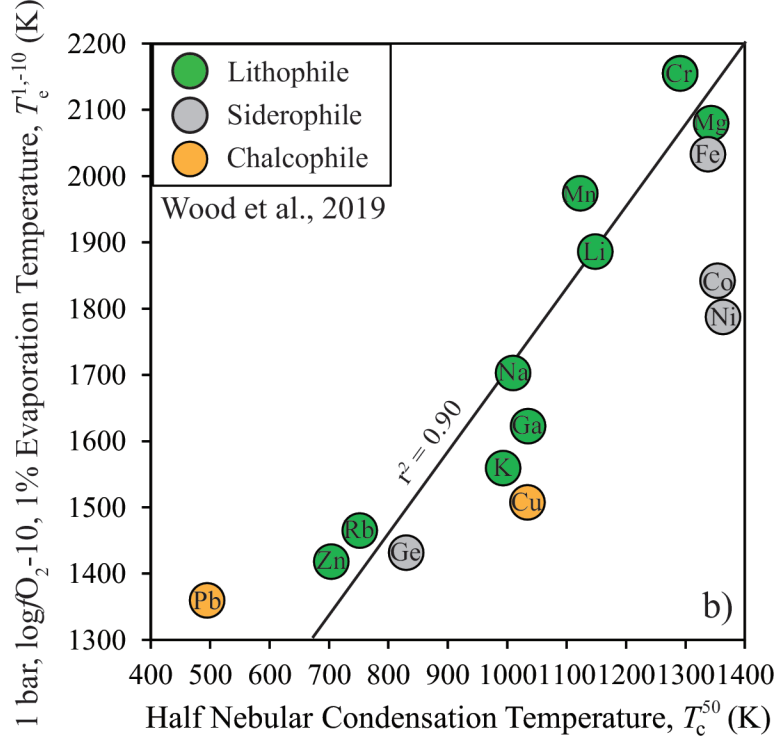
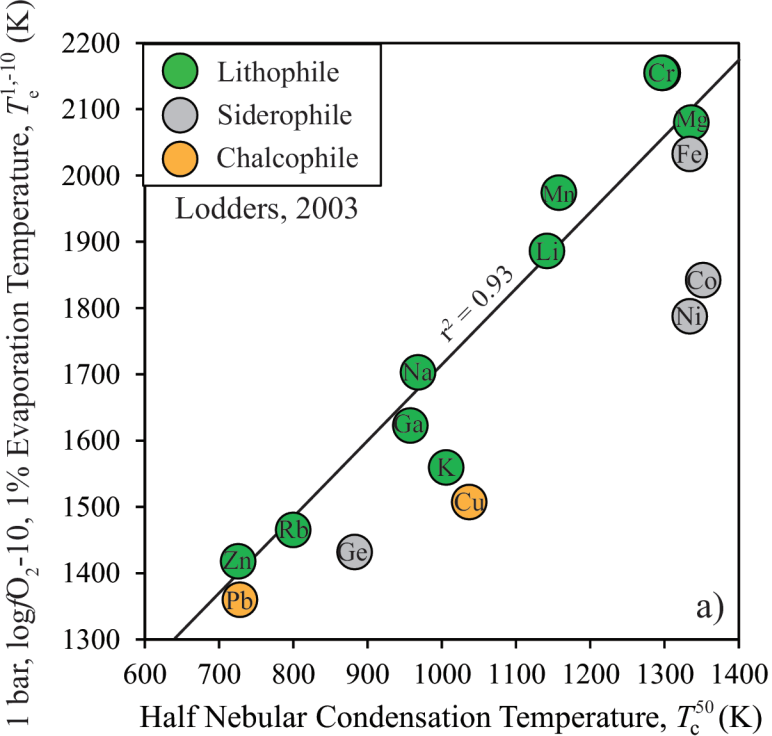
Experimental

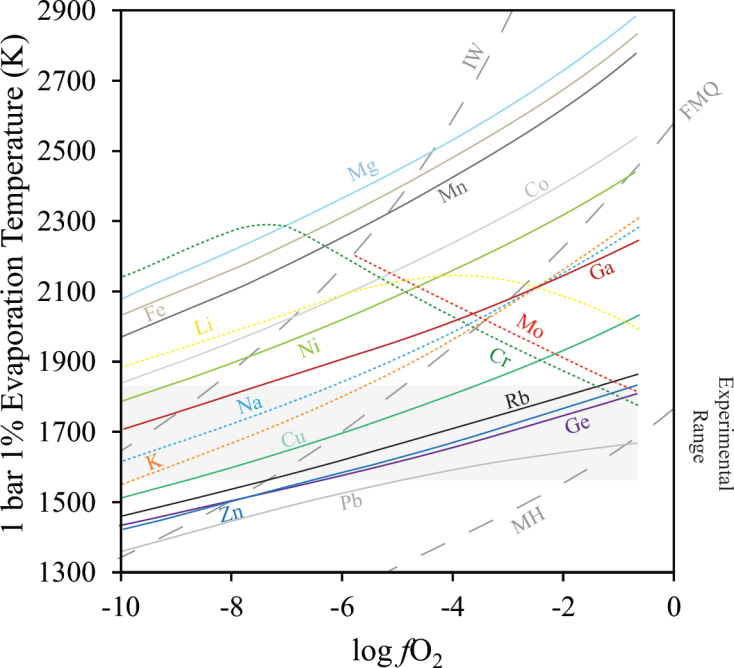


Pure System









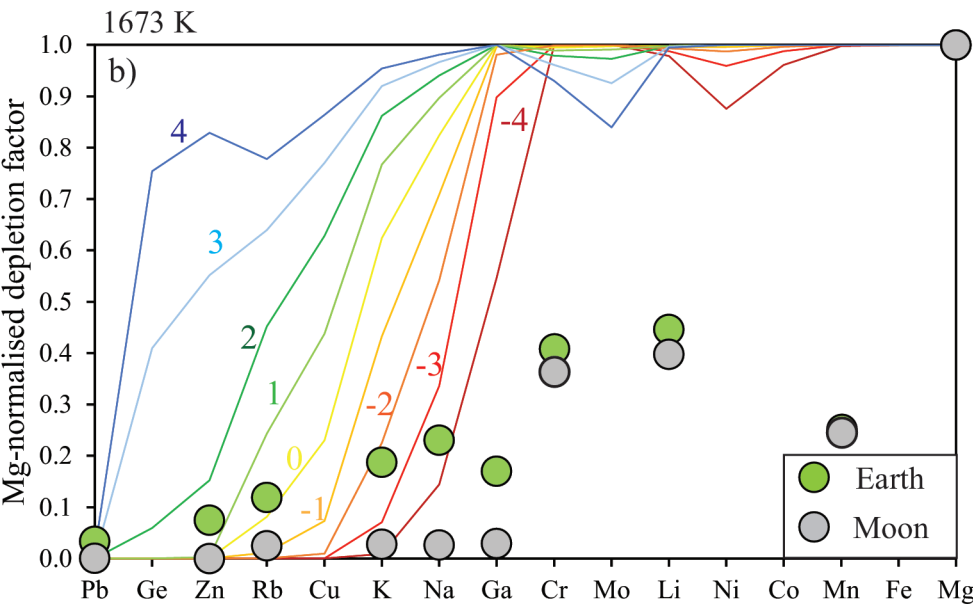
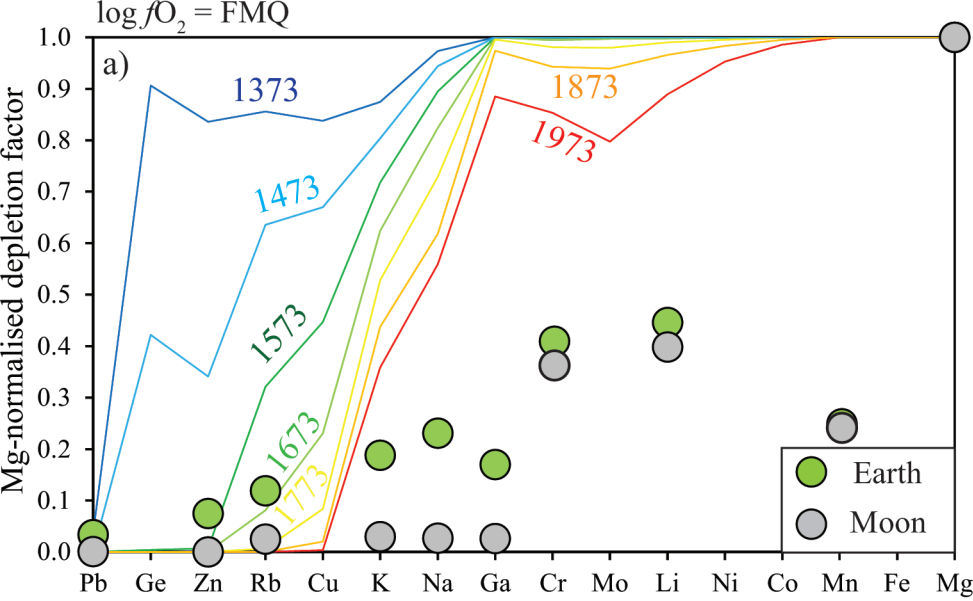


Table 1. Major (in wt. %) and trace element (in ppm) composition of the starting mixture. The ‘calculated’ column refers to that expected from added weights. The ‘measured’ column refers to EPMA analyses of glasses unaffected by Fe-loss or crystallisation post-experiment (major elements) and solution ICP-MS analyses of the de-carbonated powder pre-experiment (trace elements).

	Calculated	Measured	St. Dev.
wt. %		<i>N</i> = 8	
SiO ₂	40.76	40.60	0.21
Al ₂ O ₃	10.52	10.67	0.22
MgO	15.78	15.40	0.23
FeO	16.25	16.26	0.12
CaO	16.69	16.82	0.12
ppm		<i>N</i> = 2	
Li	1008.7	1020.0	17.8
Na	993.4	3252.3	281.3
K	1039.4	944.0	128.0
Sc	970.8	850.8	28.9
Ti	1008.0	1045.0	46.6
V	1019.7	1024.6	32.4
Cr	-	36.8	0.5
Mn	992.4	690.2	3.8
Cu	1009.5	1034.5	49.8
Zn	1015.5	1043.8	51.1
Ga	1019.3	1036.7	23.3
Ge	994.5	1007.7	44.6
Rb	1052.8	1036.1	62.4
Zr	991.9	1118.1	34.8
Mo	1029.0	1044.1	56.6
Ag	994.3	998.2	33.0
Cd	1037.0	991.1	33.2
La	1038.9	969.8	21.2
Gd	1063.3	1060.6	25.2
Yb	1036.2	1111.0	26.4
Pb	1002.7	1078.7	15.5

Table 2. Run conditions and LA-ICP-MS trace element data for all experiments. ‘Y’ denotes experiments analysed for 25 µm zoning profiles (‘Profile’) and trace element contents in the wire loop (‘Metal’). Experiments marked ‘*’ denote repeat experiments.

Run#	T (°C)	t (min)	CO (sccm)	CO ₂ (sccm)	logfO ₂	Loop	Profile	Metal	Li	Na	K	Sc	Ti	V	Cr	Mn	Ni	Cu	Zn	Ga	Ge	Rb	Zr	Mo	Ag	Cd	La	Gd	Yb	Pb
2M-15-07-16c	1300	15	-	-	-0.68	Pt	Y		1429.4	6501.2	1245.0	1085.4	1312.4	1098.9	5.5	759.6	-	1024.7	1044.8	1093.8	1034.5	961.7	1088.1	999.9	358.4	448.0	1113.8	1276.0	1273.7	896.2
2M-15-07-16d	1300	15	-	200	-3.44	Pt			1446.9	10376.3	1570.7	1040.7	1196.3	1141.8	10.7	747.0	51.4	971.2	996.1	1020.1	1003.8	1003.2	1184.7	957.2	194.9	84.3	973.9	1125.9	1124.8	478.7
2M-15-07-16g	1300	15	1.8	200	-5.63	Pt			1445.2	13585.8	1868.9	1100.5	1285.4	1270.7	20.1	775.6	-	774.5	845.5	1072.9	795.2	960.3	1193.6	1108.0	5.3	0.2	1055.9	1192.3	1207.0	150.3
2M-15-07-16h	1300	15	24	175	-7.99	Pt			1477.8	11402.1	1798.9	1138.9	1425.6	1412.2	32.7	805.9	40.3	435.6	29.1	1095.9	48.1	963.3	1262.9	1006.2	0.4	0.0	1124.1	1293.8	1296.7	5.1
2M-15-07-16f	1300	15	156	100	-10.10	Pt	Y	Y																						
P11-06-18a*	1300	60	-	200	-3.44	Pt			1121.1	3222.8	1162.0	1023.2	1120.8	1211.7	7.8	709.6	7.0	888.3	981.2	1005.2	876.4	792.8	1228.8	967.6	0.2	0.1	1061.3	1040.4	1073.8	275.0
1M-15-07-16a*	1300	60	-	200	-3.44	Pt			1272.2	6412.8	1358.7	1064.7	1235.9	1113.7	8.1	734.5	8.5	885.1	954.5	1069.0	866.4	782.5	1190.9	972.3	4.1	0.2	1009.0	1164.9	1175.6	244.7
1M-15-07-16b	1300	60	1.9	200	-5.67	Pt			1406.2	15818.1	2075.5	1203.7	1385.7	1403.4	22.2	800.5	112.7	401.1	264.8	1046.1	248.6	589.7	1374.1	975.0	0.3	0.2	1184.5	1358.1	1366.1	1.5
1M-PS6	1300	60	25	180	-8.00	Pt			1201.3	16757.9	2053.3	1184.2	1368.3	1343.1	34.4	782.9	58.1	95.6	10.6	1083.9	21.3	198.7	1252.8	1092.8	0.5	0.1	1087.5	1171.2	1149.3	0.3
3M-18-07-16b	1300	120	-	-	-0.68	Pt			1384.2	7547.0	1011.0	1053.5	1224.3	1015.7	2.8	593.4	24.6	1019.6	1087.6	993.4	1004.0	577.0	1193.4	263.7	0.4	0.0	1019.4	1175.1	1197.6	7.2
2M-18-07-16a	1300	120	-	200	-3.44	Pt			1314.2	8911.1	1495.8	1092.9	1255.8	1294.5	4.7	756.5	46.2	728.5	712.2	1068.0	640.8	983.9	1219.5	765.5	0.2	0.2	1068.6	1211.1	1218.7	15.4
2M-18-07-16c	1300	120	12	188	-7.33	Pt		Y	1405.9	9559.0	1500.9	1149.6	1417.5	1283.4	32.7	721.6	42.6	192.2	2.0	1186.1	4.3	899.1	1341.5	980.3	0.1	0.2	1132.0	1284.3	1284.6	0.0
1M-PS3	1400	15	-	180	-3.07	Pt			1046.6	13784.1	1687.2	1209.1	1276.6	1181.1	30.7	828.4	11.8	837.0	908.1	1055.6	782.0	977.3	1193.7	923.3	3.6	0.1	1028.8	1098.1	1101.8	52.7
1M-PS2	1400	15	5	180	-5.49	Pt			1054.4	10421.8	1504.8	1229.9	1258.3	1188.1	34.4	760.4	5.3	623.3	353.6	1032.1	272.2	961.7	1198.2	962.1	0.7	0.1	1024.4	1101.1	1091.8	10.7
1M-PS4	1400	15	66	133	-8.00	Pt		Y	1084.6	14426.0	1562.7	1240.4	1350.8	1218.0	35.2	833.9	10.5	142.1	1.4	895.7	0.8	749.0	1242.8	1000.4	0.2	0.1	1067.2	1170.6	1167.3	0.1
P09/06/18b*	1400	15	130	65	-9.23	Pt			1199.2	2013.9	732.4	1006.1	1156.0	1179.1	38.7	802.1	13.0	40.5	0.4	439.9	1.2	521.5	1092.2	1031.1	0.1	0.1	1003.8	930.5	947.3	0.0
P09/06/18a*	1400	15	130	65	-9.23	Re			1161.9	1901.2	684.2	1087.0	1180.8	1129.2	36.7	722.0	0.8	11.2	0.3	409.4	0.1	578.5	1126.5	989.7	0.1	0.0	1026.6	978.1	1006.7	0.0
1M-PS5	1400	15	167	33	-10.01	Pt		Y	1110.8	8419.1	1168.0	1177.3	1290.5	1223.5	37.4	851.2	6.9	15.6	0.3	283.2	0.4	436.3	1209.0	957.2	0.2	0.1	1020.5	1096.3	1090.7	0.0
P08-02-17b*	1400	60	-	-	-0.68	Pt			1034.8	3076.2	912.7	1112.2	1188.2	1190.2	9.1	692.7	9.1	840.3	1039.1	1031.2	729.2	677.1	1076.3	467.2	0.1	0.1	1033.8	1001.2	992.6	0.0
3M-29/2/16*	1400	60	-	-	-0.68	Pt	Y		1028.3	5703.4	921.1	1100.3	1084.4	1025.8	11.3	721.4	5.5	816.6	953.7	1028.4	800.6	708.0	1119.2	441.9	0.1	0.1	915.9	992.2	984.1	0.3
1M-2/3/16*	1400	60	-	200	-3.07	Pt			1129.1	10167.2	895.7	1279.7	1273.1	1148.6	28.1	863.9	13.5	695.1	348.0	878.0	214.0	358.6	1232.1	792.1	0.4	2.4	1074.7	1154.5	1178.0	3.4
C18/12/15*	1400	60	0	27	-3.07	Ir			1038.8	3167.7	911.7	1230.0	1346.1	1132.3	29.0	852.5	8.5	833.8	183.4	971.2	115.8	426.7	1090.0	820.8	0.1	0.2	1044.3	1121.8	1110.6	0.4
1M-PS1*	1400	60	5	180	-5.50	Pt		Y	1069.5	9048.0	1363.8	1008.1	1135.3	1194.8	35.6	784.8	5.5	300.5	6.5	930.5	1.6	57.7	1085.8	951.0	0.1	0.1	1037.6	1129.6	1113.6	0.1
P09/06/18c*	1400	60	5.5	195	-5.51	Re			1033.0	2345.0	547.1	1049.5	1135.7	1155.8	36.1	749.3	9.4	327.7	0.4	876.6	0.2	32.2	1011.0	983.2	0.1	0.1	1049.7	951.0	967.6	0.0
C17/12/15a	1400	60	13	27	-7.97	Re			1048.1	1068.8	40.2	1294.5	1418.9	1140.8	35.6	820.4	13.7	13.9	0.3	677.3	0.5	0.3	1499.7	980.2	0.1	0.1	1083.9	1199.7	1193.8	0.0
1M-1/3/16	1400	60	167	33	-10.01	Re		Y	1149.9	3924.1	5.2	1363.5	1396.8	1449.9	38.5	845.8	35.7	6.5	0.8	122.6	4.9	0.1	1132.6	947.5	0.1	0.1	1203.8	1276.6	1276.8	0.0
3M-1/3/16	1400	120	-	-	-0.68	Pt			858.8	20028.4	1102.7	1102.7	1323.2	1258.5	3.6	779.3	76.6	772.6	774.5	1041.6	577.5	368.7	1187.9	9.4	0.1	0.0	1117.6	1219.0	1247.2	0.2

C17/12/15b	1400	120	13	27	-7.97	Re			976.2	950.6	7.7	1223.9	1317.2	1129.1	36.4	754.6	23.6	10.5	0.3	564.1	0.3	0.3	1245.3	857.3	0.2	0.1	1022.5	1110.5	1111.9	0.0	
1M-1/3/16b	1400	120	167	33	-10.01	Re	Y		1044.3	1576.5	196.5	1320.6	1385.9	1280.5	36.0	819.9	56.2	4.4	0.2	19.1	2.2	8.3	1896.7	670.2	0.1	0.1	1159.5	1270.7	1275.3	0.0	
3M-29/2/16b	1400	930	-	-	-0.68	Pt			479.2	5993.0	541.0	1233.4	1170.0	1149.1	1.3	782.4	9.6	438.9	486.6	1086.2	96.4	113.6	1062.8	10.8	0.1	0.1	1033.7	1108.6	1132.6	0.1	
C17/12/15c	1400	720	13	27	-7.97	Re	Y	Y	571.9	32.6	1.1	1308.9	1349.0	1190.2	40.9	843.3	22.7	1.6	0.2	120.1	0.3	0.1	1013.3	718.4	0.1	0.1	1105.7	1196.4	1198.2	0.3	
2M-16-07-16e	1500	15	-	-	-0.68	Pt			952.5	7896.9	1199.2	1137.2	1319.0	1148.8	18.4	848.9	105.4	922.3	909.2	1058.2	872.3	955.1	1253.0	506.4	1.4	0.2	1034.3	1194.3	1220.7	0.6	
2M-16-07-16a	1500	15	-	200	-2.74	Pt			1217.1	10642.4	1384.8	1130.0	1219.5	1213.4	28.7	742.5	101.2	574.0	288.5	1092.7	151.3	912.9	1185.7	683.8	0.2	0.2	1025.7	1168.3	1191.4	0.5	
2M-16-07-16b	1500	15	16	184	-5.50	Pt			1319.4	4959.0	1205.5	1106.7	1238.0	1188.5	34.1	739.9	6.8	311.1	0.5	964.7	3.7	809.7	1155.6	899.5	0.1	0.1	988.5	1134.6	1158.2	0.1	
2M-16-07-16c	1500	15	120	80	-7.97	Re	Y		1287.4	4577.0	957.7	1081.0	1247.0	1154.1	33.6	738.1	7.8	39.5	0.2	540.4	2.8	501.9	1155.5	999.5	0.2	0.1	967.9	1117.7	1135.9	0.1	
3M-2/3/16	1500	60	-	-	-0.68	Pt			597.3	9378.6	1012.6	1227.5	1210.9	1200.3	3.8	764.0	13.2	570.6	566.3	1079.7	149.7	339.1	1136.7	23.6	0.1	0.6	1032.8	1092.1	1108.4	0.1	
2M-17-07-16a	1500	60	-	200	-2.74	Pt	Y		1307.9	5028.1	984.8	1069.1	1239.6	1095.5	21.6	717.7	21.8	372.7	66.1	1096.5	3.9	157.0	1155.0	347.0	0.2	0.2	980.9	1116.5	1136.9	0.1	
2M-17-07-16b	1500	60	16	184	-5.50	Pt		Y	1376.6	4711.9	727.7	1082.7	1214.1	1145.4	32.4	760.1	18.8	54.0	0.3	775.1	2.6	27.9	1163.7	609.4	0.1	0.2	991.7	1142.3	1160.1	0.0	
2M-17-07-16c	1500	60	120	80	-7.97	Pt		Y	1411.2	1842.0	281.8	1103.9	1312.0	1199.8	34.9	784.9	4.2	10.8	0.2	67.4	1.9	4.8	1158.8	944.1	0.1	0.1	1016.1	1138.9	1153.4	0.1	
2M-16-07-16f	1550	15	-	-	-0.68	Pt			580.9	11969.3	1808.5	1137.0	1298.5	1232.4	13.6	801.1	172.5	791.8	768.2	1091.2	696.2	967.6	1189.9	362.0	1.5	0.2	1051.4	1197.7	1212.1	19.9	
2M-16-07-16g	1550	15	-	200	-2.59	Pt			621.8	7199.0	1314.1	1149.4	1368.7	1175.1	25.6	825.4	50.3	663.5	251.1	1016.4	76.1	832.3	1240.3	604.2	0.3	0.2	1052.9	1198.4	1217.0	0.5	
P11-06-18b	1550	15	25	175	-5.48	Pt			1147.9	2485.5	865.2	1066.8	1123.5	1120.4	34.1	747.4	15.0	103.7	0.5	876.5	1.5	551.3	1057.7	813.9	0.2	0.1	1004.2	964.8	998.6	0.2	
2M-16-07-16h	1550	15	42	158	-6.01	Pt	Y	Y	1341.0	4106.7	957.5	1106.0	1239.6	1161.5	32.9	766.4	10.5	138.5	0.4	809.8	3.2	544.6	1201.6	879.0	0.2	0.2	1002.7	1144.9	1162.8	0.0	
2M-16-07-16d	1550	15	188	12	-9.56	Re			1361.8	2721.8	480.9	1079.6	1220.5	1108.4	33.1	819.6	5.1	5.7	0.2	22.8	2.3	118.8	1188.0	990.9	0.1	0.1	975.9	1117.6	1128.9	0.0	
<i>Blank Runs</i>																															
P28-05-18	1400	15	-	-	-0.68	Pt			0.1	92.1	77.7	0.3	2.0	0.4	1.2	1.3	6.3	1.6	3.0	0.1	0.1	0.1	0.2	0.4	0.1	0.2	0.3	3.1	0.0	1.4	
P23-05-18a	1400	60	50	100	-8.00	Re			0.2	45.7	12.1	0.4	1.3	0.3	0.1	1.1	34.5	1.0	0.2	0.4	0.1	0.1	0.2	7.3	0.0	0.0	0.2	4.1	0.0	0.0	
P24-05-18a	1500	60	93	60	-8.00	Re			0.3	25.6	1.5	0.3	1.6	0.4	1.1	2.2	119.5	1.4	0.2	2.5	0.1	0.1	0.2	5.9	0.0	0.0	0.3	3.4	0.0	0.0	
P24-05-18b	1500	120	93	60	-8.00	Re			0.3	15.6	0.6	0.3	1.7	0.4	1.7	2.2	101.8	0.8	0.2	1.9	0.1	0.0	0.2	10.8	0.0	0.0	0.3	3.9	0.0	0.0	

Table 3. The $\log K^*$ values and SD uncertainty and stoichiometries of reaction (n) found by non-linear least-squares fit to the experimental data.

Element	Reaction	n	t_0 (min)	$\log K^*$			
				1573.15 K	1673.15 K	1773.15 K	1823.15 K
Li N	$\text{LiO}_{0.5}(\text{l}) = \text{Li}(\text{g}) + \frac{1}{4}\text{O}_2$	1	0		-5.36±0.05		
Li N	$\text{LiO}_{0.5}(\text{l}) + \frac{1}{4}\text{O}_2 = \text{LiO}(\text{g})$	-1	0		-3.39±0.07		
Na N	$\text{NaO}_{0.5}(\text{l}) = \text{Na}(\text{g}) + \frac{1}{4}\text{O}_2$	1	0		-4.25±0.10		
K N	$\text{KO}_{0.5}(\text{l}) = \text{K}(\text{g}) + \frac{1}{4}\text{O}_2$	1	0		-3.95±0.06		
Rb N	$\text{RbO}_{0.5}(\text{l}) = \text{Rb}(\text{g}) + \frac{1}{4}\text{O}_2$	1	14.4	-4.15	-3.12±0.10	-2.63±0.02	-2.26
Cu N	$\text{CuO}_{0.5}(\text{l}) = \text{Cu}(\text{g}) + \frac{1}{4}\text{O}_2$	1	0	-4.09±0.12	-3.70±0.10	-3.13±0.06	-2.90
Ag N	$\text{AgO}_{0.5}(\text{l}) = \text{Ag}(\text{g}) + \frac{1}{4}\text{O}_2$	1	0	-2.23			
Zn N	$\text{ZnO}(\text{l}) = \text{Zn}(\text{g}) + \frac{1}{2}\text{O}_2$	2	9.0	-5.06±0.09	-3.96±0.09	-2.92±0.17	-2.57
Ge N	$\text{GeO}_2(\text{l}) = \text{GeO}(\text{g}) + \frac{1}{2}\text{O}_2$	2	10.4	-5.04±0.13	-3.70±0.06	-2.71±0.13	-2.29
Cd N	$\text{CdO}(\text{l}) = \text{Cd}(\text{g}) + \frac{1}{2}\text{O}_2$	2	0	-2.48			
Ga N	$\text{GaO}_{1.5}(\text{l}) = \text{Ga}(\text{g}) + \frac{3}{4}\text{O}_2$	3	0		-9.92±0.32	-8.42±0.07	-7.76
Ga N	$\text{GaO}_{1.5}(\text{l}) = \text{GaO}(\text{g}) + \frac{1}{4}\text{O}_2$	1	0		-5.10±0.26	-4.45±0.04	-4.16
Pb N	$\text{PbO}(\text{l}) = \text{PbO}(\text{g})$	0	0	-2.90±0.12	-2.00		
Pb N	$\text{PbO}(\text{l}) = \text{Pb}(\text{g}) + \frac{1}{2}\text{O}_2$	2	0	-4.47±0.19	-3.49		
Mo N	$\text{MoO}_3(\text{l}) = \text{MoO}_3(\text{g})$	0	0	-4.67	-4.34±0.00	-3.64±0.01	-3.41
Mo N	$\text{MoO}_2(\text{l}) + \frac{1}{2}\text{O}_2 = \text{MoO}_3(\text{g})$	-2	0	-2.87	-2.86±0.00	-2.48±0.01	-2.39
Cr N	$\text{CrO}(\text{l}) + \frac{1}{2}\text{O}_2 = \text{CrO}_2(\text{g})$	-2	0		-2.70	-2.40±0.03	-2.29
Cr N	$\text{CrO}_{1.5}(\text{l}) + \frac{1}{4}\text{O}_2 = \text{CrO}_2(\text{g})$	-1	0		-4.96	-4.41±0.03	-4.20

Table 4. Evaporation- (α_e) and activity coefficients (γ_i) of melt oxide species. Evaporation coefficients calculated with eq. 6 using activity coefficients shown in the references, activity coefficients calculated with $\alpha_e = 1$ from eq. 6.

Species		Temperature (K)				
		1573.15	1673.15	1773.15	1823.15	1923.15
ZnO	γ_i (this work)	0.24±0.02	0.51±0.13	0.97±0.38	1.01	
	γ_i (literature)		0.25 ^a	0.43 ^a	0.58 ^a	
	α_e		2.0	2.2	1.7	
RbO _{0.5}	γ_i (this work)		$1.3 \times 10^{-4} \pm 1.5 \times 10^{-5}$	$7.4 \times 10^{-5} \pm 5.9 \times 10^{-6}$	9.0×10^{-5}	
GeO ₂	γ_i (this work)	0.04±0.01	0.11±0.01	0.18±0.07	0.19	
CuO _{0.5}	γ_i (this work)	24.0±6.3	11.8±1.7	8.5±0.1	6.4	4.2*
	γ_i (literature)	10±1 ^b				3.5 ^c
	α_e	2.4±0.8				1.2
KO _{0.5}	γ_i (this work)		$2.2 \times 10^{-4} \pm 5.5 \times 10^{-5}$			
	γ_i (literature)		$5 \times 10^{-5} - 7 \times 10^{-4}$, ^d			
	α_e		0.3 - 3.4			
NaO _{0.5}	γ_i (this work)		$1.0 \times 10^{-3} \pm 2.2 \times 10^{-4}$			
	γ_i (literature)		$8.4 \times 10^{-4} - 2.2 \times 10^{-3}$, ^e			
	α_e		0.3 - 1.7			
PbO [^]	γ_i (this work)	0.06±0.02	0.17			
	γ_i (literature)					0.22 ^c
	α_e	0.3*	0.8*			
PbO [#]	γ_i (this work)	0.21±0.09	0.38			
	γ_i (literature)					0.22 ^c
	α_e	1.0*	1.7*			
LiO _{0.5} (air)	γ_i (this work)		1.8±0.2			
LiO _{0.5} (-8)	γ_i (this work)		15.4±3.1			
AgO _{0.5}	γ_i (this work)		0.67			
CdO	γ_i (this work)		0.15			

a = Reyes and Gaskell, 1983; b = Holzheid et al. 2001; c = Wood and Wade, 2013; d = Hastie et al. 1982; e = Mathieu et al. 2011

[^] = calculated from the reaction $\text{PbO(l)} = \text{PbO(g)}$

[#] = calculated from the reaction $\text{PbO(l)} = \text{Pb(g)} + \frac{1}{2}\text{O}_2$

* extrapolated to 1923.15 K

Table 5. Equilibrium thermodynamic data (entropy and enthalpy) for reactions investigated herein (experimental) in addition to those in the metal-oxygen system (pure system).

Element	Reaction	n	# points	Experimental				Pure System		Source
				ΔS^* (kJ/molK)	\pm	ΔH^* (kJ)	\pm	ΔS° (kJ/molK)	ΔH° (kJ)	
<i>Experimental</i>										
Li*	$\text{LiO}_{0.5}(\text{l}) = \text{Li}(\text{g}) + 1/4\text{O}_2$	1	1	0.133		413.0		0.139	413.0	1
Li*	$\text{LiO}_{0.5}(\text{l}) = \text{Li}(\text{g}) + 1/4\text{O}_2$	-1	1	0.130		326.3		0.107	326.3	1
Na*	$\text{NaO}_{0.5}(\text{l}) = \text{Na}(\text{g}) + 1/4\text{O}_2$	1	1	0.071		255.0		0.128	255.0	2
K*	$\text{KO}_{0.5}(\text{l}) = \text{K}(\text{g}) + 1/4\text{O}_2$	1	1	0.050		209.5		0.120	209.5	2
Cr*	$\text{CrO}(\text{l}) + 1/2\text{O}_2 = \text{CrO}_2(\text{g})$	-2	4	0.046	0.016	163.1	28.6	0.080	237.6	1, 6
Cr*	$\text{CrO}_{1.5}(\text{l}) + 1/4 \text{O}_2 = \text{CrO}_2(\text{g})$	-1	4	0.085	0.017	301.2	29.1	0.128	414.3	1
Cu	$\text{CuO}_{0.5}(\text{l}) = \text{Cu}(\text{g}) + 1/2\text{O}_2$	1	9	0.089	0.009	264.0	15.7	0.135	377.7	1, 4
Zn	$\text{ZnO}(\text{l}) = \text{Zn}(\text{g}) + 1/2 \text{O}_2$	2	10	0.253	0.011	548.6	19.6	0.177	411.7	3
Ga	$\text{GaO}_{1.5}(\text{l}) = \text{Ga}(\text{g}) + 3/4\text{O}_2$	3	6	0.334	0.026	885.9	45.7	0.245	760.4	3
Ga	$\text{GaO}_{1.5}(\text{l}) = \text{GaO}(\text{g}) + 1/4\text{O}_2$	1	6	0.117	0.015	358.9	24.6	0.199	633.7	3
Ge	$\text{GeO}_2(\text{l}) = \text{GeO}(\text{g}) + 1/2\text{O}_2$	2	10	0.294	0.014	612.7	23.9	0.219	453.8	3
Rb	$\text{RbO}_{0.5}(\text{l}) = \text{Rb}(\text{g}) + 1/4\text{O}_2$	1	6	0.123	0.024	306.4	41.6	0.255	402.4	2
Mo*	$\text{MoO}_3(\text{l}) = \text{MoO}_3(\text{g})$	0	6	0.118	0.016	332.4	16.4	0.120	316.3	1
Mo*	$\text{MoO}_2(\text{l}) + 1/2\text{O}_2 = \text{MoO}_2(\text{g})$	-2	6	0.033	0.004	143.2	7.8	0.075	151.2	1
Pb	$\text{PbO}(\text{l}) = \text{PbO}(\text{g})$	0	3	0.232	0.043	452.1	70.6	0.119	238.0	3
Pb	$\text{PbO}(\text{l}) = \text{Pb}(\text{g}) + 1/2\text{O}_2$	2	3	0.227	0.070	490.9	112.1	0.159	364.7	3
<i>Pure System[#]</i>										
Mg	$\text{MgO}(\text{l}) = \text{Mg}(\text{g}) + 1/2\text{O}_2$	2						0.186	666.4	1
Ni	$\text{NiO}(\text{l}) = \text{Ni}(\text{g}) + 1/2\text{O}_2$	2						0.200	597.5	1,5
Fe	$\text{FeO}(\text{l}) = \text{Fe}(\text{g}) + 1/2\text{O}_2$	2						0.183	644.4	1
Mn	$\text{MnO}(\text{l}) = \text{Mn}(\text{g}) + 1/2\text{O}_2$	2						0.173	606.3	1,4
Co	$\text{CoO}(\text{l}) = \text{Co}(\text{g}) + 1/2\text{O}_2$	2						0.192	600.0	1,4
Cr	$\text{CrO}(\text{l}) = \text{Cr}(\text{g}) + 1/2\text{O}_2$	2						0.197	712.6	1,6

1 Chase 1998 ; 2 Lamoreaux and Hildenbrand, 1984 ; 3 Lamoreaux et al., 1987; 4 O'Neill and Pownceby, 1993; 5 Robie and Hemingway, 1995; 6 Toker et al., 1991

* denotes elements for which $\log K^*$ was measured at only 1 temperature, ΔS^* and ΔH^* determined by assuming γ_i remains constant over all temperatures.

[#] pure system elements were calculated assuming $\gamma_i = 1$ at all temperatures.

^o enthalpies and entropies of formation for pure system calculated from $\Delta G^\circ = \Delta H^\circ - T\Delta S^\circ$ from T = 1000 to 2000 K

Table 6. 1% Evaporation temperatures from silicate melt at 1 bar

logfO ₂	-10		-5		-0.68	
Element	T (K)	±	T (K)	±	T (K)	±
Pb	1360	50	1563	9	1669	6
Ge	1432	9	1612	3	1809	4
Zn	1418	10	1618	5	1843	2
Rb	1465	28	1668	5	1863	16
Cu	1507	9	1746	3	2023	22
K	1548		1867		2290	
Ga	1703	1	1959	17	2239	47
Na	1623		1914		2267	
Li	1886		2092		1976	
Cr	2155		2096	52	1785	4
Mo			2138	41	1816	3
Mg	2080		2445		2883	
Ni	1787		2086		2439	
Fe	2033		2394		2830	
Mn	1974		2339		2783	
Co	1842		2159		2538	